Eur. Phys. J. Special Topics **207**, 1–117 (2012)

DOI: 10.1140/epjst/e2012-01599-9

THE EUROPEAN PHYSICAL JOURNAL
SPECIAL TOPICS

Review

Storage ring at HIE-ISOLDE

Technical design report

M. Grieser[1], Yu.A. Litvinov[2,3,a], R. Raabe[4], K. Blaum[1,2], Y. Blumenfeld[5], P.A. Butler[6], F. Wenander[5], P.J. Woods[7], M. Aliotta[7], A. Andreyev[8], A. Artemyev[2], D. Atanasov[9], T. Aumann[10,3,a], D. Balabanski[11], A. Barzakh[12], L. Batist[12], A.-P. Bernardes[5], D. Bernhardt[13], J. Billowes[14], S. Bishop[15], M. Borge[16], I. Borzov[17], F. Bosch[3,a], A.J. Boston[6], C. Brandau[18,19], W. Catford[20], R. Catherall[5], J. Cederkäll[5,21], D. Cullen[14], T. Davinson[7], I. Dillmann[22,3,a], C. Dimopoulou[3,a], G. Dracoulis[23], Ch.E. Düllmann[24,25,3,a], P. Egelhof[3,a], A. Estrade[3,a], D. Fischer[1], K. Flanagan[5,14], L. Fraile[26], M.A. Fraser[5], S.J. Freeman[14], H. Geissel[22,3,a], J. Gerl[10,3,a], P. Greenlees[27,28], R.E. Grisenti[29,3,a], D. Habs[30], R. von Hahn[1], S. Hagmann[29], M. Hausmann[31], J.J. He[32], M. Heil[3,a], M. Huyse[4], D. Jenkins[33], A. Jokinen[27,28], B. Jonson[34], D.T. Joss[6], Y. Kadi[5], N. Kalantar-Nayestanaki[35], B.P. Kay[33], O. Kiselev[3,a], H.-J. Kluge[3,a], M. Kowalska[5], C. Kozhuharov[3,a], S. Kreim[1,5], T. Kröll[10], J. Kurcewicz[5], M. Labiche[36], R.C. Lemmon[36], M. Lestinsky[3,a], G. Lotay[7], X.W. Ma[32], M. Marta[3,a], J. Meng[37], D. Mücher[15], I. Mukha[3,a], A. Müller[13], A.St J. Murphy[7], G. Neyens[4], T. Nilsson[34], C. Nociforo[3,a], W. Nörtershäuser[24], R.D. Page[6], M. Pasini[5], N. Petridis[29], N. Pietralla[10], M. Pfützner[38], Z. Podolyák[20], P. Regan[20], M.W. Reed[20,23], R. Reifarth[29], P. Reiter[39], R. Repnow[1], K. Riisager[40], B. Rubio[41], M.S. Sanjari[29], D.W. Savin[42], C. Scheidenberger[22,3,a], S. Schippers[13], D. Schneider[43], R. Schuch[44], D. Schwalm[1,45], L. Schweikhard[46], D. Shubina[1], E. Siesling[5], H. Simon[3,a], J. Simpson[36], J. Smith[8], K. Sonnabend[29], M. Steck[3,a], T. Stora[5], T. Stöhlker[47,48,3,a], B. Sun[37], A. Surzhykov[2], F. Suzaki[49], O. Tarasov[31], S. Trotsenko[48], X.L. Tu[32], P. Van Duppen[4], C. Volpe[50], D. Voulot[5], P.M. Walker[5,20], E. Wildner[5], N. Winckler[1], D.F.A. Winters[3,a], A. Wolf[1], H.S. Xu[32], A. Yakushev[3,a], T. Yamaguchi[49], Y.J. Yuan[32], Y.H. Zhang[32], and K. Zuber[51]

[1] Max-Planck-Institut für Kernphysik, 69117 Heidelberg, Germany
[2] Ruprecht-Karls-Universität Heidelberg, 69120 Heidelberg, Germany
[3] GSI Helmholtzzentrum für Schwerionenforschung, 64291 Darmstadt, Germany
[4] Instituut voor Kern- en Stralingsfysica, KU Leuven, 3001 Leuven, Belgium
[5] CERN, 1211 Geneva 23, Switzerland
[6] Department of Physics, University of Liverpool, Liverpool L69 7ZE, UK
[7] School of Physics and Astronomy, University of Edinburgh, Edinburgh EH9 3JZ, UK
[8] University of the West of Scotland, Paisley PA1 2BE, UK
[9] Faculty of Physics, St. Kliment Ohridski University of Sofia, 1164 Sofia, Bulgaria
[10] Institut für Kernphysik, Technische Universität Darmstadt, 64289 Darmstadt, Germany
[11] Institute for Nuclear Research and Nuclear Energy, Bulgarian Academy of Sciences, 1784 Sofia, Bulgaria
[12] Petersburg Nuclear Physics Institute, 188350 Gatchina, Russia
[13] Institut für Atom- und Molekülphysik, Universität Gießen, 35392 Gießen, Germany
[14] School of Physics and Astronomy, University of Manchester, Manchester, M13 9PL, UK
[15] Physik Department E12, Technische Universität München, 85748 Garching, Germany

[a] The members of the GSI Helmholtzzentrum für Schwerionenforschung will exploit the synergies with the FAIR physics program and concentrate on R&D activities relevant for FAIR.

[16] Instituto de Estructura de la Materia, CSIC, 28006 Madrid, Spain
[17] Centr Jadernykh Dannykh, Fiziko-Energeticheskij Institut, 249033 Obninsk, Russia
[18] ExtreMe Matter Institute EMMI, 64291 Darmstadt, Germany
[19] Frankfurt Institute for Advanced Studies (FIAS), 60438 Frankfurt am Main, Germany
[20] Department of Physics, University of Surrey, Guildford, GU2 7XH, UK
[21] Physics Department, University of Lund, Box-118, 22100 Lund, Sweden
[22] II. Physikalisches Institut, Universität Gießen, 35392 Gießen, Germany
[23] Department of Nuclear Physics, Australian National University, Canberra ACT 0200, Australia
[24] Institut für Kernchemie, Universität Mainz, 55128 Mainz, Germany
[25] Helmholtz Institute Mainz, 55099 Mainz, Germany
[26] Facultad de Físicas, Universidad Complutense, 28040 Madrid, Spain
[27] Department of Physics, University of Jyväskylä, 40014 Jyväskylä, Finland
[28] Helsinki Institute of Physics, University of Helsinki, 00014 Helsinki, Finland
[29] Goethe-Universität Frankfurt, 60438 Frankfurt, Germany
[30] Fakultät für Physik, Ludwig-Maximilians-Universität München, 85748 Garching, Germany
[31] NSCL, Michigan State University, East Lansing, Michigan 48824, USA
[32] Institute of Modern Physics, Chinese Academy of Sciences, Lanzhou 730000, PR China
[33] Department of Physics, University of York, York YO10 5DD, UK
[34] Department of Fundamental Physics, Chalmers University of Technology, 412 96 Göteborg, Sweden
[35] Kernfysisch Versneller Institute (KVI), University of Groningen, 9747 AA Groningen, The Netherlands
[36] Nuclear Physics Group, STFC Daresbury Laboratory, Daresbury, Warrington, WA4 4AD, UK
[37] School of Physics and Nuclear Energy Engineering, Beihang University, 100191 Beijing, PR China
[38] Faculty of Physics, University of Warsaw, 00-681 Warszawa, Poland
[39] Institut für Kernphysik, Universität zu Köln, 50937 Köln, Germany
[40] Department of Physics and Astronomy, Aarhus University, 8000 Aarhus C, Denmark
[41] Instituto de Física Corpuscular, CSIC-Uni. Valencia, 46071 Valencia, Spain
[42] Columbia Astrophysics Laboratory, Columbia University, New York, NY 10027, USA
[43] University of California, Lawrence Livermore National Laboratory, Livermore, CA 94550, USA
[44] Department of Atomic Physics, Stockholm University, AlbaNova, 10691 Stockholm, Sweden
[45] Weizmann Institute of Science, Rehovot 76100, Israel
[46] Institute of Physics, Ernst-Moritz-Arndt-University Greifswald, 17487 Greifswald, Germany
[47] Friedrich-Schiller-Universität Jena, 07737 Jena, Germany
[48] Helmholtz Institute Jena, 07743 Jena, Gemany
[49] Department of Physics, Saitama University, Saitama 338-8570, Japan
[50] Institut de Physique Nucléaire (IPN), 91406 Orsay, France
[51] Institut für Kern- und Teilchenphysik, Technische Universität Dresden, 01069 Dresden, Germany

Received 13 January 2012 / Received in final form 15 March 2012
Published online 11 May 2012

Abstract. We propose to install a storage ring at an ISOL-type radioactive beam facility for the first time. Specifically, we intend to setup the heavy-ion, low-energy ring TSR at the HIE-ISOLDE facility in CERN, Geneva. Such a facility will provide a capability for experiments with stored secondary beams that is unique in the world. The envisaged

physics programme is rich and varied, spanning from investigations of nuclear ground-state properties and reaction studies of astrophysical relevance, to investigations with highly-charged ions and pure isomeric beams. The TSR might also be employed for removal of isobaric contaminants from stored ion beams and for systematic studies within the neutrino beam programme. In addition to experiments performed using beams recirculating within the ring, cooled beams can also be extracted and exploited by external spectrometers for high-precision measurements. The existing TSR, which is presently in operation at the Max-Planck Institute for Nuclear Physics in Heidelberg, is well-suited and can be employed for this purpose. The physics cases as well as technical details of the existing ring facility and of the beam and infrastructure requirements at HIE-ISOLDE are discussed in the present technical design report.

1 Introduction

Nuclear physics experiments with stored exotic nuclei have demonstrated their enormous scientific potential in recent years [1,2]. Presently there are two heavy-ion storage ring facilities worldwide performing such experiments, namely the ESR in Darmstadt and the CSRe in Lanzhou [3]. However, these facilities are specialized for experiments at relativistic energies, but a broad range of new experiments would become possible with the availability of stored secondary beams at lower energies (0.5–10 MeV/u). Although slowing down of stored beams can be done at the existing storage rings, it is a time consuming and inefficient process that has so far been limited to stable nuclides.

An important distinctive feature of this proposal is that the ion beams will be produced by the Isotope Separation On-Line (ISOL) method, whereas both of the existing storage ring facilities are based on the in-flight production of secondary beams at high energies (∼1 GeV/u) [3]. The complementary ISOL method employed at ISOLDE is superior in terms of the beam intensity for a large number of elements and the beam quality. Moreover, the existing and planned post-acceleration schemes can deliver high-quality ISOL beams right at the required energies, which circumvents the long slowing down times required for the relativistic ion beams.

We propose to install a low-energy heavy-ion storage ring at an ISOL facility for the first time. We will cool and store post-accelerated high-intensity beams available from HIE-ISOLDE at CERN using the existing ring TSR, which is presently in operation at the Max-Planck Institute for Nuclear Physics in Heidelberg (MPIK) [4,5]. This will open up an extremely rich scientific programme in nuclear physics, nuclear astrophysics and atomic physics. We emphasize that most of the discussed experiments can only be done with the proposed facility.

This Technical Design Report describes the physics motivation (Sect. 2), beam requirements for the HIE-ISOLDE facility (Sect. 3), technical specifications of the TSR (Sect. 4), as well as the required infrastructure and supplies (Sect. 5).

2 Physics motivation

2.1 Introduction: Beam properties in the TSR

The use of the Test Storage Ring coupled to the HIE-ISOLDE post-accelerator offers a number of unique opportunities for research in nuclear and atomic physics. The topics are explored in the following chapters, where some concrete examples are also

Table 1. Parameters of beams circulating in the TSR. See text for details.

Ion	Nuclear lifetime	Energy (MeV/u)	Cooling time	Beam lifetime in residual gas	H_2 target (atoms/cm^2)	Beam lifetime in target	Eff. target thickness (μg/cm^2)
^{7}Be 3^+	(53 d)	10	2.3 s	370 s			
^{18}F 9^+	100 m	10	0.7 s	280 s	1×10^{14}	236 s	31000
^{26m}Al 13^+	6.3 s	10	0.5 s	137 s	5×10^{14}	23 s	4200
^{52}Ca 20^+	4.6 s	10	0.4 s	58 s	5×10^{14}	9.6 s	3000
^{70}Ni 28^+	6.0 s	10	0.25 s	30 s	2×10^{14}	12 s	1600
^{70}Ni 25^+	6.0 s	10	0.3 s	26 s	2×10^{13}	2.1 s	60
^{132}Sn 30^+	40 s	4	0.4 s	1.5 s	1×10^{12}	1.4 s	1.2
^{132}Sn 45^+	40 s	4	0.2 s	1.4 s	5×10^{12}	1.6 s	7
^{132}Sn 39^+	40 s	10	0.25 s	7.4 s	2×10^{12}	3.6 s	9.5
^{132}Sn 45^+	40 s	10	0.2 s	10 s	5×10^{13}	1.3 s	90
^{186}Pb 46^+	4.8 s	10	0.25 s	4 s	2×10^{12}	1.5 s	4
^{186}Pb 64^+	4.8 s	10	0.13 s	5 s	1×10^{13}	1.7 s	20

discussed. In this context it is useful to briefly review the general features of the different ways in which experiments are foreseen to be performed at the TSR. The short illustration that follows is based on the extended descriptions given in the technical sections – in particular Sect. 3 (the post-accelerator) and 4 (the storage ring).

The way to achieve an efficient transfer of the ion beam into the TSR at Heidelberg is by occupying the available phase space through a "multi-turn" injection (see Chapt. 4.5). This operation is fast (≈50 μs using 40 turns at a beam energy of 10 MeV/nucleon), however it has to be followed by a *cooling time* during which the beam is reduced in energy spread and size, from a diameter of a few centimeters to about 1 mm. This is achieved with electron cooling, described in Chapt. 4.6. Cooling times may vary between about 0.1 s and about one second. When cooling is complete, a measurement can take place in the TSR, until the following injection. Alternatively, several injection-cooling cycles can follow each other increasing the particle current, before performing the measurement. With the present power supplies, the frequency of injections is limited to 5 Hz, however a lower frequency needs to be used to allow time for the measurement. Notice that the new injection does not affect the beam already circulating in the TSR: the intensity simply adds up (the maximum current which can be stored is about 1 mA).

The timing properties of the ion beams post-accelerated in HIE-ISOLDE are determined by the operation modes of REXTRAP and REXEBIS. Currently at the ISOLDE accelerator REX, beam particles are bunched in short bursts (≈100 μs) at repetition rates of 3 Hz to 50 Hz. The extraction time is already compatible with the multi-turn injection into the TSR, and by accumulating the ions for a longer time in REXTRAP the repetition can be lowered to suit the operation of TSR and thereby ensure an optimal use of the HIE-ISOLDE beams.

The cooling times of various beams are reported in Table 1. The calculations are explained in detail in Chapt. 4.6.2. Table 1 also shows the expected lifetime of beams in the TSR, as determined by the interaction with the residual gas (at a pressure of 2×10^{-10} mbar) and with a H_2 gas target (a gas-jet target or similar, as it could be used for reaction measurements) of a given thickness. The lifetimes are calculated using the prescriptions of Nikolaev et al. [6] for electron capture cross sections, and Dmitriev et al. [7] for electron stripping (further details are given in Chapt. 4.8). The target thickness is chosen in order to ensure a sufficiently long lifetime, and reflects

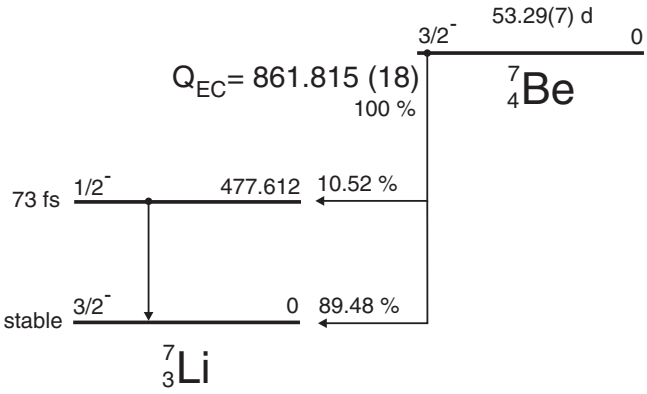

Fig. 1. Known decay scheme of neutral ^{7}Be atoms [8].

the characteristics of gas targets presently used in storage rings. It is also important to mention that, owing to a large momentum acceptance of the TSR of $\pm 3\%$ [5], a simultaneous storage of the beam in several atomic charge-states is feasible (for more details see Sect. 4.4). In this case the losses of the stored beam due to atomic electron stripping/pick-up reactions can be significantly reduced.

For the calculation of the total current intensity in the TSR, one has to consider the shortest one between the lifetimes quoted in Table 1. If τ is this shortest lifetime and i is the intensity of the post-accelerated beam in HIE-ISOLDE, the total intensity of the beam circulating in the TSR is given by $I = i\epsilon f\tau$, where ϵ is the injection efficiency and f is the revolution frequency (about 790 kHz at 10 MeV/nucleon). One can see that an increase in intensity of several orders of magnitude can be achieved.

For experiments using an internal gas target, the intensity increase should counter the much lower target thickness of the gas jet when compared to target foils used in conventional setups. This can be evaluated by defining the "effective target thickness" shown in the last column of Table 1, which is calculated by multiplying the thickness of the gas target by the increase in beam intensity $f\tau$ (the injection efficiency is here assumed to be 100% for simplicity). To attain a usable effective target thickness, energies of 10 MeV/nucleon and high charge states are desirable; the latter help both by allowing a shorter cooling time and smaller cross section for electron capture and stripping.

Experiments can also be performed with a beam *extracted* from the TSR. The details of this operation are described in Chapt. 4.10. The extracted beam is essentially DC, which can be of great advantage in experiments for which the high instantaneous rate of HIE-ISOLDE beams is a problem. In addition, the optical and purity characteristics of the extracted beam can be of much higher quality than the direct HIE-ISOLDE beam, thanks to mass-selective acceleration (Chapt. 4.9.1) and cooling in the TSR. Possibilities of measurements with extracted beams are further elaborated in Chapt. 2.7.4.

2.2 Half-lives of ^{7}Be in different atomic charge states

The decay scheme of neutral ^{7}Be atoms is shown in Fig. 1. Neutral ^{7}Be atoms are radioactive and decay with the half-life of about 53 d [8] to stable ^{7}Li atoms via the only energetically allowed decay channel, namely the orbital electron capture decay (EC):

$$^7\mathrm{Be}(e^-, \nu)^7\mathrm{Li}\ .$$

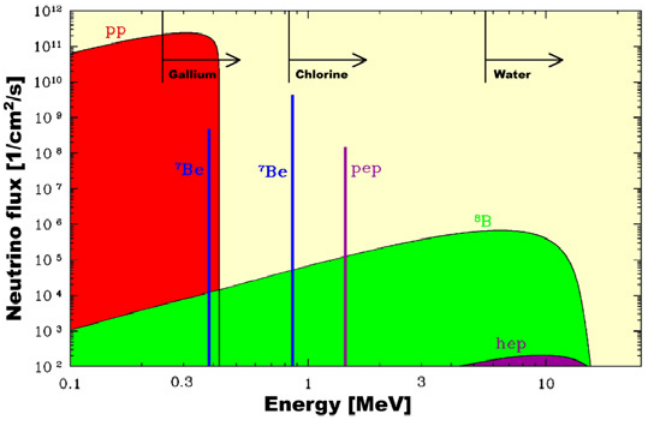

Fig. 2. Solar neutrino fluxes for different nuclear reactions as a function of neutrino energy.

Attempts to obtain the "true" terrestrial half-life of ^{7}Be are done in numerous experiments worldwide in which ^{7}Be atoms are implanted in different chemical environments, see, e.g., recent experiments in Refs. [9,10]. The motivation for studying this decay is its impact for Solar physics, where the survival probability of ^{7}Be plays a crucial role for the neutrino fluxes from the ^{7}Be EC- and ^{8}B β^{+}-decays [11] (see Fig. 2). Although the main decay channel of ^{7}Be in the Sun's interior is the free electron capture, Iben, Kalata & Schwartz [12] have shown that bound electrons can significantly increase the decay probability. Theoretical predictions exist indicating that about 20% of ^{7}Be in the center of the Sun might have a bound electron [12,13]. A longer lifetime of ^{7}Be in the Sun would increase the probability of its destruction via the $^{7}\mathrm{Be}(p,\gamma)^{8}\mathrm{B}$ capture reaction. The ^{7}Be neutrino flux from the Sun has been recently measured with less than 5% uncertainty by the Borexino experiment [14]. Therefore, a reliable value for the ^{7}Be EC-decay rate would provide, e.g., deeper insight in the branchings of the pp-chain or even give valuable information on the free electron capture decay rate, the decay channel which is presently inaccessible in the laboratory.

The EC-decay rate is proportional to the electron density at the nucleus [15]. In a simple picture the density of s-electrons in L, M and higher atomic shells scales as $1/n^3$ (n is the principal quantum number). This means that the capture rate is dominated by K-shell electrons since $\lambda_K/\lambda_L \approx 2^3 = 8$, $\lambda_K/\lambda_M \approx 3^3 = 27$, etc. Possible deviations from this simple assumption have been predicted for highly-charged atoms [16]. It is clear that fully-ionized ^{7}Be ions are stable. However, estimating the half-life of ^{7}Be in hydrogen-like (H-like) and helium-like (He-like) charge states is not trivial, because:

– Experiments with stored H-like ions have shown [17,19] that the EC-decay rate can be dramatically suppressed or enhanced depending on the populated hyperfine state. According to a simple theory [20,21], the EC-decay rate for transitions $I_i \to I_f = I_i - 1$ (I_i and I_f are nuclear spins in the initial, i, and final, f, states) conserving the total angular momentum $F_i = F_f$ ($F = I \pm s$) in H-like ions is larger by $(2I_i+1)/(2F_i+1)$ than in He-like ions. The 10.52% EC-decay branch of ^{7}Be to the excited state in ^{7}Li is an allowed Gamow-Teller $I_i \to I_i - 1$ transition. The initial state has two hyperfine states with $F_i = 1$ and $F_i = 2$ and the final state has $F_f = 0$ and $F_f = 1$. Only the decay between $F_i = F_f = 1$ is allowed. The magnetic moment of ^{7}Be is negative [22] which yields $F_i = 2$ to be the ground

state. However, due to the tiny splitting, the hyperfine states in the Sun as well as in terrestrial laboratories will be in thermal equilibrium. Thus, only 3/8 of all H-like ^{7}Be ions are in $F_i = 1$ state, which can decay to the first excited state in ^{7}Li. According to [20,21], the rate of the transition $F_i = F_f = 1$ can also be accelerated compared to conventional calculations [15].

– The density of bound-electrons, and thus the EC-decay rate, is strongly affected by the electron screening [23]. There is *no* experimental information on the electron screening corrections, and, thus, the knowledge of ^{7}Be half-lives in different atomic charge states is indispensable. We emphasize that besides the application of the measured half-lives of ^{7}Be for Solar physics, a benchmarking of the electron screening calculations can be done for the first time. Furthermore, systematic studies can be performed with other isotopes in full analogy with ^{7}Be.

This "textbook" experiment [24,25] could not be done up to now and can be performed for the first time in the storage ring at ISOLDE. The expected half-life of $^{7}Be^{3+}$ is about 100 d [25]. Thus, for a successful experiment, a few 10^6 to 10^7 stored $^{7}Be^{3+}$ ions are required, while the ISOLDE yield is $2.8 \cdot 10^{10}$ particles/s. Achieving the required charge state can be done with the existing electron beam ion source (REXEBIS). The time needed for breeding (below 100 ms) is negligible in comparison with the half-life of ^{7}Be ions. Taking into account the transmission efficiency, space charge limitations of REXTRAP, an estimated intensity in front of the TSR is about $10^8 - 10^9$ of $^{7}Be^{3+}$ ions per second. This intensity is by far sufficient to perform this experiment.

Due to the small Q_{EC}-value, the frequency distributions of stored parent $^{7}Be^{3+}$ and daughter $^{7}Li^{3+}$ ions will overlap and their direct resolution is not feasible. Dependent on the TSR vacuum, current of cooling electrons, and beam parameters, the storage lifetime of H-like $^{7}Be^{3+}$ ions is 3–5 min, which is dominated by the stripping of the bound electron in the residual gas of the TSR. The bare $^{7}Be^{4+}$ ions can easily be removed from the TSR. The storage lifetime of fully-ionized daughter $^{7}Li^{3+}$ ions is by a factor of about 30 longer than of H-like $^{7}Be^{3+}$ ions, and this factor can be further enhanced if a gas-jet target is employed. The main loss channel of $^{7}Li^{3+}$ is the pick-up of electrons in the cooler, where the H-like $^{7}Li^{2+}$ ions can be detected with about 100% efficiency by a particle detector after one of the TSR dipoles. The storage lifetimes as well as the cross-sections for electron pick-up and stripping can be accurately calibrated with stable Li and Be ions in all required charge states. To minimize systematic errors, the measurements can be performed with different initial numbers of stored $^{7}Be^{3+}$ ions.

2.3 In-flight beta-decay of light exotic nuclei

Peculiar features appearing in light exotic nuclei, such as clustering [26] and halos [27], can be effectively investigated experimentally through the β-decay, either from or towards the states of interest. Among other probes, for example complex nuclear reactions, β-decay has the advantage of being described by a well-established theory. In light nuclei, especially close to the drip lines, β-decay is characterized by large Q-values and low breakup thresholds in the daughter nuclei, so that feeding to unbound resonances and delayed emission of particles become possible (in this section "particle" refers to nucleons and light ions). In the case of halo nuclei, the same phenomenon could lead to direct decays to the continuum. The detection of the emitted particles serves at once for the identification of the decay paths, and to collect additional information about the structure of the populated states. Recent experimental results in this field include, among others, the study of unbound states of astrophysical relevance in ^{12}C [28], the β-delayed deuteron emission of ^{11}Li [29], the determination

of the $E1$ component of the $^{12}C(\alpha,\gamma)^{16}O$ cross section through the measurement of the β-delayed α decay of ^{16}N [30].

Regardless of the Q-value of the β decay at hand, the particle-emission channels are usually characterized by a small relative momentum of the fragments, because the region of interest, where the decay proceeds to, lies close to the particle threshold [31]. Besides the cases cited above, other examples of this behaviour are in the $\alpha + d$ decay of ^{6}He [32,33], or the β-delayed proton emission of ^{23}Al [34]. Theoretical studies have been recently performed on a possible proton-emission channel in the decay of ^{11}Li [35], and the β-delayed proton emission by one-neutron halo nuclei [36] such as ^{11}Be, ^{19}C and ^{31}Ne; such β-delayed proton decays in neutron-rich nuclei have not been observed so far.

Some of these cases remain outside the reach of current radioactive ion beam facilities. Even when the parent isotope can be produced with sufficient intensity, however, the detection of the very low-energy emitted particles represent a challenge for conventional setups, because identification of the particles is also required to single out the (weak) decay channel among an overwhelming background. In the case of the β-delayed proton emission of ^{11}Be, for example, the Q-value is only 0.281 MeV and the maximum of the emission is probably in the range 0.1–0.2 MeV centre-of-mass energy [36].

This problem could be overcome by observing the nuclei decay in-flight in the TSR, and detecting the emitted particles in appropriate positions along the ring. Because of the large forward momentum of the parent nucleus, the emission of the particles takes place in a narrow cone around the beam axis. For example, the decay of 10 MeV/nucleon ^{6}He into $\alpha + d$ at $E_{\mathrm{c.m.}} = 0.4$ MeV (the lowest energy reached by measurements so far) would generate deuterons within a cone of 6.6 degrees and energies between 15 MeV and 25 MeV (the α particles would be emitted in a cone half the size). The decay of 10 MeV/nucleon ^{11}Be into ^{10}Be + p would produce protons at a maximum angle of 9.9 degrees, with energies between 7 MeV and 13.5 MeV. The α particles from the decay of ^{16}N would, in the region of interest for astrophysics, be emitted within a cone of 8 degrees with energies between 30 MeV and 50 MeV. Detection of the emitted light ions could take place in charged-particle detectors, which would provide energy and trajectory information. A possible configuration could comprise a few evenly-spaced silicon-strip detectors, placed off the beam axis, at a distance of about 10 cm from each other along a straight section of the ring. The thickness would be determined by the energy to be detected – for example in the case of the protons from the decay of ^{11}Be mentioned above, 300 μm-thick detectors could be used. Such an arrangement is possible because the energy range of the particles to be detected is limited, while their total energy is relatively large. In addition, in most of the cases, the residual nucleus could also be identified, measuring its magnetic rigidity in a dipole of the TSR.

A timing scheme injection-cooling-measurement would be employed (see Sect. 2.1), as a good definition of the beam optics would be required for the measurement of the emission angles.

The TSR clearly represents a unique instrument for this type of measurements, potentially providing an access to the – so far forbidden – energy region starting right at the particle thresholds.

2.4 Laser spectroscopy of rare isotopes with the TSR

Laser spectroscopy provides model independent measurements of the nuclear moments, spins and changes in charge radii [37,38]. Nuclear moments are sensitive to the configuration of the wave function and when compared with the predictions made by shell-model calculations, can provide a deeper understanding of nuclear structure [39].

This makes laser spectroscopy extremely powerful for studying the evolution of nuclear structure with neutron excess. Initial surveys of the neutron separation energy from mass measurements have provided evidence for the erosion of established magic numbers such as $N = 20$ in the neutron rich sodium and magnesium isotopes [40]. Laser spectroscopy experiments of magnesium have measured the spins, magnetic moments and changes in mean square charge radii [41–43], which have provided compelling evidence for a strongly deformed intruder ground state in ^{31,33}Mg. The migration of single particle states in the neutron rich copper isotopes [44–46], is understood to be due to the monopole term in the residual interaction. This has motivated several laser experiments to find the inversion between the proton $f_{5/2}$ and $p_{3/2}$ ground state, now established to occur in ^{75}Cu and ^{81}Ga [47,48]. The measured magnetic moments have also demonstrated possible shell quenching of the $Z = 28$ gap as $N = 50$ is approached in ^{77}Cu [49,50].

Although there has been a great deal of progress in the field, large gaps still remain in the nuclear chart that have yet to be studied with laser spectroscopy. This is partly due to production difficulties at on-line facilities such as ISOLDE but also due to the presence of atomic structures that cannot be probed with modern laser spectroscopy.

The TSR presents an excellent opportunity to study difficult cases previously inaccessible at ISOLDE and provides several advantages over existing laser spectroscopy techniques [51,52]. The transitions that have rest frame wavelengths in the vacuum ultraviolet (which makes them difficult to probe) will be Doppler shifted by up to 30 nm at 10 MeV/A. By partially stripping the ion in the REX-EBIS it is possible to preferentially populate metastable states with transitions that can be probed by lasers. Additionally the TSR could be used to study elements that can only be efficiently produced at ISOLDE through chemical separation techniques [53], since the REX-EBIS will break up molecular beams during the charge breading process [54]. The recirculating beam in the TSR offers a significant gain in experimental efficiency, since the same ions can be probed many times. In principle a single ion stored in the ring for 1 s will circulate 10^5 times. Laser spectroscopy of cooled stored beams at HIE-ISOLDE builds on the trapping and bunching methodology developed in Jyväskylä and recently introduced to ISOLDE [55,56]. This complements the parallel developments for the LASPEC project at the future FAIR facility [57].

The attainable resolution within the TSR is determined by the longitudinal momentum spread of the heavy ion beam, which is typically $\delta p/p = 6 \times 10^{-5}$ and translates to a line width of $\delta\nu \sim 2$ GHz [51]. The hyperfine splitting of highly charged ions is typically between one and two orders of magnitude greater than this. For many of the possible cases transitions in deep ultraviolet will used, which will require minor modification of the light collection region previously used in the TSR [51]. From previous work an initial experimental efficiency of 0.1% can be expected, which is comparable to standard laser techniques [38].

The programme of laser spectroscopy is focused on cases that cannot be studied with low energy laser spectroscopy techniques, such as neutron rich carbon, nitrogen, oxygen and boron isotopes. This in principle will open up investigations into the recently proposed magic number of $N = 16$ [58] centred about the double magic nucleus ^{24}O [59,60]. Initial stage proof of principle with stable beams of partially stripped ions will be required before on-line measurements can be carried out. This stage of the project will also investigate the possibility of precisely measuring the isotope shift in light mass elements using the TSR for charge radii determination.

2.5 Capture reactions for the astrophysical p-process

Most of the elements beyond iron are produced via neutron-induced reactions, mainly neutron captures. But there are about 35 proton-rich nuclei between Se and Hg,

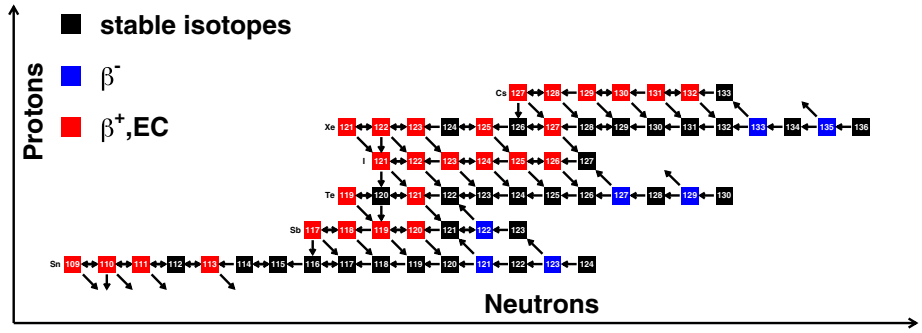

Fig. 3. Reaction network during the p-process nucleosynthesis between Sn and Cs for $T_9 = 2.4$. The most important reactions are shown for $T_9 = 2.4$. The p-process network is dominated by (γ, n) reactions. Other reactions are shown, if they are dominating. See [62] for more details.

which can neither be produced by s-process (slow neutron capture) nor by the r-process (rapid neutron capture). These nuclei are attributed to the p-process (proton-capture), which requires high temperatures of about 2-3 GK. In such an environment the reaction flow is carried by photo-dissociation processes, that is by (γ,n), (γ,p), and (γ,α) reactions. Since high temperatures are needed, the presently favored sites for the p-process are the explosively burning O/Ne layers in Supernovae of type II, where temperatures of $2–3 \cdot 10^9$ K are maintained for about 1 s at densities of $\approx 10^6$ g/cm^3 [61]. Under these conditions, especially the heavy proton-rich nuclei are produced by a sequence of (γ,n) reactions, while (p,γ) reactions are most likely dominating for lighter nuclei. When this sequence is halted about four to six mass units from the valley of β-stability by the increasing neutron-separation energies, further reaction flow is determined by (γ,p) and/or (γ,α) reactions. As the temperature decreases after the explosion, the reaction path moves back to the region of stable nuclei. This scenario involves about 2000 nuclei connected by more than 20,000 reactions and requires correspondingly large reaction networks to describe the abundance distributions following from these scenarios, see Fig. 3.

In view of the huge number of reactions, p-process studies will always have to rely on theoretical results obtained with a Hauser-Feshbach statistical model. Nevertheless, it is of utmost importance to base these calculations on a grid of experimental cross sections spread over the entire reaction network. Such data are crucial since the calculated cross sections exhibit uncertainties of several hundred percent even for stable isotopes. In case of the (γ,n) reactions, sufficient experimental data are available for constraining the model parameters close to stability so that theoretical uncertainties for stable nuclei can be reduced to a level of about 30% [63]. These uncertainties are quickly increasing though, if one moves away from stability. Compared to this rather favorable situation, rate predictions for the (γ,p) and (γ,α) reactions are completely inadequate since only a handful of experimental data for stable isotopes has been determined in or close to the astrophysically relevant energy range – the so-called Gamow window - of the p-process so far. Because of this lack of experimental information the corresponding reaction rates are typically uncertain by factors of two to three even for the stable isotopes [64].

Because of the uncertain nuclear physics input, p-process models for Supernovae of type II and Ia are capable of reproducing the p-abundances within a factor of about three [62]. Moreover, both scenarios do have problems in describing the light p-nuclei with A<100 correctly. Since the p-process in type II Supernovae is dominated by photo-disintegrations from heavy seeds, this model does not account for the relatively

large abundances of ^{92,94}Mo and ^{96,98}Ru. An alternative origin of these nuclei could be imagined via (p,γ)-reactions. The high temperatures and proton densities, which are required for these reactions to proceed with significant rates, are obtained in novae or X-ray bursters [65], where hydrogen is burnt explosively under degenerate conditions, but remixing of synthesized material to the interstellar medium is still in question for these scenarios. Another interesting scenario is the p-process during type Ia Supernovae. Recent model calculations suggest the importance of (p,γ) rates for the production of the light, proton-rich molybdenum isotopes [66–68].

Proton- and α-induced rates are therefore highly important in this context and can be directly used in p- and rp-process (rapid proton capture) networks [62,65]. They are also important indirectly for determining stellar (γ,p) and (γ,α) rates via detailed balance.

Such measurements in the astrophysically interesting energy range are already very challenging on stable nuclei, especially for isotopes heavier than iron where the p-process is located. However, only a minute part of the nuclei involved in p-process networks are stable. The majority of the isotopes crucial for the final p-process abundance are unstable.

The most promising approach to determine the desired reaction rates is to produce the isotopes in Radioactive Ion Beam (RIB) facilities and to investigate the reactions in inverse kinematics. Bombarding a hydrogen or helium target with the isotopes under investigation has the main advantage that no radioactive sample has to be produced. If such an experiment is performed at a storage ring, the stored beam is intersected by an internal gas-jet target and the recoils from the reaction are measured with high (up to 100%) efficiency after one of the ring's bending magnets. The TSR, owing to the "pseudo"-continuous accumulation scheme is a versatile tool for such measurements. A proof-of-principle experiment has been performed at the ESR ring of GSI, where the cross section of the proton capture on stable ^{96}Ru nuclei (^{96}Ru$(p,\gamma)^{97}$Rh) has been measured [69]. A new proposal to investigate (p,γ) reactions in the Gamow window was accepted at GSI [70]. At GSI, in order to perform measurements in the Gamow window of the p-process, the stored ions have to be slowed down to energies below 10 AMeV. Such a procedure is time consuming and inefficient. The TSR at HIE-ISOLDE would be an ideal combination, where the post-accelerated stable or radioactive beams are injected and stored at the right energy.

The number of cases for possible studies is huge, in particular since not only reactions important for the p-process can be studied, but also (p,γ) and (p,n) reactions for the νp-process or fusion reactions important for the understanding of the different burning stages of the stars. It is suggested to start the experimental program with stable beams (e.g. ^{86}Kr, ^{112}Sn), which can also be done during proton-accelerator shutdowns. The data are hardly available and even the first experiments will have high scientific impact. The cross-sections for (p,γ) and (α,γ) reactions in the Gamow-window of the p-process are relatively high. For the first experiments, one can select the cases with cross sections in the range 0.1–10 mb and, thus, moderate intensities would be required (a few 10^5 stored ions only).

Atomic electron-stripping reactions have huge cross-sections at the required low energies of 3–5 MeV/u and are the main cause for beam losses. Furthermore, the removal of one electron causes the ions to be on the same trajectory as the desired reaction products following a (p,γ) reaction and the same holds true for the comparison of the removal of two electrons and (α,γ) reactions. This means, signal and background cannot be disentangled based on their position on the detector, but only because of the slight change in kinetic energy, which is in the order of 1–2%. Therefore, the above experiments require high atomic charge states and sophisticated particle detection systems. Fully-ionized atoms are required for elements in the Z-range $30 \leq Z \leq 70$. Such high-ionization grades cannot be achieved with the

present REXEBIS and an upgrade to higher electron densities and voltages to a so-called Super-EBIT is indispensable.

2.6 Nuclear astrophysics through transfer reactions

The use of the TSR@HIE-ISOLDE is particularly well suited for transfer reaction studies of key astrophysical resonances in explosive nuclear astrophysical scenarios such as novae, X-ray bursters, and Supernovae. In many instances, one is dealing with relatively light heavy ion beams which can easily be produced fully stripped, and which have lifetimes greater than 1 second, since in general the most important individual reactions involve radioactive isotopes close to, or adjacent to, the valley of β-stability.

Many key explosive astrophysical reactions are too weak to be measured directly in the low-energy Gamow burning regime, and require an indirect approach for progress to be made. For such studies, the transfer reaction is used to populate the states of interest corresponding to resonances in the compound nucleus produced by the astrophysical fusion reaction, or populates known analog states in the mirror nucleus. A key experimental aspect is that such resonances often reside in regions of moderately high level density where high resolution spectroscopy is essential. The use of high quality, pure beams from the TSR@HIE-ISOLDE in combination with highly segmented Silicon detector systems, means that such resolution can be achieved ($\sim$20 keV FWHM has already been demonstrated for such arrays for inverse (d,p) studies). A further important benefit for such studies is the use of pure, thin targets. In normal inverse kinematic experiments a solid CD_2 target is for example commonly used for (d,p) studies, where there is increased multiple scattering and straggling of the heavy ion in the thick target, and importantly, background reactions on the ^{12}C in the target. The use of thin pure gas targets in combination with a ring means that high luminosity, high resolution as well as high detection efficiency (up to 100%) can be achieved with no background reactions.

The (^{3}He,d) reaction can serve as a surrogate for the (p,γ) reaction, where it can be used to determine the proton spectroscopic factors of key low-lying resonances unable to be measured directly. For resonances in such reactions the proton spectroscopic factor is often the key uncertainty in determining the astrophysical reaction rate. Angular distribution measurements of transfer reactions also serve to identify these key states, which correspond to small angular momentum transfers (and hence small centrifugal barriers) in the astrophysical reactions. Examples of important (p,γ) reactions are, $^{18}\mathrm{F}(p,\gamma)$ for breakout from the hot CNO cycles in novae explosions, $^{26g}\mathrm{Al}(p,\gamma)$ for destruction of the cosmic gamma-ray emitter ^{26g}Al in Wolf-Rayet stars, and the corresponding isomeric reaction $^{26m}\mathrm{Al}(p,\gamma)$ which is important for the observations of excess ^{26}Mg in meteoritic inclusions associated with core collapse supernovae (CCSN) sites [71–73]. In the latter case, there may be the unique possibility of purifying the isomer component of the beam in the TSR.

In some instances it may be necessary to use the (d,p) reaction to populate analog states in the mirror nucleus to determine spectroscopic factors and the identity of key states. For example, the $^{18}\mathrm{F}(d,p)^{19}\mathrm{F}$ reaction can be used to study analogues of key states in the mirror nucleus, ^{19}Ne, corresponding to resonances in the $^{18}\mathrm{F}(p,\alpha)^{15}\mathrm{O}$ reaction. This reaction occurs in the hot CNO cycles in novae, and is thought to be primarily responsible for the destruction of the currently unobserved cosmic gamma-ray emitter, ^{18}F.

Transfer reactions provide an alternate route to study the decay branches of key astrophysical resonances. A major challenge for the field of explosive nuclear astrophysics is to determine the $^{15}\mathrm{O}(\alpha,\gamma)^{19}\mathrm{Ne}$ reaction rate for a single key resonance.

This rate controls the astrophysical conditions for breakout from the hot CNO cycles into the rp-process in X-ray bursters. The rate critically depends on the α-branching ratio of the key resonance thought to be $\sim 10^{-4}$ [74]. One approach for example would be to use the ^{18}Ne$(d,p)^{19}$Ne reaction to feed this state, ^{18}Ne is of course also important as a potential source of neutrinos for the beta-beam project at CERN.

Finally it should be noted, that some of the key isotopic beams have long half-lives well in excess of 1 second, and are relatively light and fully stripped. Therefore, such long-lived beams would be ideally for luminosity increases by the use of stacking on the TSR.

2.7 Nuclear structure through inelastic scattering and transfer reactions

Understanding the evolution of nuclear structure far from stability is a central challenge in contemporary nuclear physics. Measurements on exotic nuclei have been performed in the last twenty years employing various experimental tools, revealing a number of unexpected phenomena: new nuclear topologies [75,76], changes in magic numbers [41,45,77,78], shape coexistence [79]. Theoretical developments have started giving an insight on these observations [80–82], identifying the role of the different terms of the underlying nucleon-nucleon interaction [83,84]. There is now a need for detailed nuclear structure information on the states of the key nuclei located in the vicinity of shell closures. Inelastic scattering and transfer reactions can provide such information. Measurements could be performed either in the storage ring, by using an internal gas jet target, or by extracting a cooled, essentially DC beam with optical qualities much superior to those of the direct HIE-ISOLDE beam.

We refer further to Sect. 2.7.3 for a discussion of the technical aspects; here we focus on the physics motivation.

2.7.1 Inelastic scattering and Coulomb excitation

Inelastic scattering on protons gives access to transition densities. Protons interact with both protons and neutrons in the nucleus, whereas Coulomb excitation on a heavy-Z partner or lifetime measurements probe directly only the proton density distributions. The combination of the two types of measurements can disentangle proton and neutron contributions to excited states [85,86]. This could be particularly important in very neutron-rich nuclei, where large collective matrix elements may be dominated by neutron motion, decoupled from protons and charge. Coulex and inelastic scattering therefore provide highly complementary probes of nuclear structure across all regions of neutron excess. Such reactions would be performed with a H_2 gas jet target in inverse kinematics, with identification of the reaction channel relying on the detection of the recoil protons.

Coulomb excitation studies could also benefit from the use of the TSR. Here the preferred scheme is by using the extracted, cooled beams from the ring. In the heavier mass region, REX-ISOLDE has recently demonstrated a unique capability to post-accelerate mass 200 and heavier ions. A programme of Coulex measurements of the mid-neutron shell Hg, Pb, Po and Rn isotopes has been successfully initiated. Here these neutron-deficient nuclei have been schematically described as oblate ($\beta \approx -0.15$) or spherical ground states coexisting with prolate ($\beta \approx 0.25$) structures, separated by energies less than 1 MeV. In the octupole $Z \sim 56$, $N \sim 88$ and $Z \sim 88$, $N \sim 134$ regions it is now possible to provide more precise information on the nature of the octupole collectivity through the Coulomb excitation of radioactive beams. Recent measurements have demonstrated that $B(E3)$ values of nuclear transitions, a direct measure of octupole correlations, can be measured in nuclei such as

^{224}Ra. In both of these examples the combination of the high quality of the cooled beams that are extracted from the storage ring together with advances in particle spectrometer design (particularly the HELIOS concept, see Chapt. 2.7.4) allow the nuclear state population from (mostly) single-step excitation be directly measured. This circumvents many of the problems that beset the conventional particle-gamma measurements, particularly where there is significant internal conversion and feeding from higher-lying states.

2.7.2 Transfer reactions

Single-nucleon transfer reactions are particularly useful as a spectroscopic tool due to their selectivity in favour of the population of single-particle (or hole) levels. The excitation energies of the different states in the nucleus under study can be obtained directly from the measured energy spectra. The Q-values measured for the ground state in these spectra sometimes provide the first determination of the mass in the case of very exotic nuclei, at the limit of drip lines or, for light nuclei, even beyond. While the angular distributions of the differential cross sections depend on the transferred angular momentum, and therefore bring information on the spin and parity of the state, the absolute values of these cross sections are directly related to the spectroscopic factors and thus to the structure of the states.

At ISOLDE, interesting possibilities are provided by the availability of beams of exotic nuclei in specific regions of the nuclear chart. The use of the TSR becomes competitive when the accumulation and recirculation of the beam compensates the lower thickness of an internal target. This requires half-lives of the order of a second or more, thus nuclei not in the immediate vicinity of the driplines. Possibilities start to open up in the Ni region, where, with the intensities currently available at REX-ISOLDE, the monopole migration and onset of collectivity between N=40 and N=50 can be studied in detail. Measurements, aiming at the spectroscopic factors and thus the single-particle structure of the first excited states in the Ni isotopes, could extend to ^{70}Ni(d,p) and possibly further.

Single-particle states outside N=50 could be reached by employing the most neutron-rich Zn, Se and Kr beams. For example, the effects of the tensor term of the monopole interaction [83] can be studied by measuring the position of the neutron single-particle levels just above the N=50 shell closure: the ordering of such levels in the isotone chain above ^{78}Ni is influenced, through the tensor interaction, by the removal (going towards more exotic nuclei) of the protons in the $f_{5/2}$ orbital. A key measurement is the ^{80}Zn(d,p) transfer. With respect to the conventional setup, the storage-ring technique would probably not ensure a higher luminosity ($T_{1/2}(^{80}\mathrm{Zn}) = 0.545\,\mathrm{ms}$), however the improved energy resolution may be important in the detection of the possibly low-lying first-excited state; in addition, a higher beam purity may be obtained through cooling in the ring.

More in general, on the neutron-rich side, (d,p) reactions can be used to investigate the shell evolution towards the nuclei of the astrophysical r-process. Essentially the same topics are at play in the region around ^{132}Sn, where measurements could be performed on Sn isotopes beyond the N=82 shell closure. For example for the ^{134}Sn(d,p) reaction, similar experimental conditions (comparable luminosity but better purity and resolution) are encountered as for the reactions discussed in the Ni region. Here the aim is to investigate the evolution of the $2f_{7/2}$–$3p_{3/2}$ energy difference. On one side, one could expect the development of a N=90 gap, in analogy with the behaviour of the $1f_{7/2}$–$2p_{3/2}$ N=28 gap in Ca isotopes (due to the attractive monopole interaction between neutrons filling the same orbital [81], lowering the $f_{7/2}$

level). However, this could be counter by a repulsive tensor interaction between the protons in $g_{9/2}$ and the neutrons filling the $2f_{7/2}$ orbital.

Also around the Z=50, N=82 shell closure, there will be the opportunity to study two-particle, two-hole and particle-hole states immediately in the vicinity of ^{132}Sn to extract two-body matrix elements, as has been done for ^{208}Pb [87]. This would quantitatively characterise the effective NN interaction in this neutron-rich environment for the first time, provided essential input for shell-model and mean-field calculations and furthering out understanding of nuclear structure in this region. This can be achieved by proton- and neutron-adding and -removing reactions with beams and reactions such as ^{133}Sb(d,t), (d,p), (^{3}He,d), (α,t) and similar with beams of ^{131}Sn, ^{133}Sn, and ^{131}In, all produced with sufficient intensities and life times. Such measurements can be achieved with the anticipated Q-value resolution with extracted TSR beams and appropriate charged-particle spectrometer, such as HELIOS (Sect. 2.7.4).

Around ^{100}Sn, the study of states in nuclei is relevant for the role of isospin symmetry in the nuclear structure. The proton and neutron shell closures can be studied with (d, p), (^{3}He,^{4}He) and (^{3}He,d) reactions. Neutron pick-up reactions have a strong negative Q-values, thus the high beam energy (10 MeV/nucleon) is important. The half-lives of the most exotic nuclei available (Sn and In isotopes), on the other hand, are much longer than ≈1 s, possibly providing a higher luminosity.

Unique opportunities are present in the region of the Pb nuclei, produced at ISOLDE by spallation reactions. The physics motivation has been illustrated in the section about Coulomb excitation (2.7.1). On the neutron-deficient side, transfer reactions could give an insight on the issue of shape coexistence in those nuclei, with possible studies as far as ^{186}Pb, while the somewhat heavier neutron-rich region would allow to probe the single-particle states responsible for octupole deformation. More specifically, one could probe the hole states in Tl via Pb(d,^{3}He) reactions and the particle states in Bi via Pb(^{3}He,d) or (α,t) from say ^{186}Pb to say ^{208}Pb. This would map the evolution of the respective single-particle states, tracking the $h_{9/2}$ and $i_{13/2}$ proton shells above $Z = 82$ as neutrons fill similar high-j orbits in the Pb cores.

Favourable experimental conditions are found closer to the valley of stability, where again details of the nucleon-nucleon interaction can be investigated for some specific cases. For example, the isotonic chain $N = 83$ has been used to investigate the separation between the centroids of the neutron $i_{13/2}$ and $h_{11/2}$ single-particle levels [88], as protons fill the $g_{7/2}$ orbital (in stable nuclei from Ba to Sm). The energy difference was found to be decreasing, consistently with the effect of the tensor interaction between protons and neutrons in those orbitals (see Fig. 4). It is interesting to extend the measurements above the valley of stability to nuclei where protons start to fill the $h_{11/2}$ orbital, for which the sign of the tensor interaction would reverse causing a decrease of the neutron $i_{13/2}$–$h_{11/2}$ gap. Since the levels of interest are highly fragmented, due to the coupling with vibrational excitations of the cores, measurements are needed of spectroscopic factors with beams such as ^{146}Gd and heavier $N = 82$ species (^{148}Dy, ^{150}Er). Similar measurements could also be made outside $N = 126$ using ^{206}Hg, ^{212}Rn and ^{214}Ra beams. All these species are readily available at ISOLDE.

2.7.3 Technical aspects in reaction studies with the TSR

The TSR at ISOLDE would represent the first example of a storage ring coupled to an ISOL facility. The use of an internal (gas-jet) target requires accumulating and recirculating the beam, to compensate for the lower target thickness; for this, a lifetime of the beam of about 1 s is sufficient. However, a reaction measurement in the

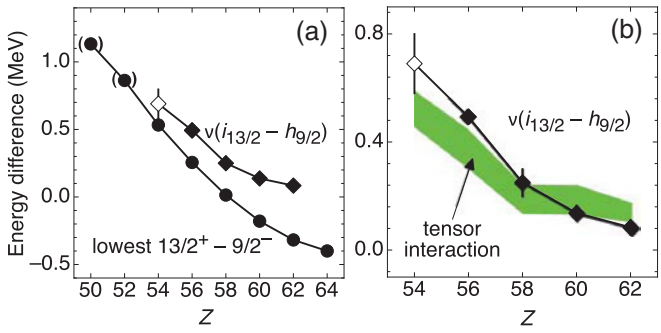

Fig. 4. (Adapted from [89]) Differences in experimental centroid energies of neutron- $i_{13/2}$ and $h_{9/2}$ strength (diamonds) compared to: (a) the energy differences between the lowest $13/2^+$ and $9/2^-$ states (circles), and (b) predictions of a $\pi+\rho$ tensor interaction (green band). The width of the band is generated by experimental uncertainty in the proton occupancies.

ring would also benefit in precision from the high quality of the beam and the lack of straggling, and in background reduction from the absence of carbon in the target. The requirement of a sufficiently long lifetime means that the ISOL technique can be fully exploited in this combination, using the advantages offered in terms of beam intensities and phase-space density for a number of isotopes. In addition, transfer studies need to be performed both at high (some hundreds MeV/nucleon) and low energy (5–10 MeV/nucleon) in order to probe the wave functions in all spatial regions. For the lower energies, post-accelerated beams will be available at HIE-ISOLDE, thus avoiding the losses due to a slowing-down procedure needed for in-flight produced beams.

Execution of an experiment in the storage ring using an internal gas target, with respect to using a direct beam and an external target, must consider a number of technical issues. Detailed studies have been made in the past, however mostly concerning beams circulating at higher energies (for example, see Ref. [90]). For the TSR, and the comparison with the direct beams from HIE-ISOLDE, the main features are summarised in Table 2. Here we discuss some of those issues, while in the following Sect. 2.7.4 we consider the use of extracted beams from the TSR.

The energy of post-accelerated beams at HIE-ISOLDE, 10 MeV/nucleon, is well-suited for transfer reaction studies. Good matching conditions can be obtained in (d, p) or (p, d) reactions to orbitals with low angular momentum, while orbitals occupied in heavy nuclei can be better populated in stripping or pick-up reactions involving α particles. As already mentioned in the introduction to this Chapt. (2.1), the time structure of the beams from the REX low energy part, with short bunches of $\approx$100 μs that can be repeated with a few times per second or lower, matches well the injection into the TSR. Between two injections the beam can be cooled in the ring reaching a very small energy spread. This property could be used to perform further purification from isobar contaminants: the goal is a resolution of 1 in 10^4 using mass selective acceleration (Chapt. 4.9.1).

The maximum magnetic rigidity allowed in the TSR is 1.5 Tm. At an ion energy of 10 MeV/nucleon, this translates into ionization states higher than the ones presently achieved in the REXEBIS charge breeder, especially on the neutron-rich side and for nuclei beyond $Z \approx 50$. Those charge states could be reached by an upgrade of the REXEBIS, or possibly using a stripping foil (with varying efficiencies).

In the TSR, gas-jet targets of H_2, d, and ^{3,4}He would be used. Present target technology allows reaching thickness of the order of 10^{14} atoms/cm^2 [91], however in many cases a lower thickness should be used to prevent a fast loss of the beam

Table 2. Comparison between the main characteristics of typical reaction measurements when performed either after HIE-ISOLDE or in the TSR.

	HIE-ISOLDE	HIE+TSR
Beam structure	macrostructure	DC
Beam size	few mm	≈mm
Beam energy resolution	1.4×10^{-3}	1×10^{-4}
Transverse emittance	0.5 mm mrad	0.03 mm mrad
Loss due to beam cooling	None	(20% to 40%)[a]
Beam purity	A/q contamination possible	(1 in 5000)[b]
Target z-extent	negligible	(5 mm)[c]
Target thickness (background)	≈100 μg/cm^2	negligible
Target purity	e.g. CH_2	pure gas
Luminosity[d]	nominal value 100	>4 for $50 < A < 200$
Charge state requirement	$A/q \approx 4$	($A/q \approx$ 3-4)[e]
Vacuum requirements	SHV	UHV
Reaction timing	requires buncher/chopper	from beam-like detection

[a] Improvement possible – goal is 10% and 1–2 cm diameter for un-cooled beam.
[b] Improvement possible – goal is 1 in 10^4; investigate laser ionisation.
[c] Improvement possible – goal is 1 mm.
[d] The luminosity L is defined, for HIE-ISOLDE, in terms of the beam intensity I_{beam} and the target thickness T_{target}, as $L = I_{\text{beam}} \times T_{\text{target}}$. For the TSR, L also depends upon the revolution frequency f and beam lifetime τ: $L = I_{\text{beam}} \times T_{\text{target}} \times f\tau$. See also Table 1.
[e] Requires EBIS development for heavier ions.

through atomic charge exchange reactions (see Table 1 in Chapt. 2.1). The longitudinal extension of the target is also an issue, and should be kept as small as possible for a better definition of the interaction point. These issues are discussed further in Sect. 4.14. The reactions of interest typically demand the detection of the outgoing light particle and possibly gamma rays in coincidence. In some cases, beam-like particles could be sufficiently separated from the circulating beam and detected before, within or after a bending element. A number of solutions for combining detector arrays with the ultra-high vacuum (UHV) requirements of a storage ring have been investigated, proposed and recently tested by the EXL collaboration [92–95]. In particular Ref. [94] reports the results of a series of tests using various semiconductor and scintillator detectors, also placed at a short distance from the beam axis, in combination with a jet target. In addition, the possibility of housing detectors in fast-retractable pockets is demonstrated. This latter application is relevant for a detection setup in the TSR, considering the large size of the beam before cooling. A setup for use in UHV is described in Ref. [95], where double-side silicon detectors separate the UHV from a standard vacuum where outgassing components are located. This concept was tested and its feasibility proven. While more development is certainly necessary for a full array, also taking into account the different requirements at the HIE-ISOLDE energies, expertise is clearly available in the collaboration.

Because of the very good beam-energy definition and the absence of straggling in the target, a superior energy resolution is expected in reaction measurements with an internal target: the remaining contributions would be the intrinsic resolution of the charged-particle detectors and the spatial resolution affecting the kinematical reconstruction; for the latter, good collimation of the beam on the target is necessary. An external array like Miniball can be used for the detection of gamma rays, provided sufficient coverage can be reached around the instrumentation needed by the gas target. As demonstrated in recent transfer reaction measurements at REX-ISOLDE

[96], gamma rays can be very useful to reconstruct the decay scheme of the populated nucleus and thus put further constraints on the spin-parity assignments of the states.

2.7.4 External spectrometers

The superior properties of the cooled extracted beam from the TSR compared to the direct beam from HIE-ISOLDE (see Table 2) will be of benefit to many classes of external spectrometers that can exploit these qualities. Several concepts for spectrometers have been discussed by the HIE-ISOLDE user community and have already been presented to the INTC as Letters of Intent [97]. Mass separators [98] similar to the EMMA device being constructed at TRIUMF and light-charged particle arrays such as GASPARD [99] will achieve their optimum performance if the incident beam has the superior energy spread, transverse emittance and x-y extent of the cooled beam from the TSR.

The helical orbit spectrometer HELIOS [100] uses a large-bore superconducting solenoid to provide a ∼3 T uniform magnetic field, in which the outgoing ions execute helical orbits and return to the beam axis where their position, time of flight, and energy are measured. The resulting excitation energy spectra are free from kinematic compression, yielding optimum Q-value resolution. HELIOS will also benefit from the excellent energy resolution, transverse emittance and small beam size of the extracted beam, and will allow (using several widely spaced, thin targets) Q-value resolutions as low as 20 keV be achieved for (d,p) reactions. Resolutions approaching 50 keV will also be possible for Coulomb excitation of heavy-ion radioactive beams by a cascade of ∼10 ultra-thin carbon targets.

The active target detector, ACTAR-TPC [101], a gaseous ionization detector where the nuclei of the gas atom are also the target nuclei, has a very good geometric efficiency, a low detection threshold and excellent tracking capabilities (allowing the measurement of angular distributions). Particle identification is possible, and a large target thickness is possible without loss of resolution. In the case of short-lived or unbound reaction products, the decay and its products can be detected in the gas volume itself. The thickness of the target allows beams as low as 100 particles per second to be employed – giving access to the most exotic systems. However for more intense beams dead-time will reduce the efficiency of the device; the quasi-DC nature of the extracted TSR beam, as compared to the highly pulsed beam from HIE-ISOLDE, will reduce these losses.

2.8 Long-lived isomeric states

Nuclear isomers are metastable excited states with half-lives ranging from ns to years [102]. For isomeric beams that live long enough to be electron cooled, that is with half-lives greater than 1 s, it is expected that the TSR at ISOLDE will offer unique opportunities for novel physics experiments. These fall broadly into three categories, discussed below. It is notable, that already there are known [103] to be more than 70 isomers with excitation energy, $E > 500$ keV, and $T_{1/2} > 1$ s, and more will be discovered in the future. Only a few examples will be used here to illustrate the range of possibilities.

(i) *Exotic isomers yet to be identified*
The vast majority of isomers arise from the individual-particle properties of nuclei with the ability to generate high angular momentum at relatively low excitation energy. A leading, well-known example is the spin-16, 31-year isomer

at 2.4 MeV in ^{178}Hf, which has a stable ground state, and there are predictions [102] for analogous long-lived isomers in neutron-rich hafnium isotopes. Indeed, a $T_{1/2} \sim 12$ minute isomer at 2.5 MeV in ^{184}Hf was recently discovered [104] in the ESR at GSI on the basis of only a few stored particles. This was uniquely observable in a storage ring, where no decay was required for the determination of its existence and excitation energy. Further experiments will be performed to search for a predicted spin-18 isomer in ^{188}Hf. Here the sensitivity of the storage ring spectrometry to single stored ions is a clear advantage (see also Refs. [105,106]).

Similar experiments could be carried out with the TSR at ISOLDE, where isotopic yields are likely to be greater than at GSI, with the condition that the ion-source chemistry must be favourable. Pushing further into the neutron-rich domain will open up opportunities to search for signs of, for example, $N = 126$ shell quenching as protons are removed the $Z = 82$ closed shell, which may be needed to explain elemental abundances arising from r-process nucleosynthesis. Isomer excitation energies in magic nuclei give characteristic measures of shell gaps and residual interactions.

Another intriguing and so-far unobserved possibility is that of neutron radioactivity, where the angular-momentum barrier of high-spin isomers may lead to an unbound neutron having an extended half-life. In a storage ring, the neutron emission could be uniquely established from the change in the revolution frequency, without the need to observe the emitted neutron itself. (A comparable situation has been successfuly exploited with proton decay − without observing the proton [107].)

(ii) *Nuclear reactions with pure isomeric beams*
The ability to form purified isomeric beams, making use of either a scraper or dielectronic recombination, will open up remarkable possibilities for novel reaction physics. Scenarios discussed in this document for reactions with radioactive beams in their nuclear ground states can then also be applied to isomeric states, including Coulomb excitation and particle transfer. With the blocking of pairing correlations in isomeric multi-particle configurations, as well as the involvement of high-spin orbitals, the nuclear reactions will have exceptional features, and unusual states will be populated – especially in transfer reactions.

Purified and accelerated isomeric beams of ^{68m}Cu and ^{70m}Cu have already been produced at ISOLDE, using laser resonance ionisation [108], but the technique remains element specific. With the TSR at ISOLDE, the possibilities will be dramatically expanded.

One interesting study will be that of isomer Coulomb de-excitation, as already observed with ^{68m}Cu [108]. The electromagnetically-induced release of isomer energy is a controversial topic [109] that could lead to novel energy-storage devices, but reliable measurements have been rare. This situation is set to change with the TSR at ISOLDE, where it will be possible to make detailed investigations of the de-excitation of a large range of isomers.

(iii) *Exploiting isomers to study the atomic/nuclear interface*
The combination of purified isomeric beams and a high-quality electron target will open further avenues for novel physics. Related to the discussion of Coulomb interactions (see previous subsection) the atomic-electron orbits also interact with the nucleus electromagnetically. Nuclear excitation by electron capture, the so-called NEEC process, has never been observed, yet it is predicted to have large effects in certain circumstances [110–112]. The challenge is to establish the appropriate atomic/nuclear environment, and the TSR is expected to provide this. Further discussion of the importance of the

atomic/nuclear interface is given elsewhere in this document, in connection with dielectronic recombination.

The role of isomers in this context may be to provide an identifiable signal: a small energy change from an atomic interaction can lead to substantial energy release from an isomer. This scenario is simply not available from a nuclear ground state. One such case may be ^{128}Sn, where a long-lived isomer at 2.1 MeV could be excited to a level just 30 keV higher, which can then bypass the isomer in its decay. Thus, a 30 keV excitation can release 2.1 MeV.

2.9 Atomic effects on nuclear half-lives

The storage ring facility at HIE-ISOLDE will allow experimental investigations of radioactive decays of ions in various atomic charge states up to bare nuclei. One of the clear motivations for such experiments is stellar nucleosynthesis in stars, where, due to the high temperatures and densities, the nuclides involved in the s-, r-, rp-, etc processes are, as a rule, not in a neutral atomic charge state but highly ionized [113,114]. One example is the EC-decay of ^{7}Be, which is discussed in detail in Sect. 2.2 [24].

Furthermore, highly-charged atoms offer the possibility to study decays under "clean" conditions. For instance, by preparing the parent ion in a simple, well-defined quantum state, as a bare, hydrogen- or helium-like atom, the effects due to bound electrons not directly involved in the decay itself (electron screening, re-arrangement of atomic shells after the decay, shake-off effects, etc. [15]) can be disentangled.

Besides the fundamental aspects of such studies, an understanding of how the high atomic charge states modify the nuclear decay properties with respect to neutral atoms can have a range of applications, like, e.g., the transmutation of nuclear waste. Scientists have tried to manipulate nuclear decay rates ever since radioactivity was discovered. However, only small modifications of up to a few percent have been observed in atoms by changing the environmental parameters such as pressure, temperature, or electromagnetic fields [115]. It has been predicted [113,114], that the decay properties of highly-ionized nuclides can be altered dramatically: Decay modes known in neutral atoms can become forbidden or the new ones can be opened up. It is obvious, that the electron capture and electron conversion decays are disabled in the absence of orbital electrons in fully-ionized atoms. It has been shown experimentally, that half-lives of isomeric states can be dramatically prolonged in bare nuclei [104,116,117]. The latter provides directly the information on conversion coefficients [116] and can be useful for studying weak γ-ray transitions [117].

Bound-state β^- decay (β_b^-), a decay channel where the emitted electron can be captured into atomic inner-shell vacancies instead of being emitted into the continuum, can become significant in highly-charged ions. Indeed, the largest observed lifetime modifications are due to this decay mode. It was for the first time experimentally verified in the ESR for fully-ionized ^{163}Dy and ^{187}Re nuclei [118,119]. A highly desirable but still missing experiment is the determination of the β_b^- decay probability of bare ^{205}Tl^{81+} nuclei [120], which is important for solar neutrino physics [120] as well as for the "final" s-process abundances prior to the formation of the solar system [121]. We note, that this experiment has been recently proposed and approved for the ESR facility at GSI [122].

The branching ratio of bound to continuum β^- decay in neutron-rich nuclei, β_b^-/β^-, is analogous to the EC/β^+ ratios in neutron-deficient nuclei. Up to now, β_b^-/β^--values have been measured only for the heavy ^{205}Hg [123] and ^{207}Tl [124] nuclei, where the experimental value for ^{205}Hg^{80+} is almost 25% lower than the calculations [114]. TSR at ISOLDE can be employed to measure β_b^-/β^--values as a

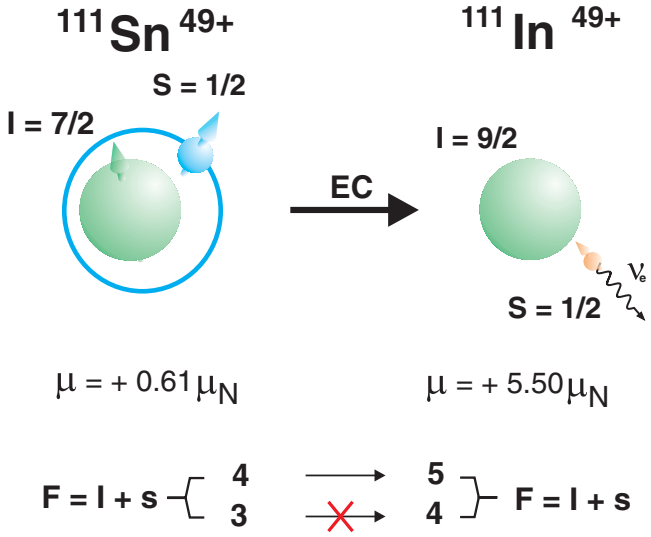

Fig. 5. Decay scheme of neutral ^{111}Sn as taken from Ref. [8]. ^{111}Sn has a half-life of 35.3(6) min, a 92.9% branch to the ground state of the daughter ion, a Q_{EC}-value of 2445(8) keV, and an EC-branch to the ground state of ^{111}In of about 63%.

function of decay energy, element number, spin-parities of the parent and daughter nuclides, thus constraining the theory which is essential for astrophysical calculations of nucleosynthesis processes [114].

The data on nuclear decay of hydrogen- (H-like) and helium-like (He-like) ions are still very scarce. Up to now there have been only two experiments performed studying the EC decay of H-like and He-like ions [2], in which the g.s–g.s. allowed Gamow-Teller transitions ($1^+ \rightarrow 0^+$) in ^{140}Pr and ^{142}Pm ions have been accurately measured [17–19,125]. It has been observed that the EC decay rate in H-like ions is by about 50% larger than in He-like ions and even larger than in neutral atoms. It has then been shown theoretically, that the EC-decay rate is highly-sensitive to the population of hyperfine states [20,21]. A possible impact on the EC-decay of ^{7}Be is discussed in Sect. 2.2.

Systematic investigations of EC-decay as a function of atomic charge states and of spin-parities for the parent and daughter nuclei can be conducted at the TSR@HIE-ISOLDE. Such experiments can be used to address the electron screening in beta-decay, or employed as a thermometer for the ion-beam interacting with electrons or gas-jet particles. Furthermore, long-lived isotopes decaying within a few days to 100 kilo-years by orbital electron-capture (e.g., ^{56}Ni ($T_{1/2}$=6 d), ^{57}Co($T_{1/2}$=272 d) are frequently used in cosmic ray physics to estimate the time between the nucleosynthesis in stars and the acceleration [126,127]. An interesting option can be the selective population of hyperfine states with a laser beam (a proof of principle has been done in the ESR [128]).

The number of candidates for the studies at the TSR is huge. One well-suited nucleus for a possible "first-day" experiment is ^{111}Sn (see Fig. 5) [129], which decays by an allowed Gamow-Teller transition ($\frac{7}{2}^+ \rightarrow \frac{9}{2}^+$) to ^{111}In atoms. H-like ^{111}Sn ions have two hyperfine states with $F_i = 7/2 \pm 1/2$, where (i) indicates the initial (parent) state. In the final (daughter) state (f), the bare ^{111}In and an emitted neutrino have also two hyperfine states with $F_f = 9/2 \pm 1/2$ (forbidden decays can be neglected in the present context). Only the transition conserving the total angular momentum F is allowed, that is the transition between the states with $F_i = F_f = 4$. However, the

magnetic moment of ^{111}Sn is positive, which yields $F_i = 3$ as the hyperfine ground state. Thus, the ground hyperfine state of H-like ^{111}Sn ions can *not* decay by an allowed electron capture. This can successfully be used to study forbidden decays or to address electron screening in continuum β-decay (see also [130]). The long half-live of ^{111}Sn atoms $T_{1/2}$=35.3 min allows longer charge breeding times. The estimated ISOLDE yield is about 10^9 particles/s, which is higher than required in this case. However, the present REXEBIS is only capable of achieving charge states lower than $q_{\rm limit}^{Z=50}$=39+, which is insufficient ($q_{\rm limit}$ is the maximal achievable charge state for a given Z, determined by the condition that the ionization energy for a certain $q \rightarrow q+1$ becomes larger than the energy of the electron beam). An upgrade of the REXEBIS would thus be required.

Another candidate could be ^{64}Cu ($T_{1/2}$=12.7 h) [17]. Besides a 37% β^--branch, this nucleus decays via an allowed Gamow-Teller transition ($1^+ \rightarrow 0^+$) to the ground state of stable ^{64}Ni atoms. We note, that the β^--decay in bare and H-like ^{64}Cu ions has a significant β_b^--branch. In contrast to ^{140}Pr, ^{142}Pm and ^{111}Sn ions, the magnetic moment of ^{64}Cu nucleus is negative, yielding $F_i = 3/2$ as the ground hyperfine state of H-like ions. Since the final state has only one hyperfine state with $F_f = 1/2$, the conservation of the total angular momentum prevents any allowed ($l_{\nu_e} = 0$) EC-decay from the ground state of H-like ^{64}Cu ions.

We note, that EC decay of lithium-like ions has never been addressed up to now and can be done at the TSR.

The storage ring lifetime spectroscopy (as shown in numerous ESR experiments [2]) allows redundant measurements: The number of parent ions is continuously monitored with non-destructive Schottky technique and the number of daughter ions is either also monitored simultaneously or counted by a particle detector. A few decay branches (e.g., EC and β^+) can be unambiguously identified and simultaneously investigated.

The ISOL production methods allows achieving unprecedentedly high intensities for a range of elements, which, in combination with the accumulation scheme developed at the TSR, will provide unique experimental conditions. The latter will allow the conduction of experiments that are presently very difficult or even impossible to perform at the ESR and/or CSRe storage rings.

2.10 Nuclear effects on atomic half-lives

The influence of the hyperfine interaction on atomic lifetimes was already noted as early as 1930 by Bowen, who commented on the spectroscopic work of Huff and Houston [131] on "forbidden" lines in mercury. The hyperfine interaction leads to a shortening of lifetimes of metastable levels and, correspondingly, to an enhanced associated emission of radiation. In astrophysics, this can be used for discriminating between radiation from different isotopes and, thus, for inferring isotope-dependent abundance ratios which provide insight into stellar nucleosynthesis [132,133].

Experimentally, the effect has predominantly been studied by beam-foil spectroscopy of He-like ions (for a very recent and comprehensive review see [134]) where the hyperfine-induced (HFI) transition of the metastable $1s\,2s\ ^3P_0$ level to the $1s^2\ ^1S_0$ ground level competes with the much faster transition to the $1s\,2s\ ^3S_1$ first excited level (Fig. 6). The situation is much more clear-cut for Be-like ions, and, in general, divalent atoms and ions, having a $(ns)^2\ ^1S_0$ ground level and a valence shell n, where the $ns\,np\ ^3P_0$ level is the first excited level which in isotopes with nuclear spin $I = 0$ cannot decay by a one-photon transition. For $I \neq 0$ the hyperfine interaction mixes states with different J and the $ns\,np\ ^3P_0$ level acquires a finite radiative lifetime ($\tau_{\rm HFI}$), which depends strongly on nuclear charge and nuclear magnetic moment.

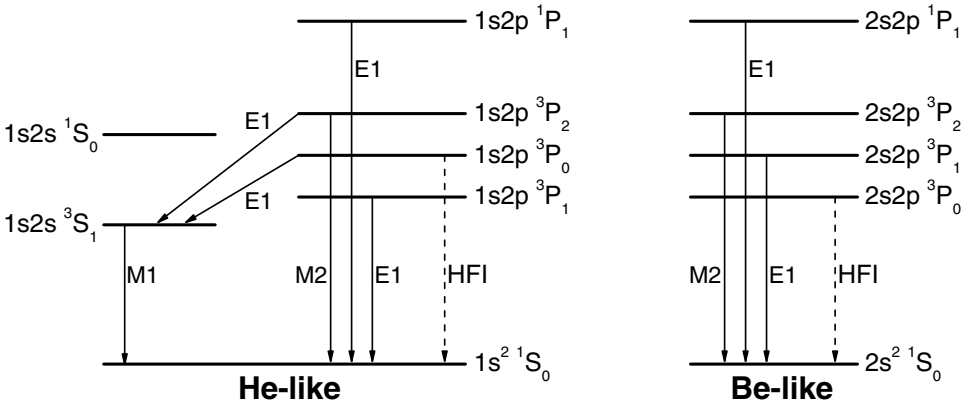

Fig. 6. Schematic of the lowest energy levels and their main one-photon decay modes in He-like and Be-like ions. The energies are not to scale. In the absence of a nuclear spin the hyperfine-induced (HFI) one-photon transitions are forbidden. The lifetimes of the two photon E1M1 processes which compete with the marked HFI transitions are orders of magnitude longer [136] than τ_{HFI}. Therefore, two-photon processes can safely be neglected in the present context.

Theoretical predictions [135] for Be-like ions range from $\tau_{\mathrm{HFI}} \approx 3000\,\mathrm{s}$ for $^{15}\mathrm{N}^{3+}$ down to $\tau_{\mathrm{HFI}} \approx 4\,\mu\mathrm{s}$ for $^{231}\mathrm{Pa}^{87+}$.

Such long lifetimes are attractive in view of obtaining ultraprecise optical frequency standards [137,138]. This has motivated experiments with trapped In^+ [139] and Al^+ [140] ions which provided experimental values for τ_{HFI} (with uncertainties of $\sim 4\%$ and $\sim 7\%$, respectively) from optical spectroscopy of the atomic-clock transitions $5s5p\ ^3P_0 \rightarrow 5s^2\ ^1S_0$ in $^{115}\mathrm{In}^+$ and $3s3p\ ^3P_0 \rightarrow 3s^2\ ^1S_0$ in $^{27}\mathrm{Al}^+$. For Be-like $^{14}\mathrm{N}^{3+}$ τ_{HFI} was inferred from a spectroscopic observation of a planetary nebula [141].

Another experimental environment that permits access to long atomic lifetimes is a heavy-ion storage ring [142]. In fact, the only other experimental value for a HFI lifetime of a Be-like ion, i.e., of $^{47}\mathrm{Ti}^{18+}$, was obtained from a measurement at TSR [143]. In this experiment, Ti^{18+} ions from the MPIK accelerator facility were injected into the storage ring. The decrease of the number of stored ions was monitored by counting Ti^{17+} ions which were produced from the primary beam by electron-ion recombination in an electron beam that moved collinearly with the ion beam in one of the straight sections of TSR. Separation of Ti^{17+} product ions from the Ti^{18+} primary ions took place in the first TSR dipole bending magnet behind the electron target and a single particle detector was positioned at a suitable location behind that magnet such that it intercepted the path of the Ti^{17+} product ions. Since the ions moved at 10% of the speed of light all reaction products were emitted into a narrow cone in the laboratory system and could be detected with essentially 100% efficiency. This is a decisive advantage of the recombination method over, e.g., the more conventional detection of fluorescence photons which suffers from small solid angles and background photons [144].

The TSR experiment yielded $\tau_{\mathrm{HFI}} = 1.8 \pm 0.1\,\mathrm{s}$ [143] which is about 20% larger than the results of the most recent atomic-structure calculations [135,145,146]. This discrepancy is larger than the 5% experimental uncertainty and presently not understood. Somewhat smaller but still significant discrepancies exist between the above discussed trap measurements with In^+ [139] and Al^+ [140] and the corresponding state-of-the-art calculations [147–149]. Clearly, more work needs to be done to reach

a thorough understanding of the intricate hyperfine interaction between electron shell and atomic nucleus.

TSR at HIE-ISOLDE adds a new dimension to this field of research, i.e., the possibility to vary the nuclear magnetic moment of the stored ions by choosing different (radioactive) isotopes of the same element. For example, eight potassium isotopes with sufficiently long nuclear lifetimes of more than seven minutes would become available for HFI lifetime measurements with their nuclear magnetic moments spanning nearly an order of magnitude [150]. Correspondingly, the HFI lifetimes span two orders of magnitude since τ_{HFI} for alkaline-earth-like ions scales with μ_I^{-2} [132]. Therefore, for a number of elements it becomes possible to *chose* an isotope with a HFI lifetime that is shorter than the ion-beam storage time in TSR. TSR at HIE-ISOLDE, thus, considerably enlarges the number of elements in the periodic table for which HFI lifetime measurements can be carried out. Moreover, by comparing measured HFI lifetimes with results from state-of-the-art calculations it may become possible to reduce the present 1%–10% uncertainties of the nuclear magnetic moments of some long-lived isotopes [150]. It should be noted that the main source of the 5% experimental uncertainty in the $^{47}Ti^{18+}$ experiment [143] was counting statistics which possibly can be improved in future measurements.

2.11 Dielectronic recombination on exotic nuclei

The resonant process of dielectronic recombination (DR) is a unique spectroscopic tool that is well-established in the research programmes at CRYRING, TSR and ESR [151–153]. Sharp resonant structures in the recombination cross section that result from the resonant pick-up of free electrons by the highly-charged ion in the so-called dielectronic capture, DC (time-inverse of autoionization), are successfully utilized for high-resolution precision studies of the atomic shell. The DR approach is complementary to conventional methods of spectroscopy that determine the energy of emitted photons. DR collision spectroscopy can be regarded as "inverse Auger electron spectroscopy": Electrons with a given kinetic energy that matches the resonance condition of DR are captured with a higher probability and lead to an increased number of recombined ions. In a storage ring the reaction products are separated from the revolving primary beam in the successive bending magnet behind the electron target and can be registered using particle counters with an efficiency close to one. The high sensitivity that results from large resonant atomic cross sections and the high detection efficiency allows for experiments with minute numbers of stored ions ($\sim 10^4$) and is thus ideally placed for the reduced intensities that are typically available for radioisotopes. The range of applications that have been studied spans from precision studies of QED in strong fields over benchmarks of relativistic atomic theories but also comprises the measurement of absolute cross sections for applications in astrophysics and plasma physics [152].

The installation of a storage ring facility at ISOLDE is very appealing, since the high spectroscopic precision and sensitivity can be exploited to deduce nuclear parameters of stable as well as of unstable isotopes. Radioisotopes with lifetimes down to a few seconds can be accessed provided the time is sufficient to store and cool the ion beam. The electronic structure reflects the mutual interplay of the atomic shell with the nuclear moments. Using the DR technique, one decisively benefits from the well-selected electronic configurations that can be tailored to the scientific needs of the experiment. In particular, Li-like ions and with some restrictions Na-like ions provide ideal probes for the measurement of nuclear properties such as charge radii, magnetic moments and nuclear spins. Ions with a single $2s-$ or $3s-$ valence electron posses a large overlap with the nucleus, thus, showing substantial isotope shifts and

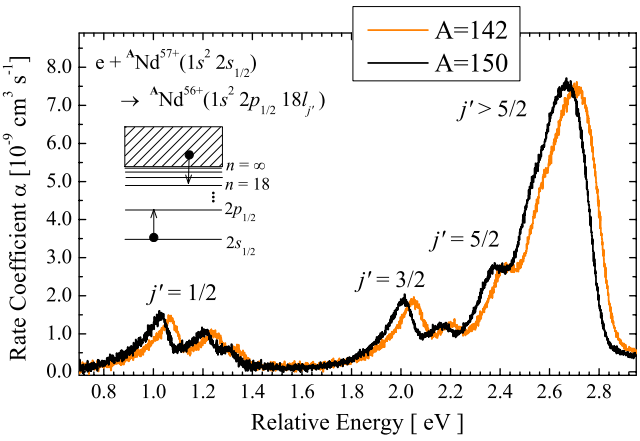

Fig. 7. Experimental DR spectra of the two Li-like neodymium isotopes $^{A}Nd^{57+}$ with A=142 (orange) and A=150 (black) in the energy range of the $^{A}Nd^{56+}(1s^2 2p_{1/2} 18l_{j'})$ resonance group [155]. The experiment was conducted at the ESR storage ring using the electron cooler as a target for free electrons.

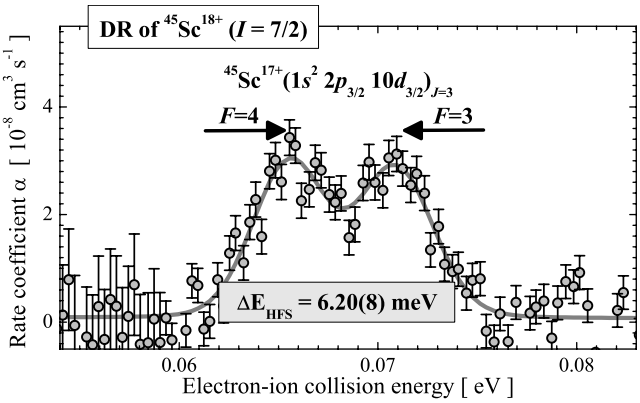

Fig. 8. Hyperfine-split DR resonances of $^{45}Sc^{18+}$ ($I = 7/2$, $\mu_I = 4.7565$) [157] of $(1s^2\, 2p_{3/2} 10d_{3/2})_{J=3}$ doubly excited states. The separation of the resonance states that are just 6 meV apart could be achieved exploiting the unique capabilities of the TSR high-resolution electron target. Please note, that the two F-states are about equally populated.

hyperfine effects. At the same time the interpretation of the experimental data is clear-cut and without ambiguity since the analysis can be performed within a full QED framework [154–156]. Due to the strong scaling of nuclear size and hyperfine effects with $Z^{5\ldots6}$ and Z^4, respectively, the DR approach is especially well-suited for heavier ions ($Z > 40$).

First experiments that revealed isotope effects in DR were reported from CRYRING [158] and TSR [159] for ions with Cu-like and Zn-like electronic configurations, i.e., with active 4s-electrons. A major progress was achieved by the transition to ions with just three valence electrons. The application of DR of such Li-like ions to nuclear ground state properties was pioneered at the ESR and TSR. Figs. 7 and 8 show two remarkable examples of an isotope shift experiment with stable three-electron Nd ions ($^{A}Nd^{57+}$, A = 142, 150) [155] and a hyperfine splitting study of $^{45}Sc^{18+}$ [157], respectively, in order to visualize the potential of the technique. The latter experiment was carried out at the ultra-cold target station of the TSR storage

ring and benefitted from its unprecedented experimental performance. The extension to unstable isotopes was demonstrated at the ESR: DR spectra of uranium and protactinium radionuclides produced in-flight have been measured for the first time [160,161]. Recently, the feasibility to extend the scope of the experiments also to nuclear isomers was realized in a test-run [162].

In addition to the static nuclear structure studies, the long storage time that is routinely achieved at heavy ion storage rings can be combined with the "DR tool" in order to measure the lifetimes of long-lived atomic or nuclear excited states. Metastable beam admixtures exhibit unique fingerprints in the DR resonance spectra well-distinguishable from the ones of the ground state. Thus, the intensity of resonance features that are attributed to the excited state can be used to monitor the additional beam component, and hence, rendering lifetime studies possible. The technique has been used to study atomic metastable states [163,164] and the hyperfine quenching thereof [143]. Similarly, the lifetime of excited hyperfine levels and the one of nuclear isomers can be experimentally accessed. The latter option is very attractive since isomeric lifetimes can be measured in dependence on a well-controlled degree of ionization, i.e., with partial or full suppression of internal conversion or nuclear electron capture. It is worth emphasizing, that DR technique does not rely on the energy separation of nuclear ground and isomeric state but rather on their different hyperfine structure and charge radii. Consequently, with this approach also isomers with excitation energies that are too small to be resolved by revolution frequency (Schottky spectrometry, see e.g. Refs. [165–167]) can be addressed.

With DR, a broad scientific program can be pursued at ISOLDE:

- isotopic or/and isotonic shifts and hyperfine splitting can be measured thus providing information on nuclear charge radii, magnetic moments and nuclear spins. As it was outline before, due to the reliable theoretical description and the practical absence of many-body effects, the DR approach with its simple electron configurations is complementary to the existing optical/laser techniques. For heavy ions, in a combined analysis, DR can be used to calibrate the laser data, e.g. with respect to the determination of the electron density at the site of nucleus or the elimination of many body or mass effects. DR spectroscopy can also be applied to elements where no suitable laser transition is at hand.
- DR as a detector, can serve in support of laser experiments of heavy highly charged ions in the storage ring that, e.g. for experiments that directly drive the transition between hyperfine states [128,168]. The task of DR in such a scenario is to provide the alternative to fluorescence detection.
- Owing to the resonant charge-changing character, DR can be exploited for beam purification, in principle. Experiments with such purified beams may be suitable for studies on laser interaction with the nuclei or for the search of predicted Nuclear Excitation by Electron Capture (NEEC) phenomenon [111] either in-ring or extracted to an external target station.
- One extremely important physics goal is the investigation of the lowest known isomeric states (^{229}Th (E^*=7.6 eV, $T_{1/2}$=79 h [169]), ^{235}U (E^*=76.5 eV, $T_{1/2}$=26 min [8])). This comprises radii, moments or lifetime studies but also the search for new, but yet unknown candidates such as states in ^{233}Th or ^{231}U [8].

The TSR features a twin electron-beam set-up comprising of an electron cooler and a dedicated electron target [153,170,171]. This "ultra-cold" electron target is optimized with respect to optimal spectroscopic performance, that is, an electron beam as monoenergetic as possible. The existing target is operated without the intermittent cooling tasks that have to be applied within a stand-alone electron cooler experiment. The co-operating cooler plus target arrangement is by orders of magnitude superior in versatility, duty cycle, precision and resolution to a single electron device (cf. Fig. 9).

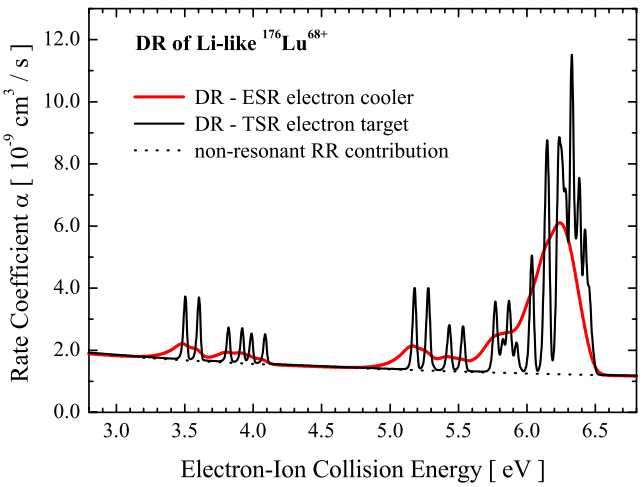

Fig. 9. Performance of the TSR high-resolution electron target: simulation of the DR spectra of Li-like $^{176}Lu^{68+}$. The red line corresponds to experimental conditions typically for the electron cooler of the storage ring ESR at GSI and the black to the parameters of the TSR high-resolution electron target (black line). The dotted line depicts the non-resonant contribution from radiative recombination.

Thus, the cooler/target combination is an indispensable asset and mandatory with respect to the envisaged DR experiments at ISOLDE. The availability of radioisotopes together with the TSR electron collision facilities will open up new and fascinating opportunities.

In order to have distinctive long beam lifetimes of very highly charged heavy ions in the storage ring it would be beneficial to have a high injection energy and/or make use of the TSR's capability to serve as a synchrotron. DR experiments can then be run at an ion energy that corresponds to the maximum magnetic rigidity of the ring. Thus, cooler and target are required to operate stable up to this maximum design energy. Since few-electron ions are essential, an upgrade of the REXEBIS is required. The experiments can be conducted if the beam intensity reaches 10^4 stored ions, which should be achievable with present EBIS technologies and/or stacking capabilities of the TSR.

2.12 Atomic data for modeling supernova explosions

Supernovae and their progenitors are responsible for the production of the majority of elements from carbon and heavier [172,173]. The relevant nucleosynthesis models can be tested using X-ray spectral observations of supernova remnants (SNRs) and measuring elemental abundances from the line emission of the various ions produced (e.g., [174]). Also of interest is the distribution of elements within a SNR [175,176]. These can be used to constrain the processes occurring inside the star during the explosion such as the interaction between the various burning shells [177], convective instabilities [178,179], and instabilities at the accretion shock [180,181]. All of these are thought to create asymmetries which may hold the key to understanding the core-collapse supernova explosion mechanism [182,183]. SNRs themselves may be analyzed (taking into account atomic physics, non-equilibrium ionization, radiative cooling, and hydrodynamics) to place constraints on the explosion as well as ejecta mass and composition (e.g., [184–187]). However, these constraints are only as good as the underlying atomic data in the models.

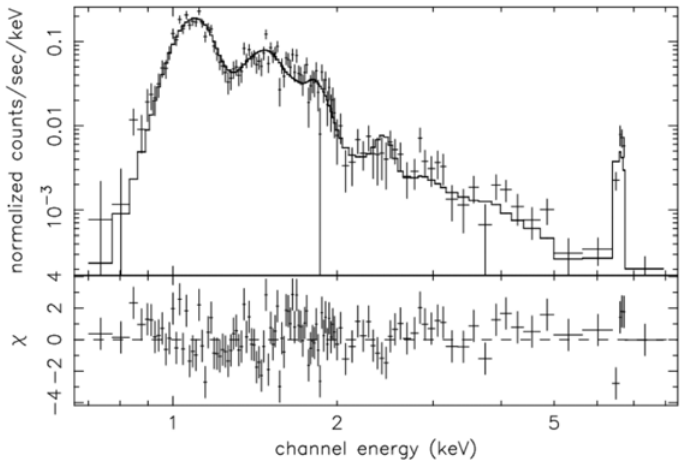

Fig. 10. *Chandra* spectrum from an iron-rich knot in the SNR Cas A (adapted from [184], courtesy of U. Hwang and J.M. Laming). This spectrum has been background subtracted using a region from another portion of the SNR. Only Si and Fe are required in order to fit this spectrum using an NEI model. The resulting values of $n_e t$ are (0.2–1.2) $\times 10^{11}\,\mathrm{cm}^{-3}\,\mathrm{s}$ for Si and (2.7–5.5) $\times 10^{11}\,\mathrm{cm}^{-3}\,\mathrm{s}$ for Fe. An abundance ratio of $\mathrm{Fe/Si} = 12(\mathrm{Fe/Si})_\odot$ has been inferred. The Fe-L and Fe-K emission can be seen around 1.0–1.7 keV and 6.7 keV, respectively. The Si-K emission is between 1.8 and 2.0 keV.

The charge state distribution at the high electron temperatures T_e found in SNRs is driven by electron impact ionization (EII). The dominant electron-ion recombination process is high T_e dielectronic recombination (DR), but the gas has had insufficient time to come into ionization equilibrium. Under these non-equilibrium ionization (NEI) conditions, the ionization evolution of the plasma depends on the ionization-age parameter $n_e t$, where n_e is the electron density and t is the time that has passed since the non-equilibrium conditions were created (e.g., by abrupt heating due to hydrodynamical shocks). Diagnostics of the ionization age combined with an independent measurement of the electron density can provide valuable information about the age and other properties of the observed source.

Figure 10 shows the *Chandra* spectrum from an iron-rich knot in the SNR Cas A [184]. The spectrum has been background subtracted using a region from another portion of the remnant. Only Si and Fe are required in order to fit this spectrum using an NEI model. The resulting values of $n_e t$ are (0.2–1.2) $\times 10^{11}\,\mathrm{cm}^{-3}\,\mathrm{s}$ for Si and $(2.7 - 5.5) \times 10^{11}\,\mathrm{cm}^{-3}\,\mathrm{s}$ for Fe. An abundance ratio of $\mathrm{Fe/Si} = 12(\mathrm{Fe/Si})_\odot$ has been inferred. The different values of $n_e t$ suggest that the Si emission and Fe emission are not co-spatial. If this is true, then this may be the signature of a special type of explosive silicon burning called α-rich freeze out. What is special about this type of burning is that it produces ^{44}Ti which has been observed in Cas A [188,189]. This may be the result of an asymmetric explosion [190]. However, a systematic overestimate (underestimate) in the recommended EII rate coefficients for Si(Fe) would lead to an underestimate (overestimate) in the inferred value of $n_e t$. Thus it will not be definitive that the Si and Fe emission are not co-spatial until reliable EII data exist for the relevant ions.

More recently the Cas A SNR was observed by the *Chandra X-ray Observatory* for a total of 1 Ms [186,187]. This is a factor of 20 increase over previous *Chandra* observations, and is by a long way the deepest ever X-ray observation of a SNR. The ultimate goal of this observation is a 3D reconstruction of the ejecta structure and

composition, with the aim of diagnosing the explosion mechanism(s). The departures from ionization equilibrium observed in the X-ray emitting knots will establish ejecta Lagrange mass coordinates, for eventual comparison with the predictions of explosion models. These data are of such quality that uncertainties in the atomic physics used to model them have become a source of concern.

Critical to the interpretation of NEI plasmas is reliable EII data. High T_e DR is believed to be well understood theoretically, in part due to an extensive series of DR measurements performed by us at TSR [191,192]. EII is less well understood, as our work at TSR has shown [193,194]. Theoretical calculations are largely untested against reliable experimetal work. Previous laboratory studies were usually performed using beams with unknown metastable populations. This limits their utility for benchmarking theory. TSR overcomes this issue by storing the ions long enough for metastable levels to radiatively relax, thereby generating a ground state beam of ions for EII studies and unambiguous benchmarking of theory. TSR is currently the only facility in the world capable of performing EII measurements on pure ground state beams for ions with complex valence shells. Thus TSR offers a unique opportunity to deepen our understanding of supernovae, through EII measurements on various ions of Si and Fe.

2.13 Atomic data for fusion energy research

Most of the remaining challenges in developing electrical power plants based on magnetically confined nuclear fusion are related to finding appropriate materials for the plasma facing components of the reactor [195]. One of the materials that will be used in the International Thermonuclear Experimental Reactor (ITER) is tungsten [196]. Consequently, tungsten ions are expected to be prominent impurities in the fusion plasma. Radiation from excited tungsten ions leads to substantial plasma cooling which has to be well controlled in order to maintain the conditions for nuclear fusion. Thus, a comprehensive knowledge of atomic energy levels and collision cross sections is required for a thorough understanding of the spatial and temporal evolution of the tungsten charge states and emission spectra in fusion plasmas [197].

To date, only a small fraction of the needed atomic data has been derived from experimental measurements and most comes from theory [198]. For many relevant charge states with electron configurations involving open atomic d or f shells, theoretical calculations are extremely challenged by the extraordinary complexity of the atomic structure. The situation is particularly problematic for dielectronic recombination (DR) where results from state-of-the-art quantum mechanical calculations were obtained for only very few tungsten ions [199]. For the time being, fusion plasma modeling has therefore to rely on DR rate coefficients which are based on the semi-empirical Burgess formula [200] and which are available from the ADAS data base [201].

This situation has stimulated storage-ring measurements of *absolute* DR rate coefficients of tungsten ions. Figure 11(a) displays the recently published [202] first storage-ring result for any tungsten ion, i.e., for $W^{20+}(4d^{10}4f^8)$. Most dramatically, at energies of at least up to 30 eV it is characterized by a high level about three orders of magnitude above the rate coefficient for non-resonant radiative recombination (RR). The huge DR resonances at very low electron-ion collision energies strongly influence the plasma rate coefficient even at temperatures above 100 eV as can be seen from Fig. 11(b). At all plasma temperatures the experimentally derived rate coefficient is very significantly larger than the W^{20+} DR rate coefficient from the ADAS data base [201]. This difference amounts to a factor of 4.3 at a plasma temperature of 160 eV where the fractional abundance of W^{20+} is predicted to peak in a fusion

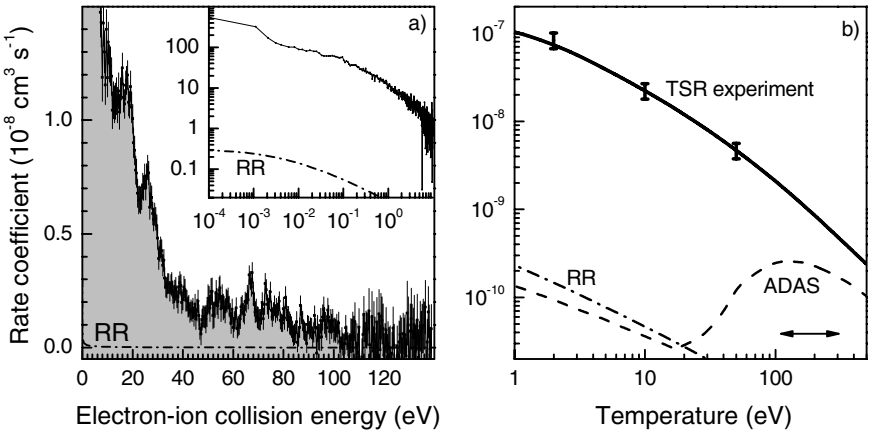

Fig. 11. Dielectronic recombination of W^{20+} [202]: a) Measured merged-beams rate coefficient for electron-ion recombination of W^{20+} as a function of relative collision energy. The dash-dotted curve is the calculated merged-beams rate coefficient for radiative recombination (RR) using a hydrogenic approximation. The inset shows the same data in a log-log representation emphasizing the rate coefficient at very low energies. b) Rate coefficients for the recombination of W^{20+} in a plasma. The thick full curve is the experimental result which has been derived by essentially convoluting the measured result from panel a) with an isotropic Maxwellian energy distribution. Error bars denote the 20% experimental systematic uncertainty. The dashed curve is the DR+RR rate coefficient from the ADAS data base and the dash-dotted curve is again the result of the hydrogenic calculation for the RR rate coefficient. The horizontal arrow indicates the temperature range where W^{20+} is expected to form in a fusion plasma.

plasma. Similar or even larger discrepancies are expected for other charge states of tungsten.

With the present configuration of MPIK accelerators, tungsten ions with charge states of about up to 30+ can be supplied in sufficient quantities for DR experiments. TSR at HIE-ISOLDE will allow one to considerably extend the range of charge states up to about 50+ with the currently available charge breeder (REXEBIS) and possibly up to 72^+ (He-like) with an upgraded charge breeder. Measurements of *absolute* rate coefficients for DR and, equally important, for electron-ion impact ionization will thus become possible for all the charge states of tungsten which are relevant for fusion plasma modeling [197].

2.14 R&D for beta beams: Tests with stable and radioactive ions

Beta beams are today one of the possible long baseline facilities to explore neutrino properties, primarily neutrino oscillation physics including CP violation in the leptonic sector. The TSR at ISOLDE can be used as a versatile tool to investigate different aspects useful to the beta beams. This is possible because of the large variety of the available stable and radioactive ions delivered by REX-ISOLDE at energies of 1 to 10 MeV/u, which will be used as an injector to the TSR. In the beta beam concept, the (anti-)neutrinos are produced by acceleration and final storage of beta-decaying isotopes with decay times around one second. CERN is a possible place to produce these well collimated pure neutrino or antineutrino beams since a suitable accelerator complex is available including the expertise to produce the needed radioactive

isotopes. In the following we give a list of non-exhaustive topics of investigation:

(i) *Production and storage of* $^{6}He/^{18}Ne$ *or* $^{8}Li/^{8}B$ *ions*
A milestone in the production of suitable intensities of ^{6}He has already been achieved at ISOLDE. The production of 10^{11} $^{6}He^{+}$ ions/s is possible at HIE-ISOLDE, and, provided cw injection into REXEBIS from ISCOOL becomes available with improved efficiencies, intensities of about $5 \cdot 10^{9}$ ^{6}He ions stored in the TSR can be envisaged. The investigation of different parameters such as ion injection, cooling linked with decay losses will be very valuable for the benchmarking of the numerical simulation tools used in the beta beam study. This will be extended to other candidates such as ^{18}Ne or ^{8}Li/^{8}B ions. In the latter case, ^{8}B beams are not yet available at ISOLDE and should be developed.

(ii) *Production of* $^{8}Li/^{8}B$ *ions with stored* ^{7}Li *ions*
The concept of a production ring for ^{8}Li/^{8}B based on stored ^{7}Li and ionization cooling has been proposed by C. Rubbia *et al.* While no study has yet been undertaken to see if the TSR would be suitable to test this concept, both the framework of HIE-ISOLDE and the availability of stable ions from the Linac during off-line beam time are strong motivations to explore this possibility. In that case, the production of $5 \cdot 10^{8}$ ^{7}Li ions/s from REXEBIS has already been demonstrated. This can be used for a reduced scale feasibility study. Several orders of magnitude should be gained if a full scale experiment is envisaged.

(iii) *Physics with low-energy neutrinos*
The availability of stored high intensity beta-decaying ions offers the possibility to perform experiments with detector(s) close to the neutrino source. This is one of the possible realizations of the low energy beta-beam proposed by C. Volpe [203]. Experiments with this kind of source might cover searches for physics beyond the Standard Model, e.g. measurement of the neutrino magnetic moment, or of coherent neutrino-nucleus scattering or the search for sterile neutrinos [204], as well as measurements of interest for nuclear and core-collapse supernova physics (see Ref. [205] for a review). These searches would benefit from reaching high intensities of high Q-value ions.

3 The injector

The post acceleration of the radioactive ions produced at ISOLDE is done at REX-ISOLDE [206]. The mass-separated, low-energy ions from ISOLDE are presently accelerated to energies up to 3 MeV/u in the pulsed REX-ISOLDE linac, which consists of 6 normal conducting (NC) cavities. An energy upgrade is foreseen within the HIE-ISOLDE [207] framework with beam energies of 5.5 MeV/u available in 2014, and 10 MeV/u in 2017. The higher beam energies are attained by superconducting cavities (SC), the so called HIE-ISOLDE linac [208], replacing part of the room-temperature cavities. As a link between ISOLDE and the linac a bunching and charge breeding system is positioned. This key element increases the charge state of the exotic ions before they are injected into the compact linear accelerator.

3.1 Charge breeding performance and requirements

3.1.1 The REXEBIS breeder

The bunching and charge breeding system of REX-ISOLDE consists of a Penning trap that accumulates, cools and bunches the semi-continuous beam from ISOLDE, followed by an Electron Beam Ion Source (EBIS) acting as charge breeder that increases

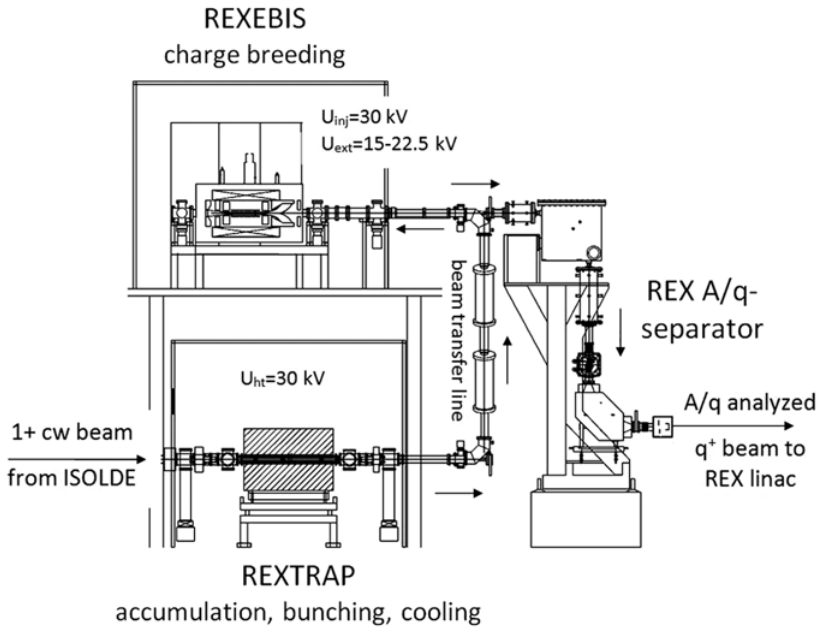

Fig. 12. Layout of the REX-ISOLDE low-energy part, including Penning trap, transfer line, breeder and A/q-separator.

the ion charge from 1+ to $q+$ [54]. The layout of the low-energy part is illustrated in Fig. 12.

The system is capable of charge breeding ions over the full mass spectrum with an efficiency of at least a few percent as demonstrated in Fig. 13 (top). REXEBIS is designed for production of ions with a moderate charge such that the mass-to-charge ratio, A/q, is less than 4.5, the restriction given by the A/q-limit of the REX linear accelerator. Fully stripped ions or few-electron systems have not been considered. In Fig. 13 (middle) the breeding times for different ion masses are plotted and in Fig. 13 (bottom) the corresponding A/q-values are indicated. With extended breeding times the A/q-values can be lowered and ultimately become limited by the electron beam energy and the radiative recombination (RR) rate. Charge states with ionization energies higher than the electron beam energy (approximately 5500 eV) cannot be reached. In REXEBIS it has been proven that fully stripped ions up to Z=18 can be produced, but with a charge breeding efficiency limited to maximum 1% and with a breeding time approaching 1 s. The system is predicted to produce H-like atoms up to $Z = 20$ and He-like ions to $Z \approx 38$, also with a reduced efficiency and extended breeding time compared to Fig. 13 (top) and (middle). An approximate upper limit for the attainable q as a function of proton number Z (above 20) is plotted in Fig. 14.

When the electron beam energy is higher than the ionization potentials of the charge states being charge bred, the ionization factor $j_e \cdot T$, i.e. the product of the electron current density j_e and the breeding time T expressed in $\mathrm{A \cdot s/cm^2}$, determines the obtainable charge state. In other words, the time required to reach a certain charge state depends on the electron-impact ionization cross-sections and the electron beam current density. In addition, RR and charge exchange processes, discussed below, will affect the ionization time. The ionization cross-sections are energy dependent and reach a maximum value for an electron beam energy of about 2.7 times the ionization energy from one charge state to the next. The electron beam current in REXEBIS is typically <300 mA, with an electron current density j_e<150 $\mathrm{A/cm^2}$. Hence, after

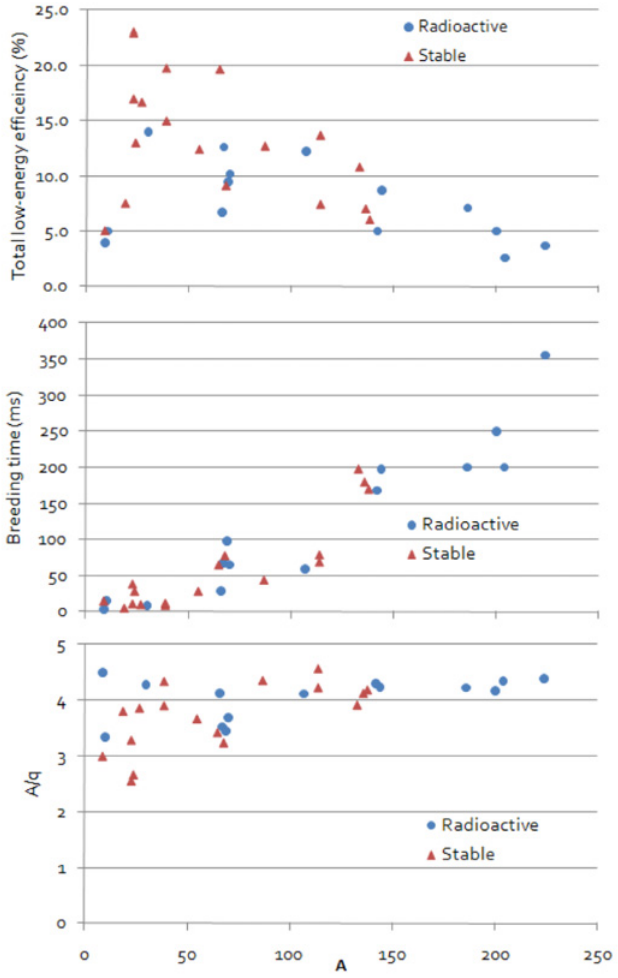

Fig. 13. Top: measured total low-energy efficiency (trap + EBIS + REX mass separator) for a selection of elements. Middle: charge breeding time for the same elements (excluding cooling-bunching time inside REXTRAP, which is normally the same length as the breeding time). Bottom: mass-to-charge ratio for the same elements.

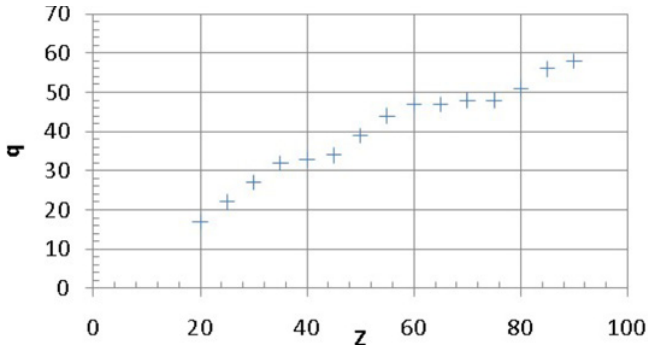

Fig. 14. Estimated attainable charge states in REXEBIS as a function of ion Z.

Table 3. Estimated REXEBIS breeding times for a selection of nuclides of relevance for experiments with TSR at HIE-ISOLDE.

Ion	Z	q	A/q	Breeding time (ms)
^{7}Be	4	3	2.33	10
^{18}F	9	9	2	100
^{70}Ni	30	25	2.8	350
^{132}Sn	50	30	4.4	120
^{132}Sn	50	39	3.38	700
^{132}Sn	50	45	2.93	EBIS upgrade needed
^{186}Pb	82	46	4.04	250
^{186}Pb	82	53	3.51	1000
^{186}Pb	82	64	2.90	EBIS upgrade needed

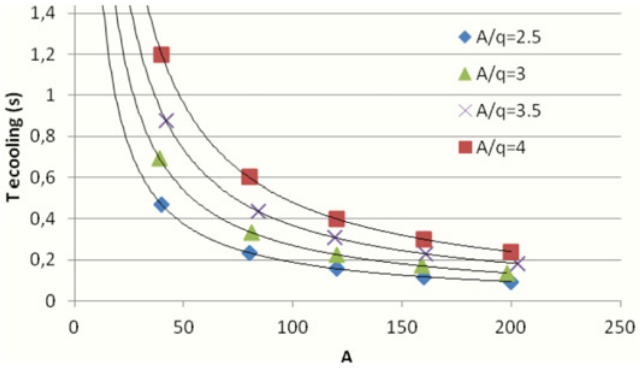

Fig. 15. Calculated electron cooling times in TSR as a function of ion mass for different A/q-values.

a charge breeding of 1 s inside REXEBIS an ionization factor of <150 A $\cdot$ s/cm^2 is reached.

In Table 3 the REXEBIS breeding times for a selection of elements and charge states of relevance for TSR at ISOLDE are listed. Several of the elements have relatively high charge as this leads to shorter electron cooling times. Some of the selected charge states are not within reach for REXEBIS due to the limited electron beam energy, so in the case they are required an upgraded REXEBIS is necessary. Upgrade suggestions are described in Sect. 3.1.5.

The accumulation and phase-space cooling of the semi-continuously released ions from the ISOLDE target takes place inside the buffer-gas filled REXTRAP. The ions are kept inside REXTRAP for as long time as the breeding process in the EBIS takes. They are thereafter transferred in a bunch and injected into the breeder. As seen in Fig. 13, light elements are charge bred within a few ms, while heavier requires a few hundred ms. Thus, the repetition rate for REX-ISOLDE in normal operation mode varies between 50 and 2.5 Hz. Such high repetition rates are not compatible with ECOOL stacking into TSR (see Sect. 4.6.2), nor if the TSR experiment requires electron-cooled beams. The reason is the long electron cooling time, described in Eq. (13) and illustrated in Fig. 15 as a function of the ion mass for different A/q. We see that low A/q-values and heavy elements have shorter cooling times. As explained above and illustrated in Table 3, low A/q-values stipulate long breeding times and

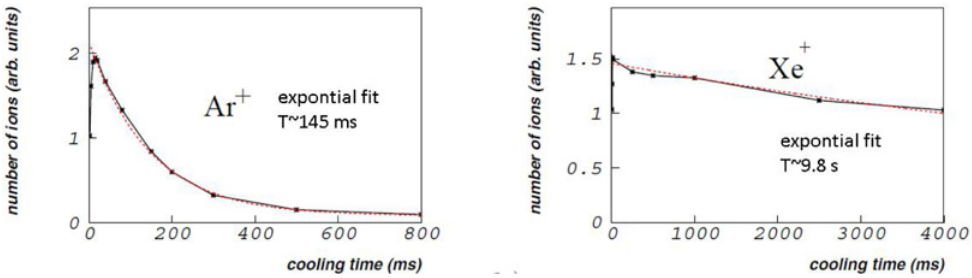

Fig. 16. Number of extracted Ar^+ and Xe^+ from REXTRAP as a function of storage time. Cyclotron cooling was applied.

a lower repetition rate of REX-ISOLDE, which matches the operation of TSR well. Moreover, the period time can be increased further by keeping the ions for longer in the trap before passing them on to the EBIS. Although the hold-up time in REXTRAP is normally the same as the breeding time, one can in principle store the ions in REXTRAP for longer times than the breeding time. Trapping times exceeding 1.5 s with additional ion losses less than 20% have been demonstrated for Ni and Rb. On the other hand, noble gases cannot be stored in REXTRAP without losses due to charge-exchange processes with the Ne buffer gas, see Fig. 16 [209]. The holding times for other elements with a high ionization potential, such as F, Cl, Br etc, as well as light elements ($A < 20$), have to be investigated. Finally, it should be pointed out that a long accumulation time may lead to space charge effects inside REXTRAP and with an efficiency loss as result. The tests with Ni and Rb were carried out with approximately $3 \cdot 10^7$ ions/s injected into the Penning trap.

The ion throughput rate is determined by the storage capacity of the electron beam for positive charges and the rate at which the accumulation, breeding, and extraction cycle can be repeated. The ion storage capacity is determined by the trap length L, the electron beam current I_e, the electron beam voltage U_e and the electron beam compensation degree f, and given by the expression:

$$f \cdot I_e \cdot L \sqrt{\frac{m_e}{2e \cdot U_e}},$$

where m_e and e denote the mass and the charge of the electron. For REXEBIS the electron space charge capacity amounts to $4 \cdot 10^{10}$ charges and a compensation degree of 50–70% is commonly attained. With approximately 20% of the beam in the desired charge state, that means $1 \cdot 10^9$ ions with charge $q = 5+$ can be extracted from one pulse, and $1 \cdot 10^8$ ions with charge $q = 50+$. This assumes that no evaporative ion-cooling using lighter ions is required, as the light ions will occupy part of the electron space charge. In reality REXTRAP is the limiting factor for high ion throughputs. The trap can accept around 10^8 ions/pulse with a maintained efficiency for the REX bunching and breeding system. The number of accelerated particles per second is therefore:

$$10^8 \cdot \eta_{\text{trap-EBIS}} / T_{\text{repetition}}, \tag{1}$$

where $\eta_{\text{trap-EBIS}}$ is the combined efficiency for REXTRAP, REXEBIS and REX mass separator for the 1^+ to q^+ transformation process. $T_{\text{repetition}}$ is normally the breeding time, but for the very light elements, where the breeding time is less than 20 ms, a minimum $T_{\text{repetition}}$ of 20 ms has to be adopted to allow for the cooling inside REXTRAP. Using the values from Fig. 13 one finds that the amount of ions injected into the linac decreases from $\sim 2.5 \cdot 10^8$ particles/s for $A < 50$ to $\sim 2.5 \cdot 10^7$ particles/s for $A > 200$ if REX is operated in normal mode. If a long storage time in REXTRAP (for

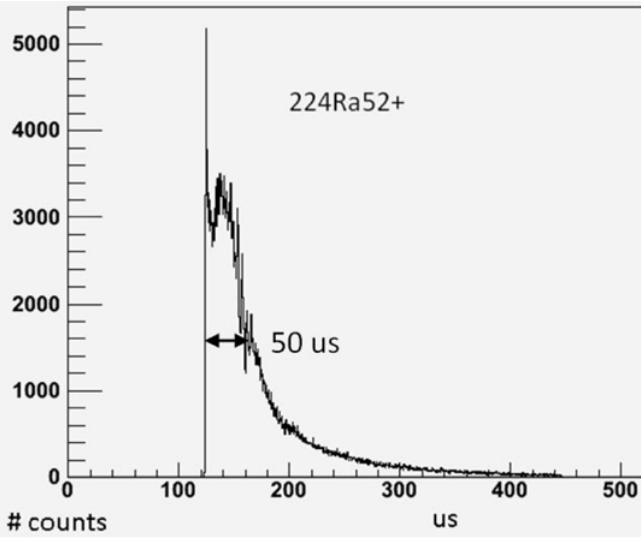

Fig. 17. Pulse structure for beam extracted from REXEBIS in normal extraction mode.

instance 1.5 s) is requested due to the electron cooling time in TSR, the ion throughput will be correspondingly lower ($\sim 3 \cdot 10^6$ ions/s).

The ion-extraction bunch length from REXEBIS, the so-called macro-bunch, has a FWHM length of approximately 50 μs during normal extraction, see Fig. 17. In this mode a 30 V slope is applied to the three trapping tubes constituting the ion trap during extraction. If the trapping region is modified so more tubes are introduced, and a higher voltage gradient is applied during extraction (up to kV), the pulse length could be shortened, possibly down to 10 μs. The extracted beam will then have a larger energy spread, thus the beam transport through the REX mass separator [210], a Nier-type spectrometer, as well as the injection efficiency into the RFQ cavity will be affected. Recent tests have proven that voltage variations of the trapping tubes of at least 350 V can be applied with only 15% transmission losses of the accelerated beam. To minimize the injection losses into the TSR during multi-turn injection, the extraction pulse length at 10 MeV/u injection energy has to be shorter than $\sim$35 μs. If the pulse length is shortened further, the non-cooled horizontal beam size in the ring is reduced.

The continuous beam released from the primary target of ISOLDE is bunched into a few short EBIS pulses. Thus, the instantaneous beam rate at the present experimental setups at REX-ISOLDE is several times higher than the intensity per second from the primary target. A limit on the incoming beam intensity is imposed by the dead time in the particle detector electronics [211]. This can be partly alleviated by increasing the extraction bunch length out of the EBIS using the slow extraction mode. Nevertheless, the bunch length is limited to 850 μs by the RF acceleration window. On the other hand, if the beam is injected into TSR, and not bunched but coasting, a true cw beam structure is obtained. The circulating beam could furthermore be extracted from the ring in a slow mode providing a cw beam to an external experiment connected to the ring.

3.1.2 TSR charge state requirements

The main determining factors for the required ion charge state are the beam rigidity limitation in TSR, the specific experimental requirements, the storage lifetime of the

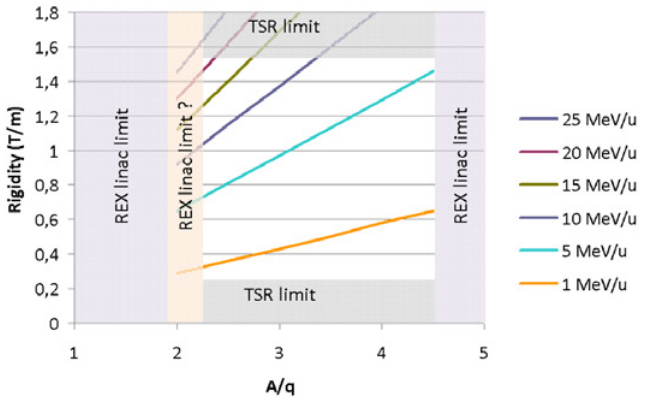

Fig. 18. Achievable beam energies inside TSR and the corresponding A/q and rigidity values.

Table 4. Ionization energies (in eV) for different electronic configurations and for different elements [212].

Z	$I_{Mg->Na-like}$ (eV)	$I_{Be->Li-like}$ (eV)	$I_{He->H-like}$ (eV)	$I_{H-like->bare}$ (eV)
15	x	586	2690	2953
30	754	2596	11440	11980
45	2197	6273	26720	27550
60	4326	11750	49140	50290
75	7288	19390	79850	81360
90	11380	28780	120900	122800

beam and the cooling time in the electron cooler.

– **Rigidity limitations**
In Fig. 18 a plot of the TSR rigidity and REX A/q-limitations is presented. TSR has an upper beam rigidity limit of 1.57 Tm, translating to an A/q-limit of 3.44 for a beam energy of 10 MeV/u. The upper A/q-limit of 4.5 is imposed by the REX linac. Also the lower A/q-limit is given by the REX linac as instabilities in the power supplies and RF jitter will deteriorate the beam quality, and multipactoring effects in the region $2 < A/q < 2.33$ may occur (to be investigated). In addition, the EBIS breeding may restrain the possibility of reaching the lower A/q-values, compare with Fig. 14.
– **Experimental prerequisites**
In the case measurements of atomic effects on half-lives on medium-heavy nuclei are to be performed they require H-like ions (Sect. 2.9). In a similar way studies of capture reactions for the astrophysical p-process demand fully stripped ions (Sect. 2.5). In both cases ions up to $Z \sim 60$ might be requested. The ionization potentials (for $Z = 60$), going from He- to H-like and from H-like to bare ions, are 49 keV and 50 keV, respectively, as listed in Table 4. An electron beam energy of at least 100 keV, preferably above 150 keV, in the EBIS breeder is therefore required to keep the RR low. The RR process counteracts the electron-impact ionization, and becomes stronger when the ionization potential approaches the electron beam energy [213]. Dielectronic recombination, a resonant process, does not contribute at the electron energies used here, and three-body recombination is negligible. Simulations using CBSIM [214], shown in Fig. 19, indicate that a $j_e \cdot T$ in excess of 20 kA·s/cm^2 is required in order to reach these high charge states. For such an ionization factor the charge state distribution will have 30% of the ions in H-like electron configuration and less than 20% as bare ions. Dielectronic recombination

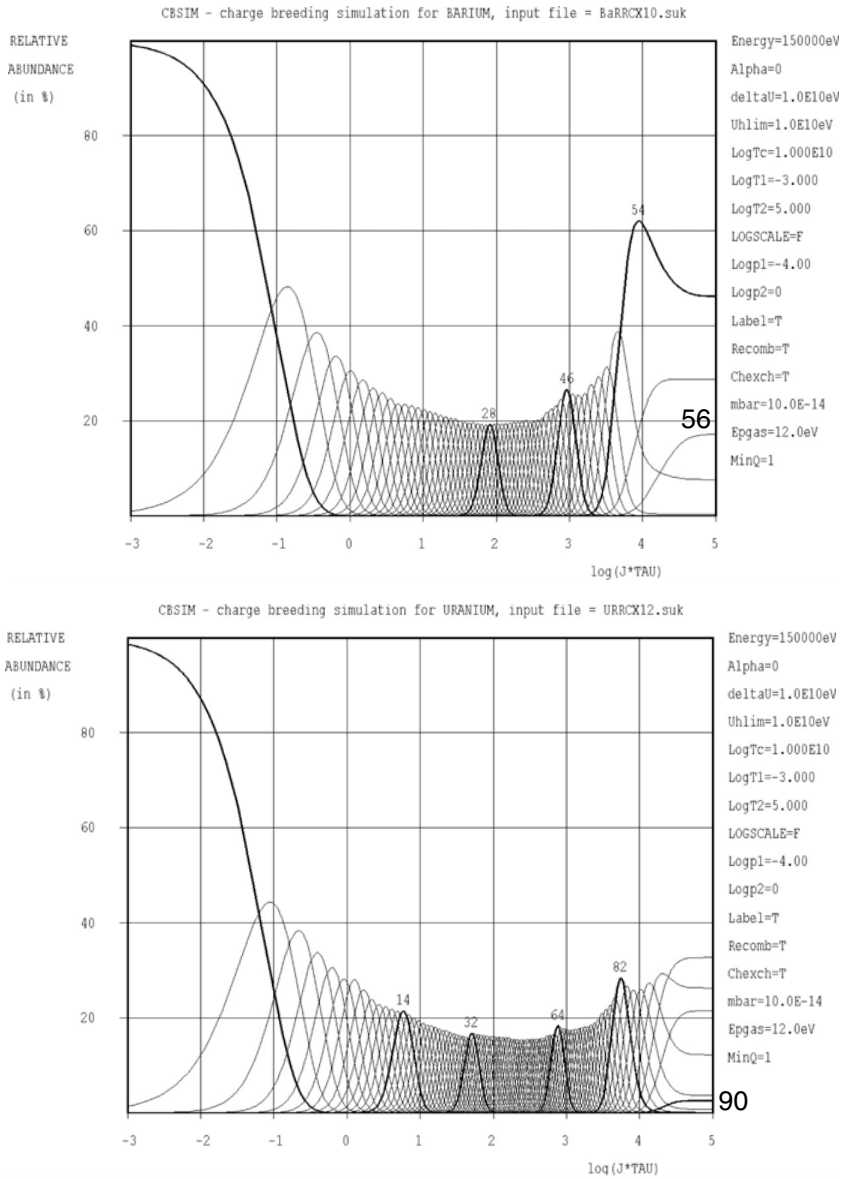

Fig. 19. Charge state development simulations for $Z = 56$ (top) and $Z = 92$ (bottom) for an electron beam energy of 150 keV. RR has been included as well as charge exchange with a residual gas pressure of 10^{-13} mbar and a neutral to 1+ ionization potential of 12 eV. For these parameters the RR in combination with the charge exchange process, governed by the vacuum inside the breeder, sets the limit of the attainable charge states.

measurements on exotic nuclei (Sect. 2.11) require few-electron system, ideally down to Li-like for very heavy ions, such as Th/U. Also here the electron beam energy should be as high as 150 keV and $j_e \cdot T > 20\,\mathrm{kA/cm^2}$ (see Table 4 and Fig. 19). If a Na-like configuration is acceptable for the heavier ions an electron beam energy of 30 keV and $3\,\mathrm{kA/cm^2}$ would be sufficient. The most stringent requirement on the ionization factor is more than two orders of magnitude higher than the one provided by REXEBIS and the electron beam energy a factor 30 higher.

Table 5. Equilibrium charge states for ions with different Z propagating through a gas.

Z	$\langle q \rangle$ for 5 MeV/u	$\langle q \rangle$ for 10 MeV/u
10	9.6	9.9
30	23.3	27.1
50	33.4	40.3
70	41.8	51.6
90	49.0	61.8

- **Storage lifetimes**
  Many of the suggested experiments in TSR have no defined requirements for the ion charge-state but this should be chosen such that the storage life time is maximized. In general the total loss cross-section, being the sum of the electron capture and stripping cross-sections, as single and multiple Coulomb scattering and electron cooler losses are in most cases smaller, is minimized at the equilibrium charge state explained below.
- **Electron cooling time**
  As illustrated in Fig. 15 short cooling times are achieved for low A/q-values, thus the ion charge should be as high as possible.

3.1.3 Stripper foils and equilibrium charge state

The ions circulating in the storage ring will interact with the residual gas atoms and molecules and with the internal gas jet target if present. Due to electron capture and stripping processes the ions will attain an equilibrium charge state in gas, which can be calculated using the Schiwietz and Grande formulae [215]. Table 5 lists the charge states for different ions at 5 and 10 MeV/u. The influence of the gas composition is negligible. The equilibrium charge state in a gas and a foil are similar.

By introducing a carbon stripper foil (thickness of $\sim$150 μg/cm^2) at the end of the linac the charge state of the ions can be increased in certain cases. Thus, a short breeding time can be maintained in the EBIS which delivers a moderate charge state fulfilling the linac requirement of $A/q < 4.5$. The gain is a reduced breeding time compared with direct breeding to the high charge state. This might not be of major importance as it was shown earlier that the repetition rate for TSR is in most cases lower than for REX-ISOLDE if electron cooling is to be used. On the other hand, the breeding efficiency might be poor for very low A/q-values due to losses inside the EBIS. The lower breeding efficiency should be compared with the reduced ion transmission through a stripper foil as only 15–25% of the stripped ions (depending on the Z of the ion, and thus the width of the charge state distribution) end-up in the correct charge state. It should further be noted that fully stripped and few-electron systems cannot be attained for heavy ions at these low beam energies. At a beam energy of 10 MeV/u the stripper foil technique can force at least 10% of the beam into H-like charge state for elements below $Z = 35$. The graph in Fig. 20 shows the equilibrium charge state, calculated using Ref. [215], as a function of the Z of the ion for two different beam energies when penetrating through a carbon foil.

The stripper foils can also be used for beam cleaning suppressing unwanted contaminants in the beam, as already demonstrated at REX-ISOLDE [216]. The method works primarily for lower-Z ions, i.e. up to $Z = 20$ for beam energies of 5–10 MeV/u.

Stripper foil ladders will be placed in front of the switchyard to the first experimental station and at the entrance of the vertical switchyard to the TSR (see layout in Sect. 3.3.1). Sufficiently long distance between the foils and the fast shutting valve protecting the SC linac is a prerequisite to avoid contamination in the case a vacuum incident bursts the foils.

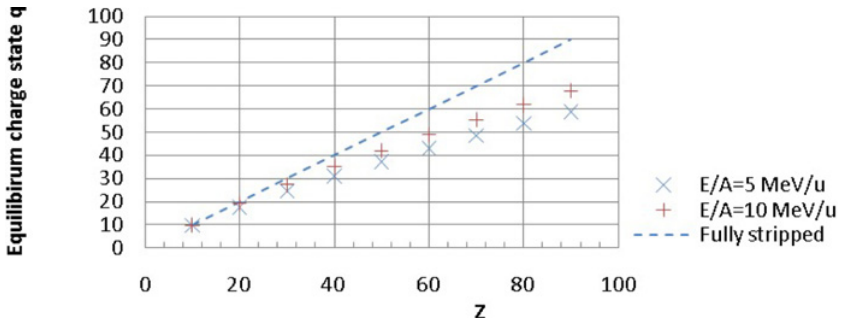

Fig. 20. Equilibrium charge state as a function of Z for ions traversing a carbon foil with 5 and 10 MeV/u.

Table 6. Beam losses in the REX separator due to charge exchange with the residual gases for a pressure of 10^{-8} mbar. The ionization energy of the residual gas atoms was conservatively assumed to be 10 eV.

Charge q	Capture cross section (cm^2)	Electron capture losses%
10	$3.7 \cdot 10^{-14}$	0.8
30	$1.3 \cdot 10^{-13}$	2.5
50	$2.4 \cdot 10^{-13}$	4.5
70	$3.6 \cdot 10^{-13}$	6.7
90	$4.8 \cdot 10^{-13}$	8.9

3.1.4 Vacuum requirements for separator, linac and transfer line

The ions extracted from the breeder are transported through a low-resolution separator to the linac (see Fig. 12). The transport energy is 5 keV/u, given by the injection velocity into the RFQ cavity. The travel length in the separator section, from the high vacuum EBIS to the accelerating RFQ cavity, is approximately 8 m. Highly charged ions have at this velocity a large electron capture cross-section due to charge-exchange processes with the residual gas. The Müller and Salzborn formula [217] was used to calculate the electron capture cross-section. A conservative residual-gas ionization energy of 10 eV and a pressure of 10^{-8} mbar were assumed. The losses through the separator are listed in Table 6 for ions with different charge states. As can be seen, to keep the loss level inside the separator below 10% also for very highly charge ions a residual gas pressure of less than 10^{-8} mbar is mandatory until the ions are being accelerated inside the RFQ cavity. A vacuum upgrade is therefore required as the present pressure in this section is a few 10^{-7} mbar.

For 3 MeV/u and above the capture cross-section in the residual gas according to Schlachter [218] is $<10^{-15}$ cm^2 for one of the worst cases ($q = 85+$). Thus a relaxed vacuum pressure of $<10^{-6}$ mbar in the high energy end of the linac and the transfer line to TSR is sufficient in order not to lose more than 10% of the beam. In the RFQ and IHS a pressure better than 10^{-7} mbar is believed to be sufficient.

3.1.5 Charge breeder upgrade

As presented above, the current REXEBIS charge breeder in combination with the 10 MeV/u HIE-ISOLDE linear accelerator can provide beams, either directly or with the help of a stripper foil at the end of the linac, with a charge state corresponding to the residual gas equilibrium charge state inside the storage ring. In case higher charge

Table 7. Main design parameters for an upgraded EBIS/T charge breeder aimed to produce VHCI for injection into TSR.

Electron current	>5 A
Electron current density	>20 kA/cm^2
Electron beam energy	>100 keV
Solenoid field	>6 T
Full-field trap length	>50 cm
Trap region pressure	$<10^{-13}$ mbar

states are desired in order to reduce the electron cooling time, or very highly charged ions (VHCI) are requested by certain experiments, an upgrade of the charge breeding system is mandatory. A couple of different upgrade options are outlined below. From a beam particle intensity point of view, the present REX low-energy system is capable of fulfilling the experimental demands as long as a too low injection repetition rate is not imposed by the experiment.

Two highly performing EBIS/T are the RHIC EBIS at BNL [219] and ReA3 EBIT at NSCL MSU [220]. The operational RHIC EBIS, providing large quantities of He, Fe and Au ions, has the electron beam current record of more than 10 A (pulsed) and an impressive extractable ion space-charge of $5 \cdot 10^{11}$ charges/bunch. The electron beam energy is also higher (15 keV) than for REXEBIS allowing higher charge states (in principle fully stripped for $Z < 32$) to be reached. Even higher electron beam energies are relatively easy to achieve with minor modifications. The electron current density is limited to 575 A/cm^2 so the EBIS is not suitable for production of VHCI, but would in any case speed up the breeding time by a factor of 4 compared with REXEBIS.

For the production of VHCI as discussed in Sect. 3.1.2 a high electron beam energy in combination with a large electron current density are needed. The main design parameters are listed in Table 7, yielding maximum breeding times of around 1 s for the requested ions. The ReA3 EBIT is designed to perform charge breeding of radioactive ions very rapidly and therefore has an electron beam current density exceeding 10^4 A/cm^2, possibly reaching 10^5 A/cm^2. The electron current is compressed by a 6 T solenoid field. The electron energy is limited to 30 keV and the electron current to 1.5 A in a first stage, later 2.5 A. The ReA3 EBIT is presently in the commissioning stage. This device is the one with design parameters closest to what would be needed to produce VHCI for TSR at ISOLDE. To fully meet the VHCI requirements the electron beam energy has to be increased and special attention has to be paid to the pressure in the trapping region (see Table 7) in order to avoid competing charge exchange losses. Presently there are four EBIT devices capable of producing VHCI: the SuperEBIT at LLNL [221], the Tokyo EBIT at the University of Electro-Communications [222], the Heidelberg EBIT at MPI-K Heidelberg [223] and the Shanghai EBIT [224]. None of them are however designed for charge breeding, thus the efficiencies are very low, and the electron beam currents and densities are modest, <0.5 A and 5 kA/cm^2, respectively.

An upgraded breeder could be placed at the present position of REXEBIS and make use of the cooling and bunching features of REXTRAP. It would furthermore use the existing REX mass separator. As long as the ion throughput limitation is not of major concern this is the most straightforward option. Alternatively, the breeder could be placed at the present position of REXTRAP, thereby suppressing the REXTRAP-REXEBIS combination and avoiding the ion throughput limitation of REXTRAP. A compact Nier-type spectrometer as presently in use by REX-ISOLDE, combining an electrostatic bender with a magnetic bender, would connect the breeder

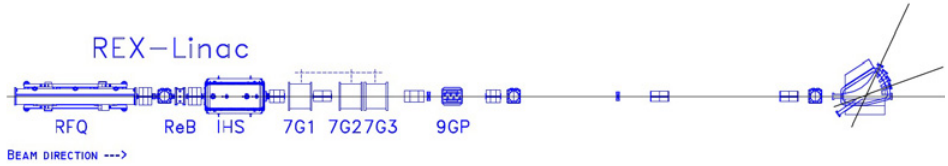

Fig. 21. REX-ISOLDE normal-conducting linac layout.

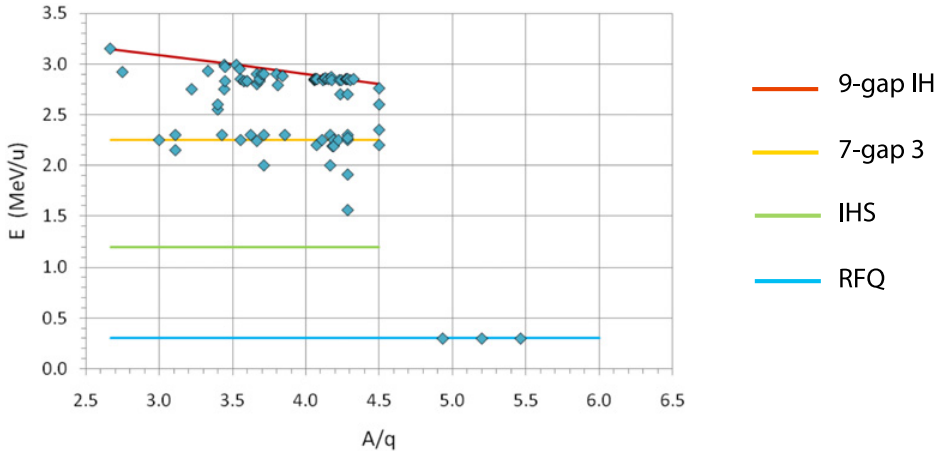

Fig. 22. REX linac maximum energy as a function of A/q. The dots indicate accelerated beams and the colour coding the attainable energy for each cavity.

with the linac. For such a placement the efficiency of the direct cw 1+ ion injection from ISOLDE into the breeder would have to be verified as well as the influence of the high magnetic field from the breeder on the surrounding beam lines at ISOLDE. Most importantly, the injection repetition rate into TSR would then affect the breeding charge state as the decoupled storage in REXTRAP is suppressed. Alternatively the preceding RFQ cooler ISCOOL could possibly be used as a trapping device.

3.2 REX-ISOLDE and HIE-REX performances

3.2.1 Introduction: The normal conducting (NC) REX-linac

The current REX-ISOLDE linac (see Fig. 21) consists of a Radio Frequency Quadrupole (RFQ) accelerator [225], an Interdigital H-type structure (IHS) [226] and three 7-gap split-ring resonators [227] all operating at 101.28 MHz. The first two structures accelerate the ion beam to 0.3 MeV/u and 1.2 MeV/u, respectively. The three 7-gap resonators allow a variation of the final beam energy between 1.2 and 2.3 MeV/u. In addition to this set-up, a 202.56 MHz 9-gap IH structure [228] was installed in 2003/2004 to increase the final energy to 3.0 MeV/u. The maximum duty cycle is 10% and the highest repetition frequency 100 Hz. The largest mass-to-charge ratio is 4.5, however the maximum beam energy of 3.0 MeV/u can only be reached for $A/q \leq 3.5$ (see Fig. 22). The RFQ can accelerate beams with a higher A/q up to about 5.5, for example a beam of $^{153}Sm^{28+}$ ($A/q = 5.46$) has been accelerated.

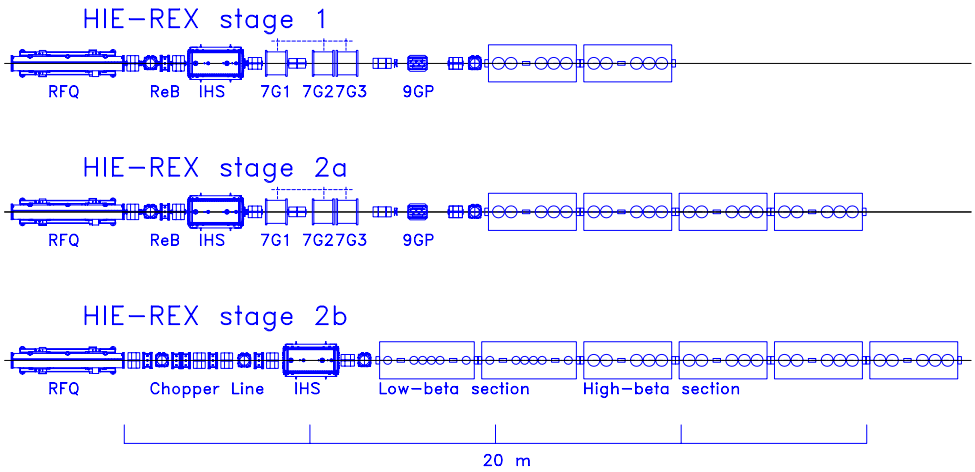

Fig. 23. HIE-ISOLDE linac stepwise installation.

3.2.2 HIE-ISOLDE SC linac stepwise installation

In the framework of the HIE-ISOLDE upgrade project, the construction of a SC linac employing quarter wave resonator (QWR) cavities is planned to increase the final energy of post-accelerated radioactive ion beams at ISOLDE to over 10 MeV/u. The linac will utilize two types of QWR cavities with respectively 6.3% and 10.3% geometric reduced velocities to cover the full velocity range from 1.2 to 10 MeV/u. The QWR cavities will be distributed in six independent cryomodules (6 cavities per cryomodule for the low-β section and 5 cavities per cryomodule for the high-β section). The transverse focusing will be provided by SC solenoids installed in the cryomodules so that beam waists will be located in the inter-cryomodule region where beam diagnostics and kickers can be installed. The HIE-REX SC linac will be installed in three phases (see Fig. 23):

1. Installation of two high-β cryomodules (10 QWR cavities) behind the 9-gap to bring the final energy to >5.5 MeV/u for $A/q = 4.5$.

2.a. Installation of two more high-β cryomodules to reach 10 MeV/u for $A/q = 4.5$.

2.b. Replacement of the energy-variable part of the NC linac with two low-β cryomodules (12 QWR cavities). The first high-β cryomodule is shifted to the end of the linac and the IHS is moved forward to create space for a chopper line between the RFQ and IHS allowing for beams with a 10 MHz pulse structure.

The installation of the first two cryomodules is foreseen for mid 2014, and the final cryomodule installation for 2017. At this point, only the RFQ, and IH structure will remain from the NC linac.

3.2.3 Beam energy

The HIE-ISOLDE linac energy will be fully variable between 1.2 and 10 MeV/u for $A/q \leq 4.5$ with maintained beam quality, as shown in Fig. 24. The high flexibility of the SC linac will allow for higher energies to be attained for lower A/q, for example ions with $A/q = 2.5$ will be accelerated to over 14 MeV/u. A deceleration of the beam

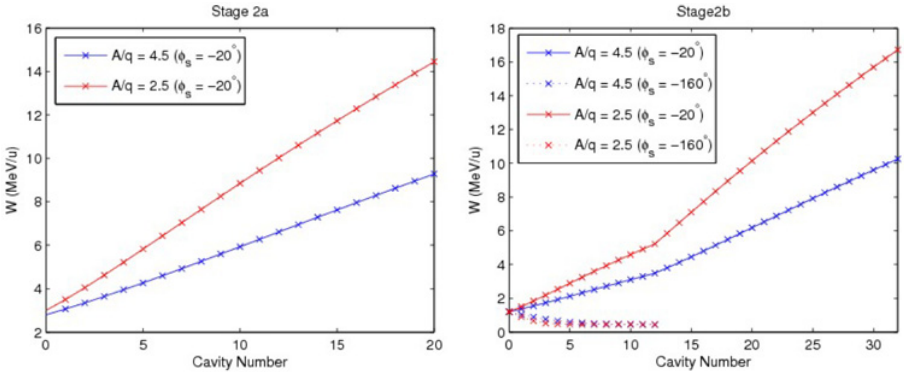

Fig. 24. HIE-ISOLDE linac energy as a function of cavity number for stage 2a (left) and stage 2b (right). The possibility of decelerating the beam is also shown in the right panel.

Table 8. Expected longitudinal beam parameters at the SC linac output.

	Long. emittance (ns·keV/u)		Energy spread (%)	
	rms	95%	rms	95%
Stage 1: (5.5 MeV/u)	0.6	3.8	±0.25	±0.60
Stage 2b : (10 MeV/u)	0.3	2.1	±0.14	±0.34

energy down to about 0.45 MeV/u can be performed by using the low-beta cavities after the IHS cavity, although with a reduced beam quality. In the cases where the full acceleration voltage is not required the last cavities can be used as de-buncher/re-buncher for longitudinal emittance manipulation.

3.2.4 Longitudinal emittance/energy spread

The longitudinal emittance has recently been measured behind the RFQ and behind the 7-gap 2 cavity to be respectively 1.48 and 1.55 ns·keV/u 86%-emittance [229]. These values are consistent with the design input emittance of 2 ns·keV/u for the HIE-ISOLDE linac, and the specified design output phase- and energy-spread of the RFQ of ±15° and ±1.5% (<1.85 ns·keV/u).

The expected longitudinal emittances and energy spreads at the output of the SC linac are given in Table 8. A dedicated bunching cavity situated in between the HIE linac and TSR could reduce the energy spread, although most likely not sufficiently to reach isobaric mass separation using the mass-selective acceleration method inside TSR. The last cavities in the HIE linac can be used to manipulate the energy spread of the injected beam.

3.2.5 Transverse emittance

The transverse emittance of the REX-ISOLDE linac has been studied during several measurement campaigns, the last ones in 2006 and 2008. The normalized 90%-emittance as a function of energy is summarized in Fig. 25. The emittance is increasing through the linac from about 0.15 mm mrad at 300 keV/u to about 0.25 mm mrad at 2.85 MeV/u. The emittance growth occurs mostly in the IHS. The emittances measured in the horizontal direction are in general larger than in the vertical direction.

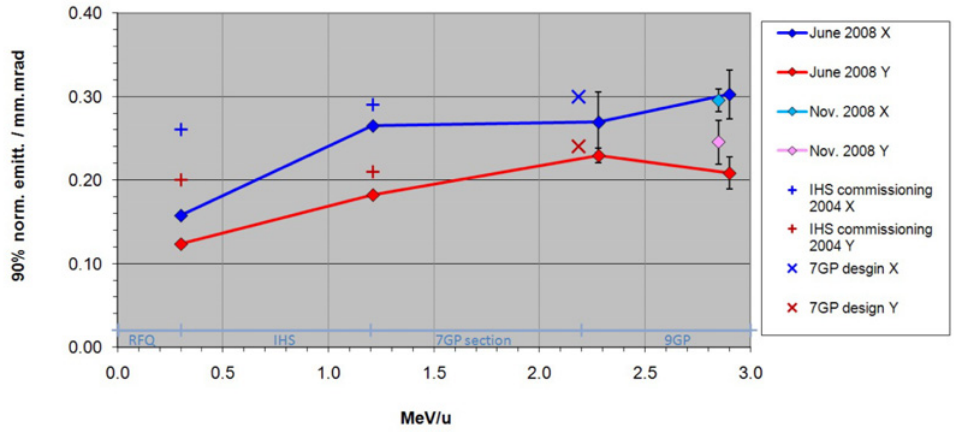

Fig. 25. REX-ISOLDE transverse normalized emittance as a function of energy.

This could be due to the horizontal slit at the exit of the separator or due to aberration in some of the linac quadrupoles (e.g., IHS inner triplet). Assuming a 0.30 mm mrad 90% transverse emittance at the RFQ output, the expected emittance at the output of the SC linac is 0.47 mm mrad.

3.3 Transfer beam line layout

3.3.1 HIE-ISOLDE linac transfer lines

The transfer lines of HIE-ISOLDE linac will use a quasi-FODO lattice with a 90° phase advance per period. The layout is shown in Fig. 26. Two of the periods directly behind the linac will be replaced by achromatic switchyards serving two multipurpose experimental stations. The option for a third beam line turning right towards a possible hall extension is open. The main experimental station where the final position of Miniball will be is served by a transfer line with two 90° achromatic bends. A large floor space (10 m × 8 m) is reserved behind Miniball for a future recoil separator.

The option of having laminated magnets in the transfer beamlines is considered both for pulse mode operation and for cost reasons. Pulsed operation would be beneficial as it would enable other experiments, for instance Miniball, to take part of the radioactive beam while the stored beam inside TSR is exploited. At a first stage normal non-pulsed power supplies are foreseen for the transfer lines at HIE-ISOLDE so the switching time will be in order of seconds, but this could later be upgraded in order to attain switching times shorter than a second.

3.3.2 Transfer line from the HIE-ISOLDE linac to the TSR

Several options have been considered for the installation of TSR at ISOLDE. The scenario considered here is the installation of the ring in a new building located at the back (west side) of the ISOLDE experimental hall. The floor of the new building would be approximately 2.8 m above the floor of the existing hall due to an essential infrastructure tunnel preventing the ring from being at equal height of the transfer beam line. For this reason it is proposed to build a vertically inclined chicane behind

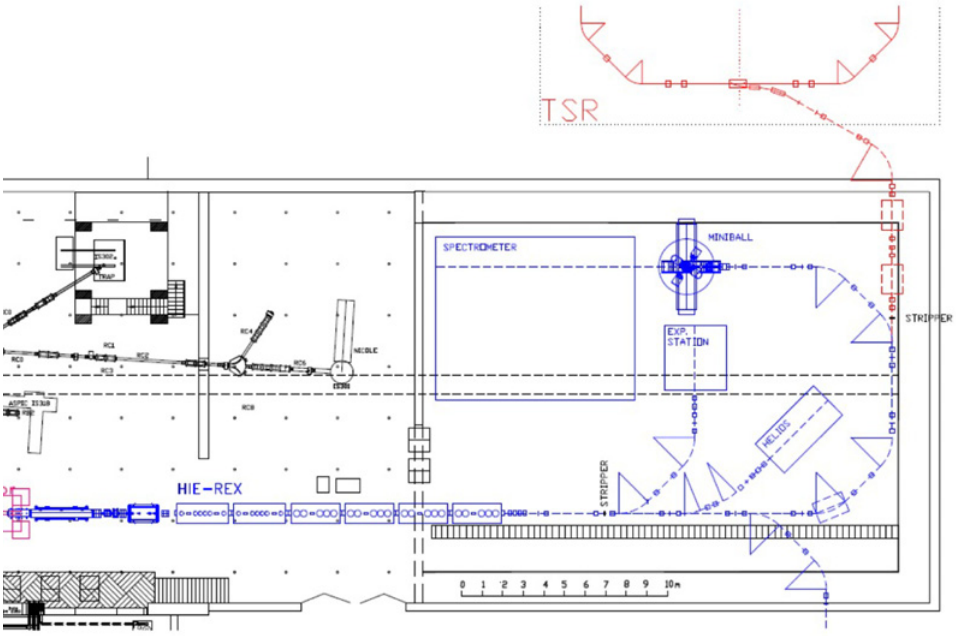

Fig. 26. HIE-REX transfer lines layout and connection to the TSR.

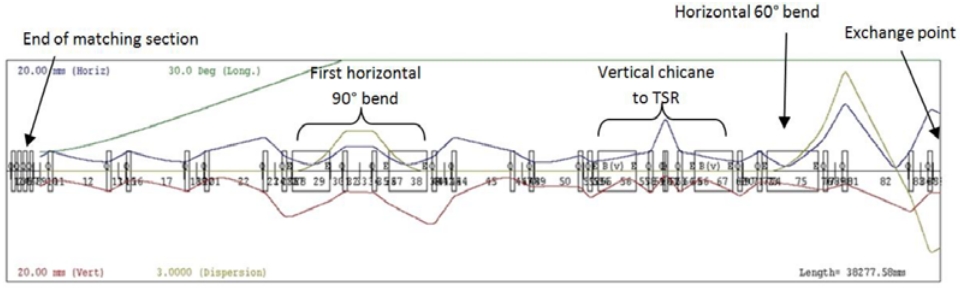

Fig. 27. Beam transport of $A/q = 4.5$ ions at 10 MeV/u from the HIE-REX output to the TSR injection line (Trace3d). Phase space matching into TSR not included.

the second 90° bend of the Miniball line to bring the beam at the correct level for injection into the TSR. The connection with the TSR injection line would involve another 60° horizontal bend which is not yet designed. The vertical switchyard could use the same magnet type as the one foreseen for the Miniball line and the first multipurpose experimental station. A possible beam transport scheme from the linac hand-over point to the end of the vertical section is showed in Figs. 27, 28 and 87.

4 The storage ring TSR

4.1 Introduction

In the late eighties and beginning of the nineties a number of laboratories started construction of synchrotons or small storage rings for light and heavy ions for research in various fields of atomic, molecular and nuclear physics. The small rings

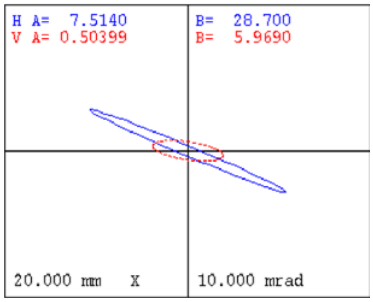

Fig. 28. Beam phase space parameters at the exchange point.

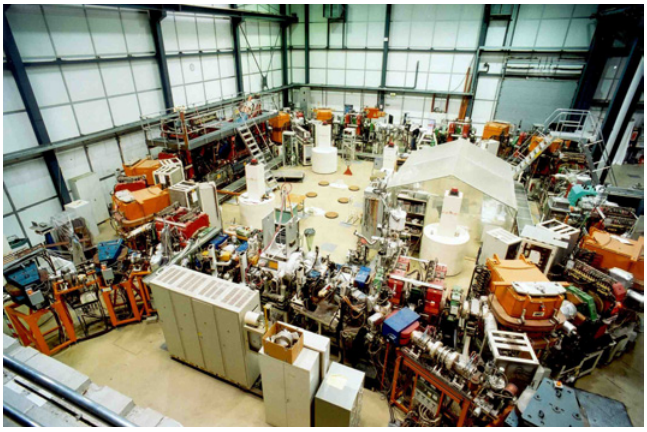

Fig. 29. The heavy ion storage ring TSR.

became possible due to the successful demonstration of phase space cooling [230] as well the progress in vacuum technology allowing vacua in the 10^{-12} mbar regime to be achieved in accelerators at moderate cost. Both features are crucial when storing highly charged particles of large intensity at energies of a few tens MeV/u. This is because the emittance growth of the beam due to Coulomb scattering of the ions by themselves (intra beam scattering), by the residual gas or by the internal target material as well as the large cross sections for electron pick up give stringent limits to the beam lifetime. The sudden interest in the technology, developed at high energy accelerators, was strongly influenced by the success of the CERN Low Energy Antiproton Ring LEAR [231] which already incorporated many of the items necessary for the rings and which encouraged the accelerator community to apply the techniques of cooling stored beams to less rare and exotic ions than antiprotons. In fact there are many fields of physics where heavy ion storage rings are valuable. It is especially atomic, nuclear and astro-physics which benefit from the cold intense beams interacting with electrons from the cooler which serves as an internal target. Various charge changing processes important for atomic-, molecular-, plasma- and astrophysics, such as radioactive electron capture, dielectronics recombination and dissociative recombination are studied. The heavy ion cooler storage ring located at MPI for nuclear physics shown on Fig. 29 belongs to this family of heavy ion cooler storage rings.

The 55.4 m circumference storage ring has four straight sections. The first straight section is devoted for the injection and extraction equipment. In the next straight section there is the electron cooler followed by the straight section for the experimental

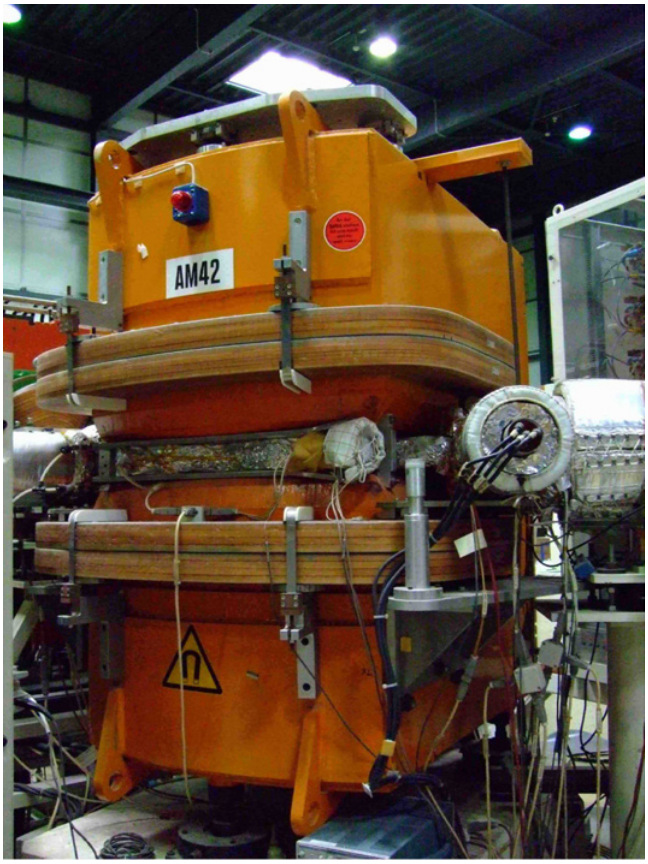

Fig. 30. TSR dipole magnet.

equipment. The last straight section is used for the rf-system and beam-diagnostics system.

4.2 The magnet system of the TSR

The bending fields in the TSR are provided by eight 45° curved dipole magnets build from 1 mm laminated steel. The TSR dipole magnet is shown in Fig. 30. Due to the parallel end faces the pole face angle is $\epsilon_1 = \epsilon_2 = 22.5°$. The maximum field is 1.3 T. The main parameters of the dipole magnets are given in Table 9.

The C-shape of the yoke with the opening oriented towards the outside of the ring facilitates access to the vacuum chambers. The two coils (2×72 turns) are separated by 305 mm to use the space in the fringe field region for pumps. The yoke of the magnet is fabricated from 880 laminations. Due to large pole face angle ϵ the structure of the fringe field does have a strong influence on the integrated field, thus endblocks for proper shimming with an overall approximated Rojowski-profile are attached to the yoke. Careful analysis of the magnetic fields yielded a small quadrupole and a sextupole component, the main contribution being given by the fringe field. To a good approximation the integrated field versus the horizontal aperture x is represented in the useful field region by:

$$\int B(x)dl = (1 + ax + bx^2)B_0 l_{eff}, \tag{2}$$

Table 9. Basic parameters of the TSR dipole magnets.

Basic parameters	
Gap	h = 80 mm
Nominal field	B = 1.3 T
Bending radius	$\rho = 1.15$ m
Deflection angle	$\alpha = 45^\circ$
Pole face angle	$\epsilon_1 = \epsilon_2 = 22.5^\circ$
Coil	
Max. current	I = 850 A (2×72 turns)
Conductor	$14.9 \times 14.9\,\text{mm}^2$
Cooling hole diam.	6 mm
Current density	$4.4\,\text{A/mm}^2$
Correction coil	30 backleg windings, air cooled
Magnet	
Resistance	R = 43.2 mΩ
Inductance	L = 44 mH
Max. power	P = 31.2 kW
Weight copper	800 kg
Steel	12000 kg

Table 10. Basic parameters of the TSR quadrupole magnets.

Basic parameters	
Aperture radius r	0.1 m
Max. Gradient	7.5 T/m
Corresponding strength	$5\,\text{m}^{-2}$
Iron Length	0.25 m
Effective magnet length	0.376 m
Coil	
Max excitation current	550 A
Number of turns	4×37
Conductor	$14.1 \times 14.1\,\text{mm}^2$
Magnet	
Resistance	R = 24 mΩ
Inductance	21.3 mH
Max. Power	7.3 kW
Iron weight	1.9 t
Copper weight	0.36 t

with coefficients $a = -0.016\,\text{m}^{-1}$ and $b = -0.37\,\text{m}^{-2}$. The variation of the effective magnetic length l_{eff} was measured to be very small: $\Delta l_{eff} < 1.5$ mm for $0 < B < 1.3$ T.

To focus the beam the TSR has 20 quadrupole magnets grouped in 5 families. As the parameters of these families are not too different, only one type of quadrupole is used in the ring because of cost reasons. Figure 31 shows a photograph of one quadrupole magnet of the TSR. Table 10 lists the basic parameters of the quadrupole. To correct the chromaticity of the storage ring and to excite third order resonances sextupole magnets are used at the TSR. Figure 32 shows a photograph of a sextupole magnet. Each sextupole has three coils located on every second pole to excite the sextupole field. The characteristics of the sextupole magnets are given in Table 11.

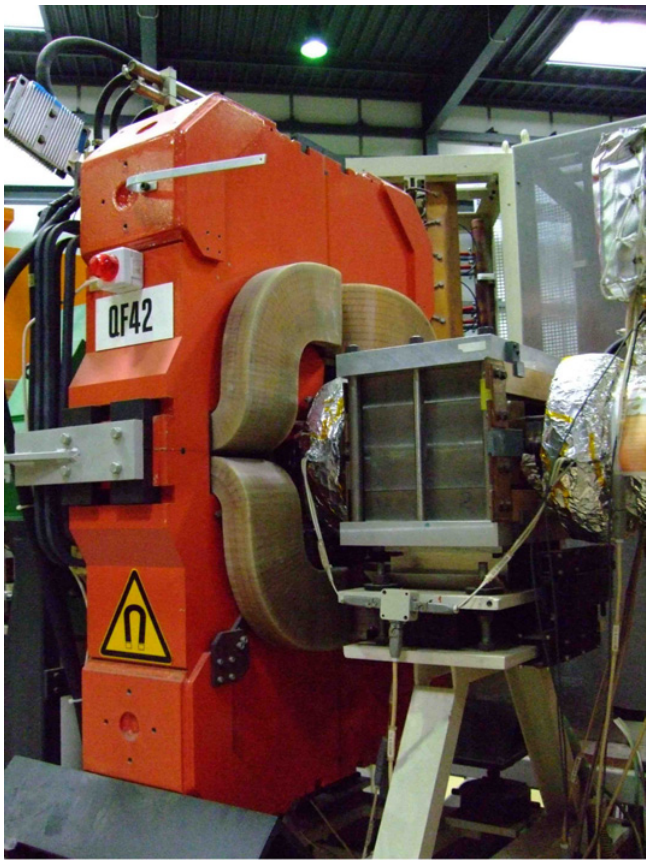

Fig. 31. TSR quadrupole magnet. In the front of the quadrupole magnet a bump magnet used for multi turn injection is visible.

4.3 The lattice of the TSR

The storage ring has a fourfold symmetry and a circumference of 55.4 m. The lattice of TSR is shown in Fig. 33. The horizontal focussing quadrupoles shown in Fig. 33 are marked with QF and the vertical focussing quadrupoles are labelled with QD. The four dipoles in the straight section of injection and extraction, used to create a time independent closed orbit bump, are labelled with LB. BM are the bump magnets necessary for multi-turn injection. Deflection is accomplished by eight 45 degree C-shaped magnets, labelled with AM in Fig. 33. Always two dipoles with quadrupoles in between form the center of the focusing period, which is completed on both sides by the quadrupole doublets. In the main operation mode of the ring two anti-symmetric focusing periods form one of the two super-periods. Figure 34 shows the beta functions β_x (solid line), β_y (dashed line) as a function of the position s. Due to the super-periodicity of two the beta functions are repeated after one half of the revolution. The position $s = 0$ marks the center of the straight section where the rf-system is located. Injection into the storage ring takes place in the next (going clockwise in Fig. 33) straight section. At the position of the electrostatic septum $s \approx 15\,\mathrm{m}$ the horizontal β function is about 6 m and the vertical one is about 2.5 m.

The electron cooler is located in the following straight section at the position of $s \approx 28\,\mathrm{m}$. Due to the super periodicity of two this straight section has the same Twiss

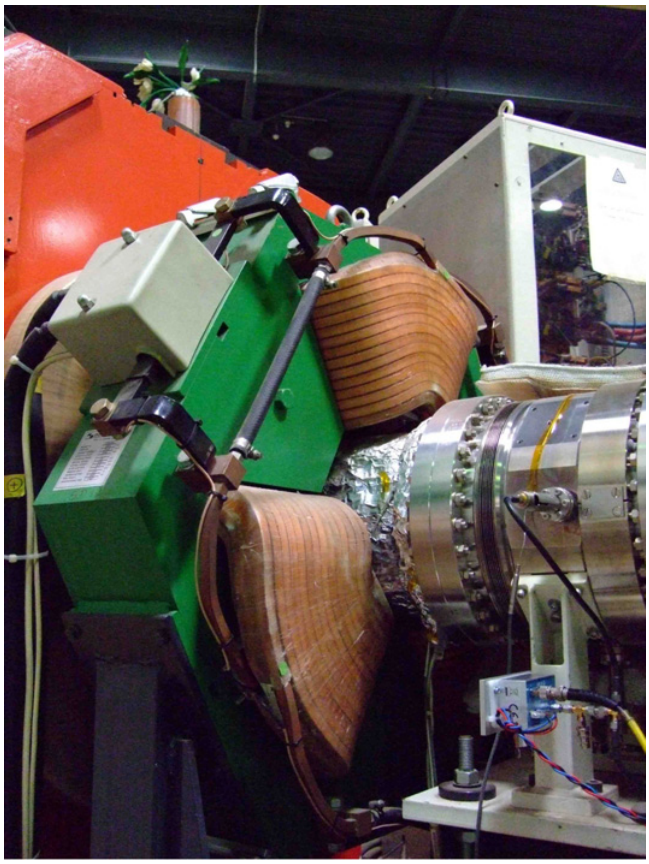

Fig. 32. TSR sextupole magnet. In the front of the sextupole magnet a capacitive pick up to measure the closed orbit of the ion beam is recognizable.

Table 11. Basic parameters of a TSR sextupole magnet.

Aperture radius r	0.125 m
Max. gradient d^2B/dr^2	50.5 T/m^2
Effective magnet length	0.205 m
Max excitation current	450 A
Maximum Voltage	13 V
Total weight	0.65 t

parameter as the straight section with the rf-system and beam diagnostics. The last straight section is devoted to experiments. In the center of this straight section the horizontal and vertical beta-functions are $\beta_x = 6\,\mathrm{m}$ and $\beta_y = 2.2\,\mathrm{m}$ and are therefore approximately double of the corresponding values in the cooler straight section. The horizontal beam size is maximum in the horizontal focusing quadrupoles where the horizontal β-function exceeds a value of $\beta_x = 17.4\,\mathrm{m}$, whereas the maximum vertical beam size is found in the vertical focusing quadrupoles situated in the straight sections of the electron cooler and rf-system. From the horizontal β_x – function ($\beta_x = 4\,\mathrm{m}$) at the position of the residual gas beam profile monitor ($s = 1.5\,\mathrm{m}$) and the maximum possible horizontal beam size, obtained after multiturn injection, the horizontal acceptance of the storage ring can be calculated. Figure 35 shows the measured horizontal beam size for a $^{12}C^{6+}$ (E = 73.3 MeV) ion beam directly after the multi-turn

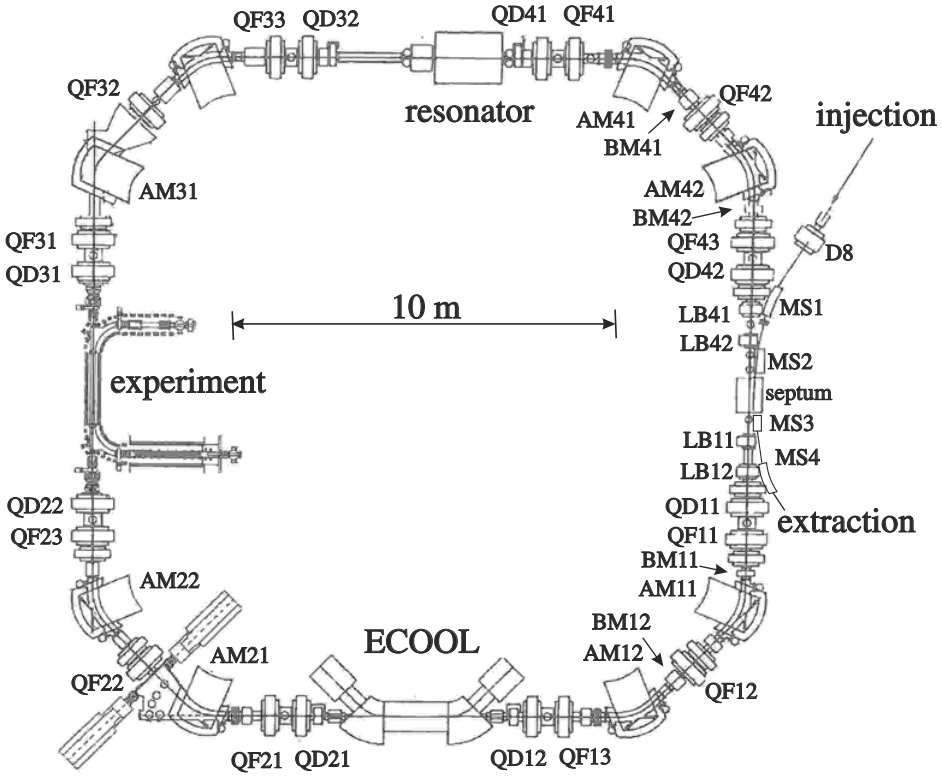

Fig. 33. The lattice of the TSR.

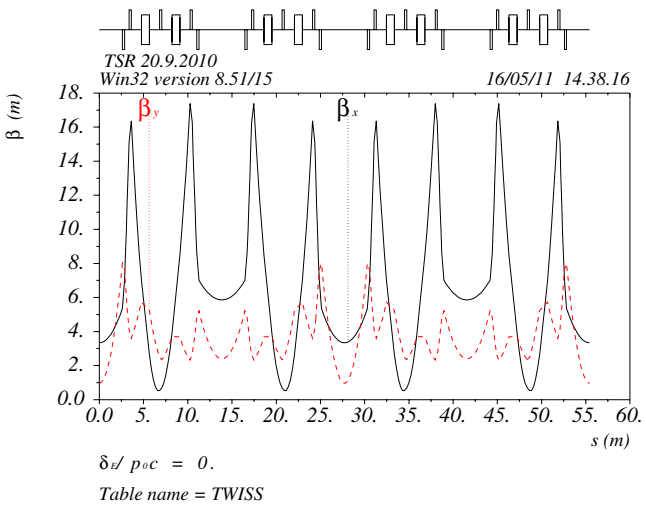

Fig. 34. Beta functions β_x (black line) and β_y (dashed line) calculated by the program MAD8 [232] (main operation mode).

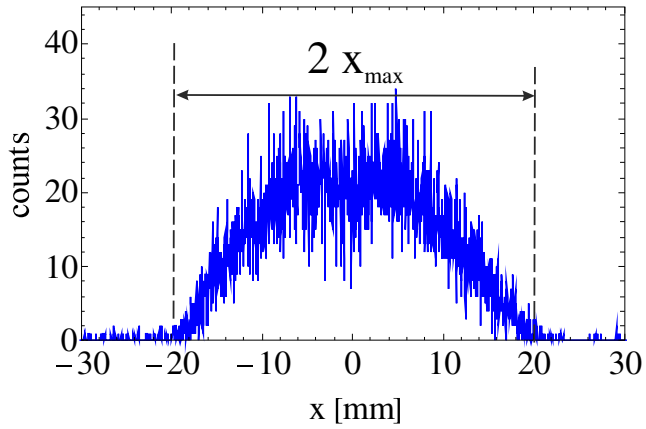

Fig. 35. Measured horizontal beam profile after multiturn injection.

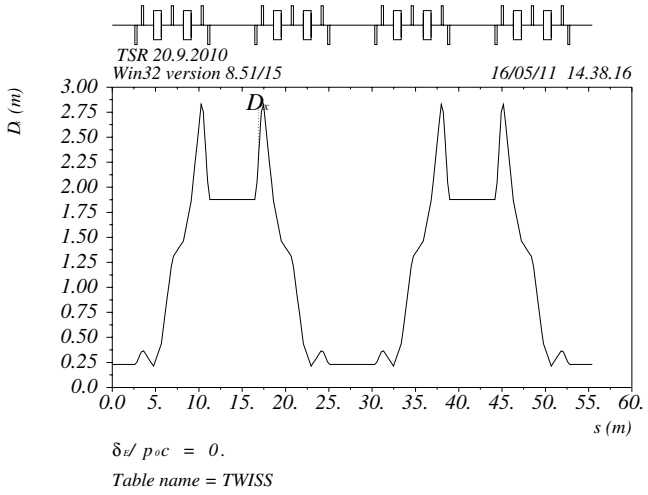

Fig. 36. Dispersion function of the TSR, D_x, calculated by the program MAD8 [232] (main operation mode).

injection. From $x_{max} = 20\,\text{mm}$ (compare Fig. 35) and $\beta_{x,M} = 4\,\text{m}$ a horizontal acceptance of the storage ring of $A_x = x_{max}^2/\beta_{x,M} = 100\,\text{mm mrad}$ is obtained. Due to the low dispersion function at the position of the beam profile monitor $D_M \approx 0.25\,\text{m}$ and the small momentum spread of the carbon ion beam $\Delta p/p \approx 10^{-4}$, used to determine the acceptance of the storage ring, the contribution of the momentum spread to the measured beam profile can be neglected.

The dispersion function of the storage ring is displayed in Fig. 36. The dispersion is set to low value $D_x \approx 0.25\,\text{m}$ in two long straight section of the TSR, while it is finite and adjustable to values around 2 m in the other two sections. The sections without dispersion are reserved for the electron cooler and the rf-system, while injection and experimental setups are to be found in the dispersive ones. The dispersion in the dipole magnets determine the α and γ_{tr} parameters of the storage ring as defined by:

$$\alpha = \frac{1}{\gamma_{tr}^2} = \frac{\Delta C/C}{\Delta p/p} \tag{3}$$

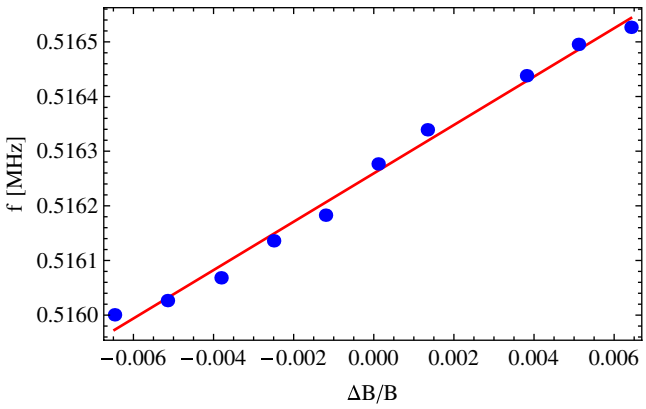

Fig. 37. Measured revolution frequency as a function of the magnetic field change $\Delta B/B$. The red line is a linear fit.

and is given by [233]:

$$\alpha = \frac{1}{\gamma_{tr}^2} = \frac{1}{C} \oint \frac{D(s)}{\rho(s)} ds, \tag{4}$$

where $\Delta C/C$ is the change of the circumference C of storage ring by changing the momentum p of the ions, D is the dispersion function and ρ is the curvature radius of the central orbit. In order to measure γ_{tr} of the storage ring all magnetic fields of the storage ring was changed by $\Delta B/B$, which has the same effect on the length of the closed orbit as a change of the particle momenta by $-\Delta p/p$ [234,235]. Since $\Delta C/C = -\Delta f/f$ ($\Delta f/f$ is the relative shift of the revolution frequency), from Eq. (3) follows:

$$\alpha = \frac{1}{\gamma_{tr}^2} = \frac{\Delta f/f}{\Delta B/B}. \tag{5}$$

The revolution frequency was measured via a Schottky noise analysis. In Fig. 37 the measured revolution frequency as a function of the magnetic field change $\Delta B/B$ is shown. From the slope of the fit (red line) a gamma transition parameter of $\gamma_{tr} = 3.4$ can be derived. From the γ_{tr} parameter the slip factor η can be derived describing the relation between the revolution frequency and the particle momentum:

$$\eta = \frac{\Delta f/f}{\Delta p/p} = \frac{1}{\gamma^2} - \frac{1}{\gamma_{tr}^2}, \tag{6}$$

where γ describes the relativistic energy ($E = \gamma mc^2$). For the TSR energies ($\gamma \approx 1$) the slip factor is then $\eta = 0.91$.

The working point of the TSR main operation mode, given by the horizontal and vertical tunes, is shown in Fig. 38. Up to 4^{th} order resonances are shown. The most dangerous are the 1^{st} order resonances which are at $Q_x = Q_y = 2.0$ and 3.0 in this Figure. The second order resonances are highlighted in blue color. The red color marks the third order resonances and the green color indicates the forth order resonances. The typical working point (Q_x=2.88, $Q_y = 2.86$) is close to the resonance $Q_x = Q_y$ which couples the horizonal and vertical motion.

Due to the chromaticity $Q'_{x,y}$ the horizontal and vertical tunes depend on the momentum of the particle:

$$Q'_{x,y} = \frac{\Delta Q_{x,y}}{\Delta p/p}. \tag{7}$$

To measure the chromaticity the momentum of the ion beam was shifted by electron cooling and the corresponding change of the tune was measured using the beam

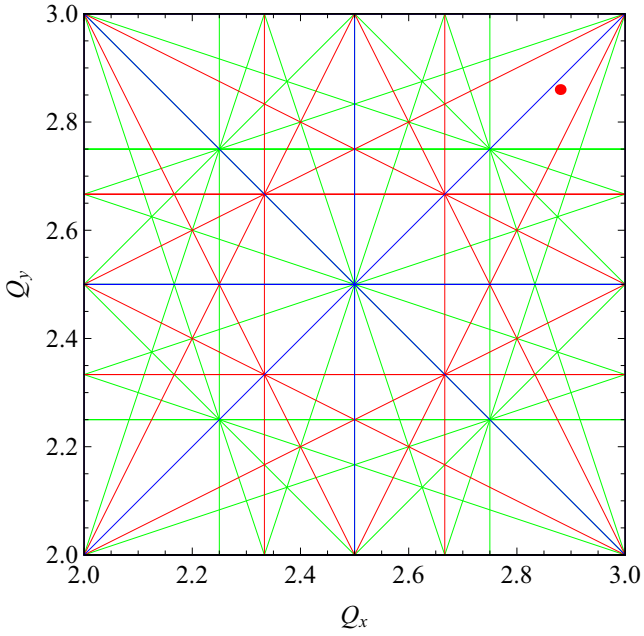

Fig. 38. Working diagram with typical working point of the main operation mode.

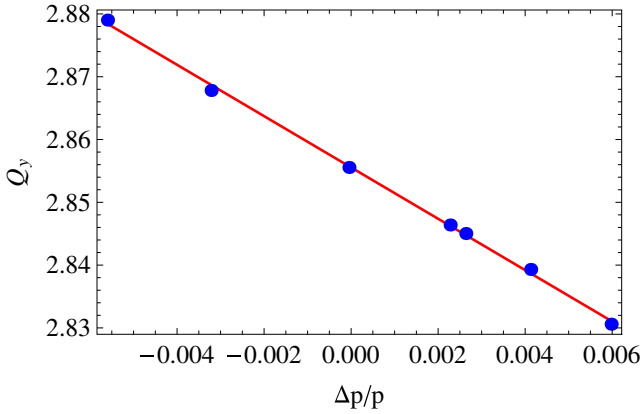

Fig. 39. Vertical tune as a function of the momentum shift $\Delta p/p$.

transfer function (BTF) measurements. In Fig. 39 the dependency of the vertical tune on the momentum shift $\Delta p/p$ is shown. From the fit (red line) a vertical Chromaticity of $Q_y^{'} = -4.1$ can be derived. Similar measurement for the horizontal chromaticity results in $Q_x^{'} = -7.4$. The chromaticity corrections use three families of sextupoles since there are three quantities to be corrected: horizontal and vertical chromaticities and the orbit dispersion in the straight sections with low dispersion.

4.4 The multi charge operation mode

Experiments carried out at the TSR require sometimes completely different settings of the TSR storage ring. The most important mode at the TSR is the standard mode described in Sect. 4.3. This mode is characterized by its large acceptance in the horizontal and vertical phase space. The machine properties of the TSR are best

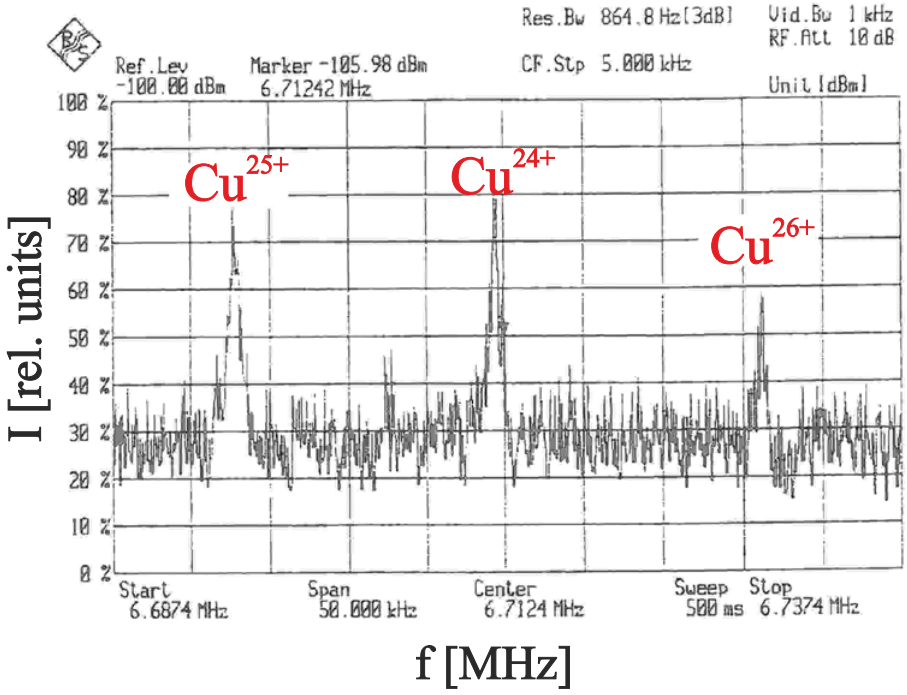

Fig. 40. Confirmation of the multi charge operation at the TSR by using the Schottky noise analysis [236].

known in that standard mode. The maximum of the dispersion function however limits the momentum acceptance of the storage ring. To store simulaneously several charge states of the ion beam a large momentum acceptance of the storage ring is required. In addition the natural chromaticity has to be corrected with sextuple magnets to avoid losses of the differently charged ions due to resonances. The most important demand on the lattice is a decrease of the dispersion function as well as a zero dispersion at the location of the electron cooler to avoid an excitation of the betatron oscillation by changing the charge in the cooler. With the low dispersion mode of the storage ring [236] the requirement of a large momentum acceptance of $\Delta p/p > \pm 4\%$ is fulfilled. To demonstrate the multi charge operation mode at the TSR storage ring, copper ions Cu^{25+} with $E = 266\,\mathrm{MeV}$ were injected. The injected ion beam as well the produced charge states via the electron capture and electron stripping could be determine with the Schottky noise analysis. In Fig. 40 a Schottky spectrum is shown which was taken 12 s after the injection of the ions into the TSR. The charge state 24+ was visible already 2–3 s after the injection. The charge state 26+ was produced in the stripping reaction and was detectable 8 s after the injection. The correlation between the peaks and the charge states was measured with a scraper. The scraper was slowly moved into the vacuum chamber and thus removing one charge state after the other. The dispersion function at the electron cooler was not exactly set to zero thus the revolution frequencies of the three charge states depend on the space charge parabola of the electron beam. Due to the dispersion in the electron cooler the three charge states are spatially separated in the cooler resulting in different revolution frequencies. The position of the three peaks in the Schottky spectrum shown in Fig. 40 can be explained if a dispersion in the cooler of $D = 0.3\,\mathrm{m}$ is assumed [236].

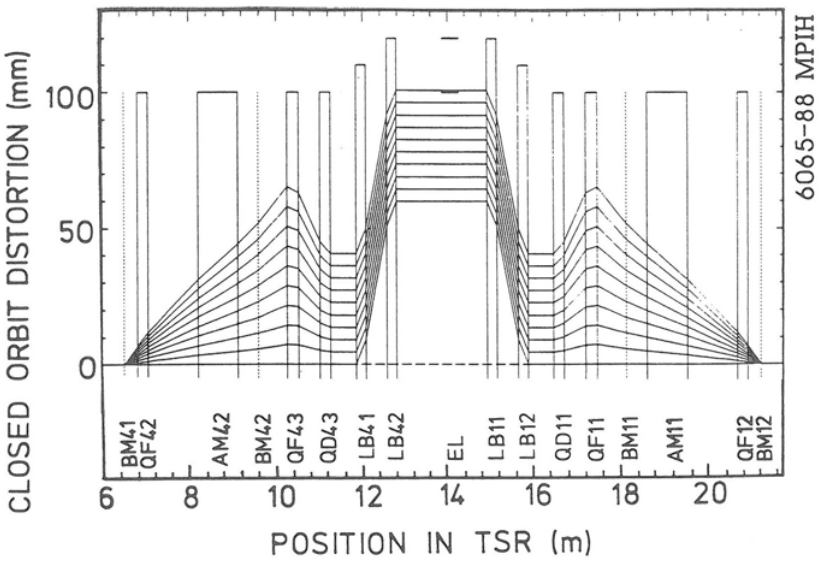

Fig. 41. Time development of the closed orbit distortion in the plane (s, x) during multiturn injection.

4.5 Multi-turn injection

With the multi-turn injection [237] the horizontal acceptance of the storage ring is filled with ions. The description of its principle is given hereafter. The ion beam injection into the heavy ion storage ring TSR is accomplished by means of two magnetic septa and an electrostatic septum, a conceptually simple device (in principle a parallel plate capacitor) which is placed in the very last stage of the transfer line. Its electrical field provides the last kick to the injected particles inflecting them onto the closed trajectory of the ring. In order to fill the ring transverse phase space with the injected beam, the closed orbit and the injection trajectories must be very close to each other after the electrostatic septum. The closed orbit must therefore be distorted in order to pick up the incoming particles at some distance from the ring axis. The distance between the central orbit in the ring and the inner thin electrode of the electrostatic inflector must be large enough to allow all particles which have already been stored in the ring to pass by it without knocking them onto the septum. Four magnets, called bumper magnets (BM41, BM42, BM11, BM12), properly placed along the ring perimeter, two before and two after the injection point, create a bump of the closed orbit so as to make it coincide with the injection trajectory at the injection point. Figure 41 shows the distorted closed orbit (called injection orbit). In our particular lattice four additional magnets (LB42, LB42, LB11, LB12) are necessary to complete the distortion. This is the situation when the magnetic field in the bumpers has the highest value. Now the injection begins: the beam is injected through the injection line and starts filling the horizontal acceptance of the ring in the center. From this moment on the magnetic fields of the bumper magnets are rapidly reduced to zero. The horizontal ring acceptance is thus filled from the center to the edge within a time of approximately 70 turns of the beam in the machine. During the 70 turns the particles are injected with increasing betatron oscillations around the closed orbit. In the phase space shown in Fig. 42 the filling status of the transverse phase space after a time corresponding to 5 turns is displayed. Since the horizontal tune in this simulation is chosen to be close to 2.75, the small ellipse of the injected particles is 90°

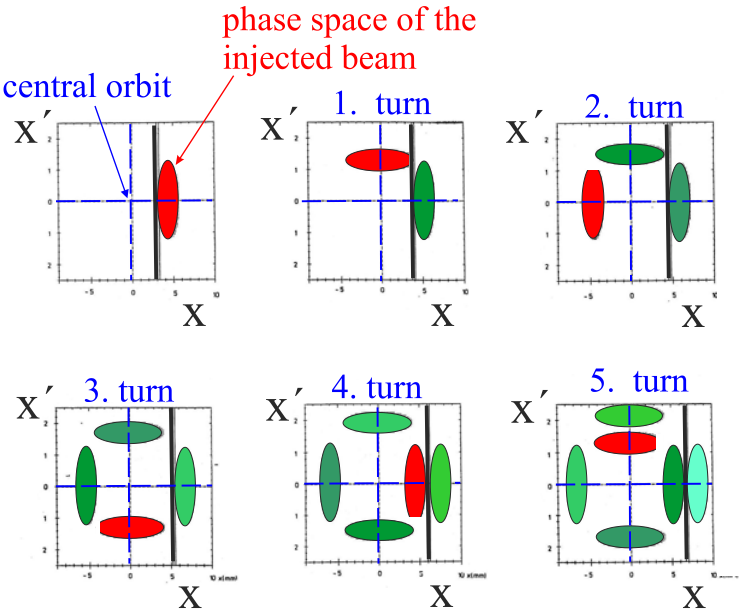

Fig. 42. Time development of the transverse phase space during the first injections into the ring acceptance. Since the distance between the closed orbit increases, most of the particles pass after four turns ($Q_x = 2.75$) the inner side of the septum and are kept safely circulating.

in advance, in the phase space of Fig. 42, with respect to the particles injected in the following turn. The distance between the closed orbit and the electrostatic septum increases, fast enough that after four turns in the ring most of the particles injected four turns before do not knock against the electrostatic septum, but can pass by its inner side and are kept running safely in the ring. The completely filled horizontal phase space of the storage ring TSR is shown in Fig. 43: this is a result of a computer simulation of the multitude injection for the heavy ion storage ring TSR. For the acceptance of the storage ring a value of 100 mm mrad was chosen. The velocity of the injection orbit displacement had to be chosen in order to maximize the particle density in the ring phase space after a complete filling of the acceptance ellipse. The intensity multiplication factor M granted by multi-turn injection can be given as:

$$M = \frac{A_x}{\epsilon_x \cdot D_t}, \tag{8}$$

where A_x is the horizontal acceptance of the storage ring, ϵ_x the injected beam emittance and D_t ($D_t > 1$) is the dilution factor the transverse phase space after multi-turn injection. The cuts to the stored injected beam ellipse are caused by the electrostatic septum foil, which can be recognized in Fig. 43. The cuts contribute significantly to D_t. Computer simulation shows that the acceptance ellipse is filled in a time corresponding to 70 turns. If a tandem beam having a typically emittance of $\epsilon_x \approx 1.5$ mm mrad is used an intensity multiplication factor of approximately 40 [237] can be achieved resulting in a dilution factor of $D_t = 1.7$.

4.6 Electron cooling

After the multi-turn injection a beam, with a horizontal width of approximately 4 cm (compare Fig. 35) at the position of the beam profile monitor is obtained. Using the

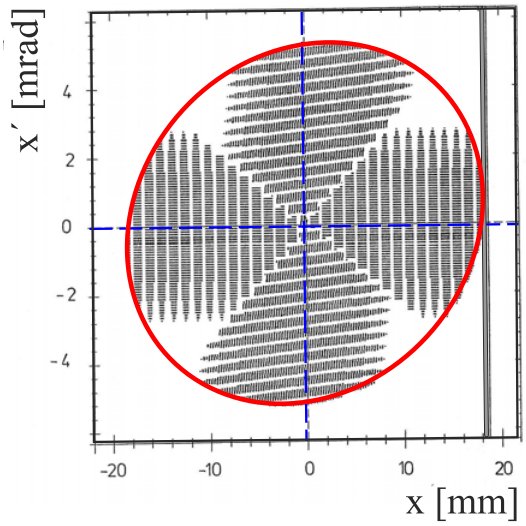

Fig. 43. Completely filled transverse phase space after multi-turn injection.

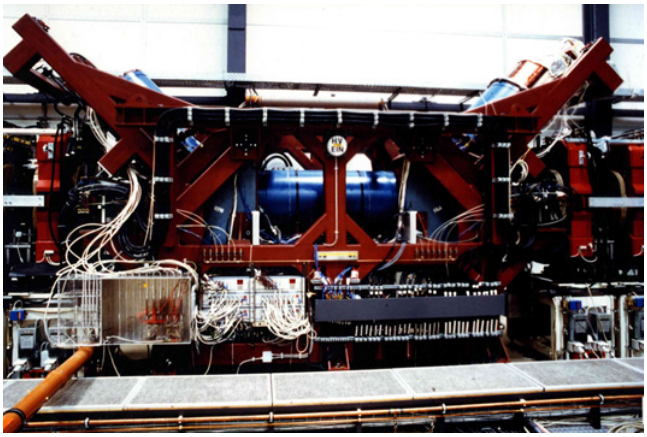

Fig. 44. Photograph of the electron cooler.

Twiss-parameter at the location of the beam profile monitor the measured horizontal spatial distribution can be converted into a velocity one with a transverse temperature of approximately $5 \cdot 10^6$ °C for $E = 73.3\,\mathrm{MeV}$ $^{12}C^{6+}$ ions. With the electron cooling the temperature of the stored ion beam can be decreased. In order to cool the stored ion beam and to highly increase its intensity, the beam is led through a bath of cold electrons in the electron cooler. As in a heat exchanger, the electrons remove the heat from the ion beam, while the cold electron bath is continuously renewed.

4.6.1 The electron cooler

The electron cooler is located in one of the four long straight sections of the storage ring. Figure 44 is a photograph of the electron cooler. The interaction between electrons and ions takes place in the solenoid located in the center of Fig. 44. The basic structure and the locations of the various components can be seen in Fig. 45. The main parameters of the cooler are listed in Table 12. The magnetic field which guides

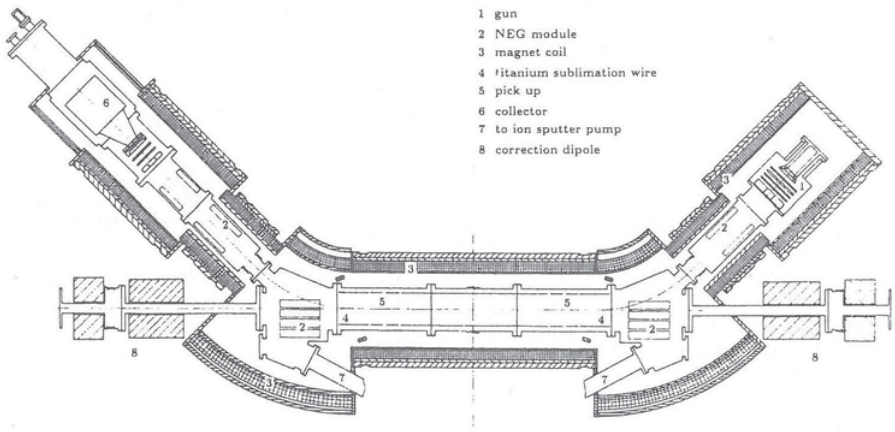

Fig. 45. Cut drawing of the TSR electron cooler showing the gun (1), the NEG pump modules (2), the solenoidal and toroidal magnets (3), the titanium sublimation pumps, the position pick ups (5), the collector (6), pumping ports (7) and the correction dipoles on the ring axis (8).

Table 12. Basic parameters of the electron cooler.

gun perveance	$1\,\mu$ perv
electron energy	up to 14 keV
electron current	up to 0.5 A
expansion factor of the electron beam	up to 30
cathode diameter	3/8 inch
effective cooler length	1.2 m
magnetic field in the cooler solenoid	$\leq$1 kG

the electron beam from the electron gun to the collector consist of five solenoidal and two toroidal coils [238]. The gun solenoid coil is designed for a maximum magnetic field of 12 kG to allow an expansion of the electron beam. The other solenoids and toroids are designed for a maximum magnetic field of 3 kG in order to be able to study cooling with strong magnetic fields. To allow steering of the beam the field direction in the main magnets can be changed by the superposition of transverse fields excited by a pair of dipole saddle coils. Although the length of the straight section in the TSR is 5.2 m, the space needed for the toroids and correction magnets to compensate the closed orbit deflection in the toroid magnets themselves limits the length of the cooling solenoid to 1.5 m. The aperture dimensions for the ion beam in the horizontal degree of freedom in the cooler solenoid and toroid is $\pm$100 mm. The field quality in the main cooler solenoid which is essential for a low electron temperature is ensured by precision windings as well as by powering 7 sets of correction coils. By doing this the root mean square fluctuations of the field direction $\sqrt{\langle B_t^2/B_l^2\rangle}$ were reduced to less than $4 \cdot 10^{-5}$ both horizontally and vertically for an effective length of the cooler region of 1.2 m. The cooler system is designed to operate in a heavy ion ring in which low-energy fully- or even partially-stripped ions should be stored with life-times in the order of minutes. Therefore a residual gas pressure of $5 \cdot 10^{-11}$ mbar or better had to be maintained also in the cooler where high gas loads from the gun and the collector are present. Beside the precaution in assembling the vacuum chambers from specially cleaned, vacuum fired and 300 °C bakeable components a high pumping speed is necessary which is provided by 34 NEG modules (15000 l/s), two 400 l/s and one 60 l/s sputter ion pumps.

The electron beam can be used as a beam cooling device and as an electron target. The transverse temperature of the electron beam is of particular importance for recombination experiments at small relative velocities. Small transverse temperatures can be obtained by adiabatic expansion [239] of the electron beam after acceleration. The transverse temperature $T_\perp$ divided by the longitudinal magnetic field $B_\parallel$ of the cooler is an adiabatic invariant:

$$\frac{T_\perp}{B_\parallel} = \text{const}, \tag{9}$$

which is preserved, if the change of the magnetic field within a cyclotron wavelength $\lambda_c = 2\pi m v_\parallel / eB$ is very small compared to the total field:

$$\xi = \frac{\lambda_c}{B}\left|\frac{dB}{dz}\right| = \frac{\pi\sqrt{8mE_\parallel}}{eB^2}\left|\frac{dB}{dz}\right| \ll 1 \tag{10}$$

where $E_\parallel$ is the electron energy and m the electron mass. In the cooler an adiabatic expansion of the magnetic field by a factor of approximately 25 and a corresponding reduction of $T_\perp$ from 110 meV (cathode temperature ≈1000 °C to 4.4 meV was realized with adiabaticity parameter ξ less than 0.08 at a typical electron energy of $E_\parallel = 5$ keV. To reach an expansion factor of about 25 a heated cathode with a diameter of $\frac{3}{8}''$ is used [240]. The gun solenoid is operated at a magnetic field up to 12 kG with a smooth transition to the next solenoid having typically a field of 0.4 kG.

4.6.2 Cooling time of a multi-turn injected ion beam

Injected ion beams have high transverse velocities in the interaction section. Unfortunately, the transverse cooling force, unlike the longitudinal one, cannot be measured for well defined relative velocities, but only the development of the beam profile can be followed. In fact this overall cooling behavior of hot injected beams is of strong interest for experiments and accumulation. At the TSR, beams are injected by multi-turn injection with very large horizontal emittance, filling the horizontal acceptance $A_x \approx 100\ \pi$ mm mrad, which is about a factor of 3 larger than the vertical one. An empirical definition of a horizontal cooling time T_C, for the cooling of ion beams having large initial beam diameters, will be given in this section. Concerning the accumulation of ions, this cooling time T_C is of importance, besides the life-time of the ion beam. To determine T_C the time evolution of the horizontal beam profile right after injection was studied [241]. An example of such a measurement with $^{12}C^{6+}$ (73.3 MeV) is shown in Fig. 46, the electron density was $n_e = 1.53 \cdot 10^7\,\text{cm}^{-3}$, for the solenoid field a value of $B_{cool} = 209$ G was chosen, the expansion factor of the cooler was set to $\alpha = 7.7$. The width of the first profile is about $\sigma_x = 10.2$ mm. The whole covered time interval is 2 s. Particles having small betatron amplitudes are cooled faster, so at first a small peak grows over a rather broad distribution, distorting the initial Gaussian profile. This is caused by the ions interacting with a non-linear force. From such a measurement, the cooling time T_C is evaluated by fitting A Gaussian function to the cooled profile (Fig. 47), yielding σ_{cool}. The cooled region shall be defined as the range between $-6\sigma_{cool}$ and $+6\sigma_{cool}$. The number of counts outside this region is $N_{outside}(t)$. The time relevant for cooling, is the time, when most of the injected particles find themselves inside the cooled region. As the number of particles decreases with the lifetime T according to $N_{total} = N_0 \cdot e^{-t/T}$, the number $N_{outside}$ is normalized to N_{total}. The ratio $N_{outside}/N_{total}$ is drawn as a function of time in Fig. 48. The horizontal cooling time T_C is defined as the time

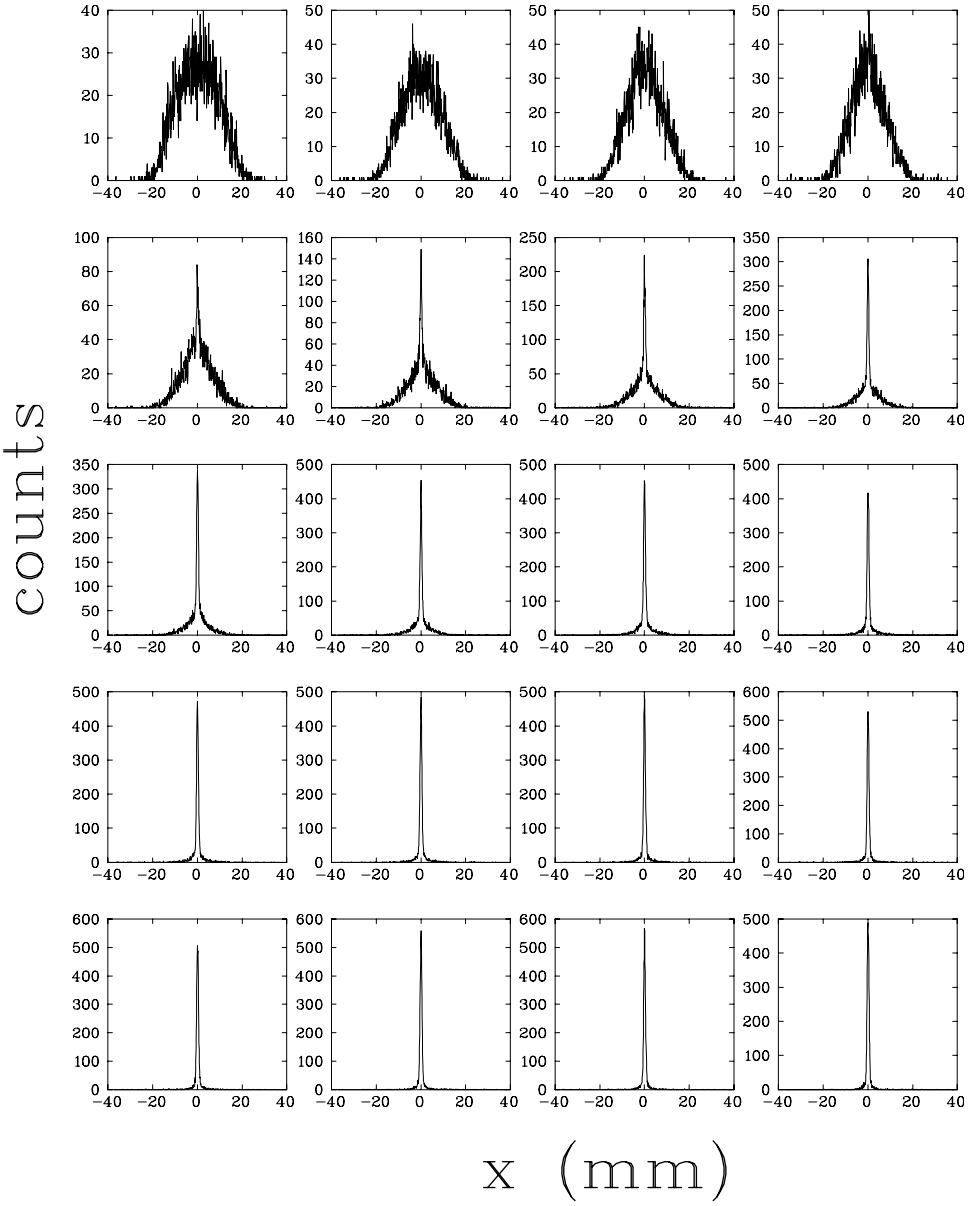

Fig. 46. Horizontal cooling time measurement with $^{12}C^{6+}$ (73.3 MeV) ($n_e = 1.53 \cdot 10^7\,\mathrm{cm}^{-3}$, $B_{cool} = 209\,\mathrm{G}$, expansion 7.7). The time evolution is in a row from left to right and from the top to the bottom. The time difference between two profiles is 0.1 s. The whole time interval covers 2 s.

when this ratio has reached 20% of its initial value. The measurement according to Fig. 46 yields $T_C = (1.15 \pm 0.04)\,\mathrm{s}$. The inverse of the cooling time T_C is called the horizontal cooling rate $1/T_C$.

The cooling time is shorter for beams with smaller width and the cooling rate thereby increases. In order to compare cooling times T_C, one has to make sure that the measurements were carried out for comparable forms and widths of the initial beam profiles.

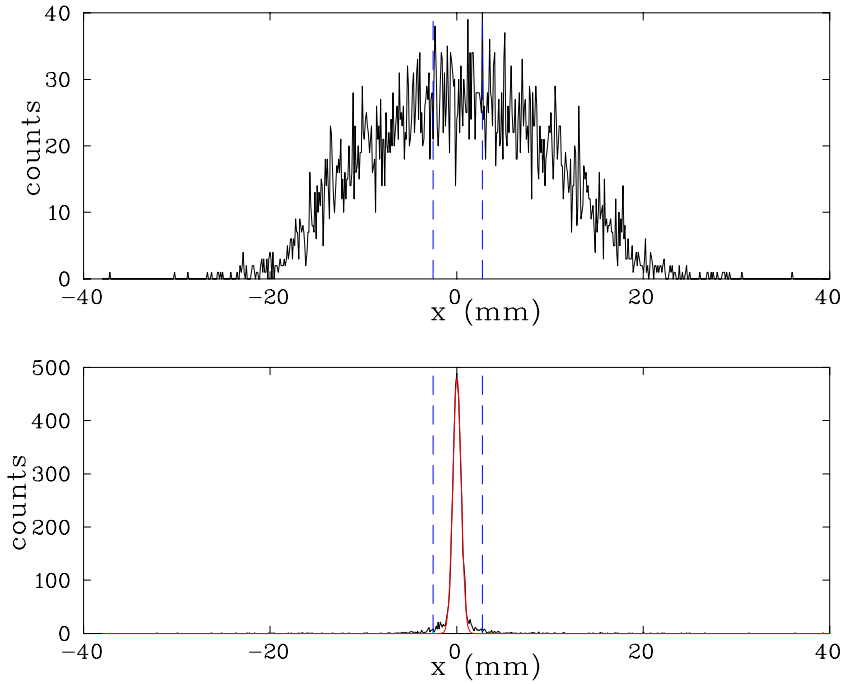

Fig. 47. Profile of injected and cooled beam for the cooling time measurement; to the latter a Gaussian function is fitted, the "cooled region" (definition see text) is marked by dashed lines. The time difference between both profiles is about 2 s.

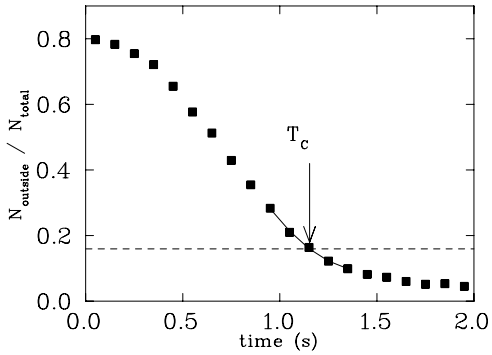

Fig. 48. Processed data according to the measurement shown in Fig. 47: The dashed line marks 20% of the initial value of $N_{outside}/N_{total}$ and the solid curve is a fitted polynome of second order in order to evaluate the horizontal cooling time T_C.

To investigate the dependence of the cooling time T_C on the ion velocity, measurements were carried out at the TSR for different atomic and molecular ions: HeH^+, $^{18}O^{2+}$, $^{28}Si^{2+}$, $^{14}N^{3+}$, $^{15}N^{3+}$, $^{12}C^{6+}$, $^{35}Cl^{6+}$, $^{32}S^{16+}$, and $^{80}Se^{23+}$. The velocities were in a range between 2.9 to 15.5% of the speed of light. Fitted Gaussians yield initial widths of (11.2 ± 3.8) mm at the position of the BPM. The normalized inverse cooling times $1/T_C$ are drawn in Fig. 49 as a function of the ion velocity $\beta = v/c$. The inverse cooling times $1/T_C$ are normalized by q^2/A (q-ion charge, A-ion mass) and to an electron density of $n_{e,0} = 10^8\,\mathrm{cm}^{-3}$. A function $\propto 1/\beta^2$ is fitted to the data (solid

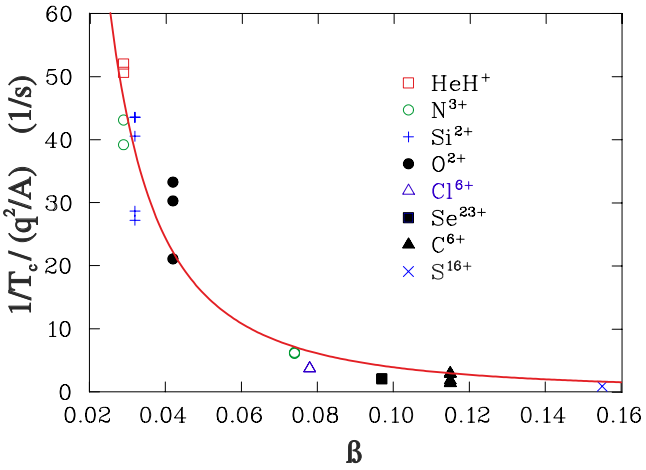

Fig. 49. Normalized inverse cooling time of a multi-turn injected ion beam as a function of the velocity $\beta = v/c$. $1/T_c$ is normalized to q^2/A and to an electron density $n_e = 10^8\,\mathrm{cm}^{-3}$. The red line is a $1/\beta^2$ fit [241].

red line in Fig. 49), describing the cooling rate $1/T_C$ at the TSR sufficiently well for velocities v_i/c within the range between 3 and 16% of the speed of light:

$$\frac{1}{T_C} = k \cdot \frac{n_e}{n_{e,0}} \frac{q^2}{A} \frac{1}{\beta^2}, \tag{11}$$

with $k = 3.9 \cdot 10^{-2}\ \mathrm{s}^{-1}$ and $n_{e,0} = 10^8\,\mathrm{cm}^{-3}$.

The electron density n_e can be calculated from the perveance μ of the electron gun ($\mu = 1\,\mu\,\mathrm{perv}$) and the cathode potential U_c:

$$I_e = \mu \cdot U_c^{3/2}. \tag{12}$$

Because the cathode potential in Eq. (12) is proportional to the square of the ion velocity: $U_c \sim \beta^2$ and the electron density scales with the velocity $I_e \sim n_e \cdot \beta$ it follows: $n_e \sim \beta^2$. Therefore the cooling time T_c becomes independent from the ion velocity and electron density:

$$T_C = k_1 \frac{A}{q^2}. \tag{13}$$

If an expansion factor $\alpha \approx 10$ is used then $k_1 \approx 3\,\mathrm{s}$. This means the cooling time for a multiturn injected proton beam in the velocity range between $0.03 < \beta < 0.16$ is about 3 s.

4.6.3 Equilibrium emittances and momentum spread

The equilibrium emittance and momentum spread of an electron cooled ion beam is determined by the electron cooling force and the intra-beam scattering, which is heating the stored ion beam. The measured equilibrium emittances $\epsilon_{x,y}$, defined by 1σ value of the spatial distribution, and the longitudinal momentum spread $\Delta p/p$ (Δp is the standard deviation of a Gaussian distribution) in the equilibrium between intrabeam scattering and electron cooling ($n_e = 8 \cdot 10^6\,\mathrm{cm}^{-3}$) are shown as function of the particle number in Fig. 50 [242]. The measurements have been done for D^+, $^6Li^{3+}$, $^{12}C^{6+}$, and $^{16}O^{8+}$ ion beams at a velocity of $\beta = 0.11$. For a given particle number,

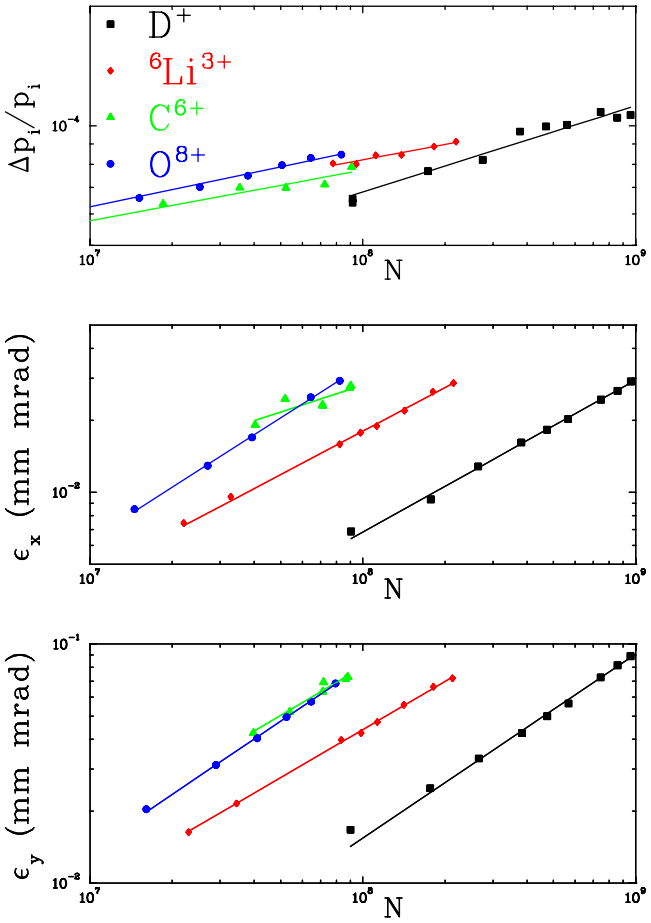

Fig. 50. Equilibrium emittances and momentum spread of cooled ion beams as function of the particle number for the ion species D^+, $^6Li^{3+}$, $^{12}C^{6+}$, and $^{16}O^{8+}$ ($n_e = 8 \cdot 10^6\,\mathrm{cm}^{-3}$, $B_{cool} = 418$ G, expansion 9.6).

Table 13. Exponents ξ resulting from fits $\propto N^{\xi}$ to the equilibrium emittances and the momentum spread.

	$\xi_{\parallel}$	ξ_x	ξ_y
D^+	0.22±0.02	0.64±0.01	0.77±0.02
$^6Li^{3+}$	0.13±0.01	0.60±0.01	0.67±0.01
$^{12}C^{6+}$	0.13±0.02	0.37±0.12	0.67±0.05
$^{16}O^{8+}$	0.15±0.01	0.73±0.01	0.77±0.01

emittances and momentum spread increase with increasing charge. Power laws $\propto N^{\xi}$ can be fitted to the measured emittances and momentum spreads. Simulations with the INTRABSC code gives $\xi_{x,y} = 0.42$ and $\xi_{\parallel} = 0.21$. The experimental exponents, resulting from fits to the data, are listed in Table 13. They are of the expected order, but $\xi_{\parallel}$ seems to be systematically lower than 0.21, and $\xi_{x,y}$ seems to be bigger than 0.42. As it is shown in Fig. 50 the momentum spread $\Delta p/p$ for the particle number $N = 10^8$ is about $7{\cdot}10^{-5}$. A reduction of the particle number by one order of magnitude would lead the reduction of the momentum spread to about $6 \cdot 10^{-5}$.

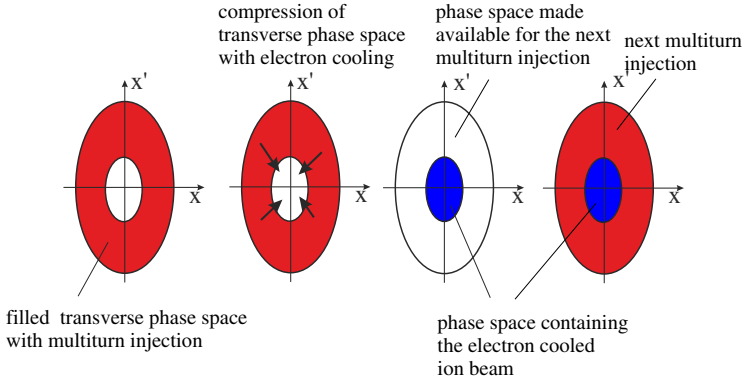

Fig. 51. Schematic description of the electron cooling stacking process.

4.7 Electron cooling stacking at the TSR

In order to accumulate ions in the heavy ion storage ring TSR the multi-turn injection is used. With the application of the multi-turn injection, the horizontal machine acceptance can be filled in typically 150 μs. In order to inject more particles, the already filled phase space must be emptied from particles, which can be accomplished by phase space compression with the electron cooling. To avoid collisions between the electron cooled ion beam and the septum foil the deflection angle of the bumper magnets has to be reduced compared to a normal multi-turn injection. Phase space needed for a new multi-turn injection can thus be made available (see Fig. 51).

When this process is repeated several times a large intensity multiplication factor is obtained [243]. This intensity multiplication factor is defined as the ratio of the stored to the injected ion beam current. With the use of this stacking method – called ECOOL stacking hereafter – the stored intensity I increases with time as:

$$\frac{dI}{dt} = n_r \cdot I_m - \frac{I}{\tau}, \tag{14}$$

where n_r is the repetition rate, I_m the effectively stored ion current of a multiturn injection and τ is the beam life-time. The solution of the differential Eq. (14) is:

$$I = I_0(1 - e^{-t/\tau}) \tag{15}$$

with:

$$I_0 = n_r I_m \tau. \tag{16}$$

The current I_m depends on the injector current I_e with: $I_m = M \cdot I_e$, where M is the intensity multiplication factor with multiturn injection. The total intensity multiplication factor $N = I_0/I_e$ is thus given by:

$$N = n_r M \tau. \tag{17}$$

In the following parameters important for ECOOL stacking will be discussed. In order to calculate the intensity multiplication factor N of ECOOL stacking, the lifetime of the ions must be known. The main processes affecting the lifetime of the stored ion beam are discussed in Sect. 4.8. The repetition rate n_r for the multi-turn injection depends on the time T_C for the electron cooling to clear the available phase space for the next multi-turn injection ($n_r = 1/T_C$). The time T_C can be estimated with formulae (13), giving for $^{32}S^{16+}$ ions an injection rate of approximate $3\,s^{-1}$, which

Table 14. Intensities for a few ions achieved with ECOOL stacking and comparison to the maximum possible intensities due to the incoherent tune shift.

Ion	Energy [MeV]	Life time [s]	Intensity [μA]	Stability limit [μA]
p	21	220000	1000	740
$^{16}O^{8+}$	98		750	1000
$^{12}C^{6+}$	73	1700	1000	1000
$^{32}S^{16+}$	195	450	1500	999
$^{35}Cl^{17+}$	293	318	1000	1130
$^{45}Sc^{18+}$	178		380	1087
$^{56}Fe^{22+}$	250	77	70	1151
$^{56}Fe^{23+}$	260	74	128	1114
$^{58}Ni^{25+}$	342	60	600	1147
$^{63}Cu^{25+}$	290	49	280	1150
$^{63}Cu^{26+}$	510	122	100	1326
$^{74}Ge^{28+}$	365	45	110	1234
$^{80}Se^{25+}$	480	204	100	1590
$^{80}Se^{31+}$	506	50	<1	1304
$^{197}Au^{50+}$	695	3	3	1651

is below the maximum possible injection rate of $5\,s^{-1}$ limited by the property of the bumper power supplies. An intensity multiplication factor M for the multi-turn injection as large as possible is desirable with electron cooling stacking. This factor depends on the phase space that is available for the multi-turn injections (see Fig. 51), which is smaller compared to a normal multi-turn injection, because some phase space is reserved for the electron cooled ion beam. If highly-charged ions are used, created in Heidelberg in three stripping processes, which take place in the tandem, after the tandem, and after the post acceleration, the injected ion beam has a much higher emittance than a typical tandem beam resulting in an intensity multiplication factor $M \leq 10$. Achieved intensities with electron cooling stacking are listed in Table 14. Up to mass numbers $A = 35$ intensities of about 1 mA could be reached. The measured total intensity multiplication factor N for $^{32}S^{16+}$ was about 4000.

4.7.1 Incoherent tune shift

The maximum possible number of stored ions N_i is determined by the maximum possible incoherent tune shift ΔQ given by:

$$N_i = \frac{A}{q^2}\frac{2\pi}{r_p} B\beta^2\gamma^3\epsilon(-\Delta Q), \tag{18}$$

where A is the ion mass number, q the ion charge, r_p the classical proton radius, B the bunching factor, β ion velocity in units of speed of light, γ the relativistic mass increase, and ϵ the beam emittance. The maximum possible incoherent tune shift for a coasting beam ($B = 1$) is $\Delta Q \approx -0.1$ at the TSR. From Eq. (18) a scaling law for the maximum possible intensity $I = qe_0N_if_0$ (f_0 – revolution frequency) can be

derived. The emittance scales as [244]:

$$\epsilon \sim \left(\frac{q^4}{A^2} \frac{N}{\lambda_{cool}} \frac{1}{\beta^3} \right)^{0.44} . \tag{19}$$

The cooling rate λ_{cool} in Eq. (19) is proportional to the electron density n_e:

$$\lambda_{cool} \sim n_e \frac{q^2}{A}. \tag{20}$$

As it was shown in Sect. 4.6.2 the electron density scales as: $n_e \sim \beta^2$. If expression (19) and (20) are inserted in Eq. (18) we obtain for the maximum possible stored ion intensity due to the incoherent tune shift the following scaling law:

$$I_{max} = \text{const} \cdot \frac{(A^{19} E^9)^{1/28}}{q}, \tag{21}$$

where the const can be calculated for example from the $^{12}C^{6+}$ data [235]. In Table 14 the achieved intensities during ECOOL stacking are compared with the maximum possible intensities due to the incoherent tune shift calculated with Eq. (21). As it is shown in Table 14 the stability limit I_{max} can be only reached up to ion masses of $A = 35$, because of the intensity limitation of the tandem post-accelerator combination for ion masses higher than $A = 35$.

4.8 The life time of stored ion beams

If the storage ring is operated at a stable working point the losses of the ions are primarily determined by interactions with the residual gas and the electrons in the electron cooler. For the interaction with the residual gas the following three processes have to be considered:

- single and multiple Coulomb scattering;
- electron capture;
- electron stripping.

Each of the above processes may become dominant under certain operation conditions of the TSR. The partial lifetime τ of the beam with respect to a certain process is given by $\tau^{-1} = \sigma \rho v$, where σ is the relevant cross section, ρ the density of the residual gas atoms of atomic charge number Z_{gas}, and v the ion velocity. Since all cross sections scale with powers of Z_{gas} between one and four, the concentration of heavier atoms in the residual gas is essential for the lifetime of the beam. After a bakeout of the storage ring to 250 °C, the residual gas is typically composed of 93% hydrogen and other molecules containing 2% carbon, 1% nitrogen, 6% oxygen and the heaviest component is 0.3% argon. Table 15 contains a compilation of measured lifetimes of stored ion beams with and without electron cooling together with theoretical lifetime estimations for Coulomb scattering (MS), stripping reactions (ST), electron capture in the residual gas (CAP) and in the electron cooler (REC). The lifetimes of molecules are determined by dissociation processes (DIS) in the residual gas and in the electron cooler. The longest lifetime of about 60 h was achieved for 21 MeV protons. This lifetime is determined by electron capture in the electron cooler. For singly-charged ions the lifetime is determined by the stripping reaction. The lifetime for highly-charged ions are limited by the electron capture processes in the residual gas and in the electron cooler. The heaviest ion stored so far was $^{197}Au^{50+}$. With $^{197}Au^{50+}$ ions

Table 15. Experimental and theoretical lifetimes of ion beams in the TSR.

			Experiment		Theory			
Ion	Energy	Pressure	Cooled	Uncooled	Cooled	Expl.	Uncooled	Expl.
	[MeV]	[10^{-11} mbar]	[s]	[s]	[s]		[s]	
p	21	4	220000		180000	REC		
HD^+	2	7		5				DIS
$^{7}Li^{+}$	13	6		48	41	ST	41	ST
$^{9}Be^{+}$	7	6	16	16	12	ST	12	ST
$^{12}C^{6+}$	73	6	7470		5519	REC	5630	MS
$^{28}Si^{14+}$	115	6	540	260	424	CAP	493	CAP
$^{32}S^{16+}$	196	5	450		554	REC	1200	CAP
$^{35}Cl^{15+}$	157	6	366		306	CAP	375	CAP
$^{35}Cl^{17+}$	202	6	318	366	402	REC	735	CAP
$^{56}Fe^{22+}$	250	5	77		90	REC	278	CAP
$^{58}Ni^{25+}$	342	5	60		89	REC	374	CAP
$^{63}Cu^{26+}$	510	6	122		166	REC	622	CAP
$^{74}Ge^{28+}$	365	5	45		59	REC	162	CAP
$^{80}Se^{25+}$	480	5	204		179	REC	384	CAP
$^{197}Au^{50+}$	710	5	3					

a storage lifetime of only 3 s was measured with the magnetically expanded electron beam in the cooler at a density of $n_e \approx 10^7\,\mathrm{cm}^{-3}$. This short storage time is a consequence of the highest recombination rate coefficient ever observed with an atomic ion. At about 30 meV a huge dielectric recombination resonance was observed [245]. Such resonances occurring at near zero relative energy between electrons and ions lead to the enhanced recombination rate observed in $^{197}Au^{50+}$ ions. The lifetime of $^{12}C^{6+}$ without electron cooling is given by multiple scattering in the residual gas. This small-angle scattering process and, in particular, the influence of the storage ring acceptance has been treated by Hardt [246]. Introducing a maximum acceptance angle Θ_{max} of the ring, the e^{-1} time τ_{ms} for losses due to multiple scattering is for a round vacuum chamber given by:

$$\tau_{ms} = \frac{\Theta_{max}^2}{3.67 d\overline{\Theta^2}/dt}. \tag{22}$$

The time derivation of the projected mean square angle $\overline{\Theta^2}$ of multiple scattering is given in textbooks [247] and we obtain for a single residual gas component:

$$\tau_{ms} = \frac{\Theta_{max}^2 v^3}{\pi\rho(q/A)^2 Z_{gas}^2 r_p^2 c^4 \ln(\Theta_{max}/\Theta_{min}) 14.67}. \tag{23}$$

Here v is the velocity of the ions with charge state q and mass number A, ρ the density of the residual gas atoms, r_p the classical proton radius and c the velocity of light, while Θ_{min} is given [247] by:

$$\Theta_{min} = \frac{2.84 \cdot 10^{-6} Z_{gas}^{1/3}}{A(v/c)\gamma}. \tag{24}$$

The measured lifetimes are reproduced if a value of the maximum acceptance angle is $\Theta_{max} = 2\,\mathrm{mrad}$. When the emittance growth is compensated by electron cooling, the losses due to multiple Coulomb scattering can be neglected. Then, for fully-ionized ions two processes compete:

(1) *Single scattering* by an angle larger than Θ_{max} resulting in an effective lifetime τ_{ss}:

$$\tau_{ss} = \frac{1}{\rho v \int \sigma_{Ruth} d\Omega} = \frac{\Theta_{max}^2 v^3}{4\pi\rho(q/A)^2 Z_{gas}^2 r_p^2 c^4}. \tag{25}$$

From Eqs. (23) and (25) follows:

$$\tau_{ss} = \tau_{ms} \ln\left(\frac{\Theta_{max}}{\Theta_{min}}\right) 3.67 = 20.5\tau_{ms}. \tag{26}$$

Therefore the single scattering lifetimes are approximately one order of magnitude higher than the multiple scattering lifetimes τ_{ms}.

(2) *The ions losses due to electron capture.* Schlachter et al. [218] have determined an universal scaling rule for electron capture rates for all ions. They introduced a reduced cross section $\tilde{\sigma} = \sigma Z_{gas}^{1.8}/q^{0.5}$ and a reduced energy per nucleon $\tilde{E} = E/(Z_{gas}^{1.25} q^{0.7})$, where the projectile energy is given in kev/A and σ is the cross section in cm^2. They determined the following relation for the reduced cross section:

$$\tilde{\sigma} = \frac{1.1 \cdot 10^{-8}}{\tilde{E}^{4.8}} (1 - e^{-0.037\tilde{E}^{2.2}})(1 - e^{-2.44\cdot 10^{-5}\tilde{E}^{2.6}}). \tag{27}$$

At the TSR energies the terms in brackets can be neglected in most cases and we can write:

$$\sigma = 1.1 \cdot 10^{-8} \frac{q^{3.9} Z_{gas}^{4.2}}{E^{4.8}}. \tag{28}$$

For our residual gas composition the strong $Z_{gas}^{4.2}$ dependence of the cross section leads to a dominance of the C, N, O fraction. According to Eq. (28) the lifetime due to the electron capture in the residual gas is much stronger energy dependent than the lifetime of single- and multiple-scattering processes. In Fig. 52 the measured lifetime of a $^{12}C^{6+}$ ion beam between 10 and 74 MeV, without electron cooling, is shown [235]. The dashed brown curve indicates the calculated lifetimes due to multiple scattering processes, whereas the red dashed curve represents lifetimes due to the electron capture. Both curves are calculated for $p = 7 \cdot 10^{-11}$ mbar. The total lifetime of these two processes is displayed with a solid red line. As it is indicated in Fig. 52, multiple scattering dominates at higher energies around 70 MeV and at low energies around 10 MeV electron capture is the determining process on the lifetime.

Beside electron capture in the residual gas, one also expects contributions from the recombination with free electrons in the electron cooler through mechanisms such as radiative or dielectronic recombination. The lifetime τ_{rec} due to radiative recombination in the electron cooler is given by:

$$\frac{1}{\tau_{rec}} = n_e (l_{eff}/C_0) \alpha_{rec}, \tag{29}$$

where α_{rec} is the recombination coefficient, l_{eff} the effective length of the cooler (TSR: $l_{eff} = 1.2\,\mathrm{m}$), C_0 the circumference of the storage ring, and n_e the electron

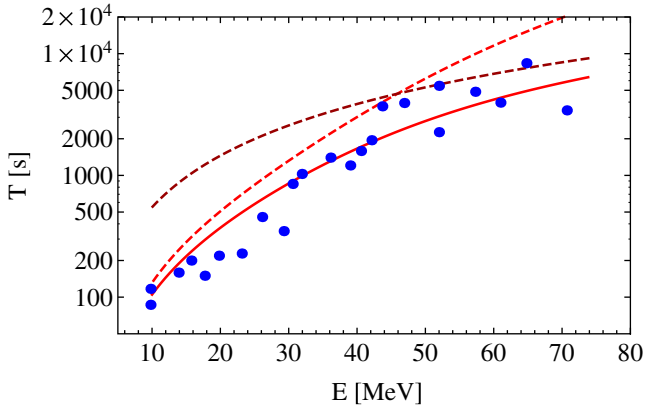

Fig. 52. Measured lifetime of a $^{12}C^{6+}$ beam at different energies. The brown dashed line shows the calculated lifetimes taking into account multiple scattering, whereas the red dashed line represents the lifetimes due to electron capture. The red solid line shows the total lifetimes calculated for $p = 7 \cdot 10^{-11}$ mbar.

density. The recombination coefficient α_{rec} has been derived in ref. [248]:

$$\alpha_{rec} = 3.02 \cdot 10^{-13} \frac{q^2}{\sqrt{kT_\perp}} \left(\ln\left(\frac{11.32q}{\sqrt{kT_\perp}}\right) + 0.14 \left(\frac{kT_\perp}{Z^2}\right)^{1/3} \right), \tag{30}$$

with $kT_\perp$ in eV and α_{rec} in cm^3/s.

For the electron stripping from one-electron ions reliable theoretical as well as experimental results exist. Theoretical treatments of stripping reactions are mostly based on classical models [249] or on the Born approximation. In the classical model one considers the energy transfer to the electron as a result of its scattering by an atomic nucleus of charge Z_{gas} and Z_{gas} individual electrons of this atom. The stripping cross sections [7,249] for ion velocities large compared to the velocity of the ionic electron ($v > Zv_0$) are calculated separately for light and heavy targets, which in our case translates into heavy and light projectile:

(1) Heavy projectile: $Z \geq Z_{gas}$

$$\sigma_{sh} = 4\pi a_0^2 \left(\frac{v_0}{v}\right)^2 (Z_{gas}^2 + Z_{gas}) \frac{I_0}{I}, \tag{31}$$

where a_0 is the radius of the first Bohr orbit, $v_0 = \alpha c$, I is the binding energy of the electron and $I_0 = 13.6\,\text{eV}$.

(2) Light projectile: $Z \leq Z_{gas}^{1/3}$:

$$\sigma_{sl} = \pi a_0^2 Z_{gas}^{2/3} \frac{v_0}{v} \cdot \sqrt{\frac{I_0}{I}}. \tag{32}$$

Here it is taken into account that the firmly bound inner electrons of the target no longer act independently but screen the nuclear charge. The stripping cross section for ions with several electrons can be calculated approximately by summing over the contributions of the k individual electrons of the projectile:

(1) Heavy projectile:

$$\sigma_{sh}(k) = 4\pi a_0^2 \left(\frac{v_0}{v}\right)^2 (Z_{gas}^2 + Z_{gas}) \sum_{i=1}^{k} \frac{I_0}{I_i}. \tag{33}$$

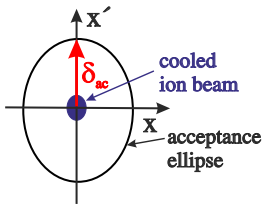

Fig. 53. Electron cooled ion beam inside the acceptance ellipse at the target location. δ_{ac} is the maximum possible scattering angle in the gas target which does not lead to the loss of the ion.

(2) Light projectile:

$$\sigma_{sl}(k) = \pi a_0^2 Z_{gas}^{2/3} \frac{v_0}{v} \cdot \sum_{i=1}^{k} \sqrt{\frac{I_0}{I_i}}. \tag{34}$$

In Table 15 the lifetimes of singly-charged ions were calculated using Eqs. (33) and (34). Thus, when the uncertainties in the residual gas pressure are taken into account it is indeed possible to understand the measured lifetimes from the calculated partial lifetimes.

4.8.1 Ion interaction with an internal gas target

Experiments devoted to nuclear structure investigations through inelastic scattering and transfer reactions demand an internal gas target with a target thickness of up to $5 \cdot 10^{13}$ atoms/cm^2 or even higher (see e.g. Sect. 2.7.2). In this section the ion lifetime due to the interaction with the internal gas target is discussed. For these interactions we have to consider Coulomb scattering, electron capture as well as stripping reactions. The cross sections for stripping and electron capture have been already discussed in Sect. 4.8. With these individual cross sections σ the particular lifetimes τ of the different loss mechanisms can be calculated:

$$\tau = \frac{1}{\sigma \cdot n_t \cdot f_0}, \tag{35}$$

where f_0 is the revolution frequency and n_t the target thickness: $n_t = \int n \cdot ds$, depending on the gas density n.

4.8.2 Coulomb scattering in the target

The particle losses due to the single scattering are explained in Fig. 53. To compensate the energy loss and multiple scattering in the target, leading to an emittance growth, electron cooling is required which reduces the emittance of the ion beam. The transversal phase space occupied by the cold ion beam is sketched in Fig. 53 by an upright ellipse. Coulomb scattering in the target leads to an increase of the slope x' of the particle orbit. If the maximum possible scattering angle δ_{ac} reaches the acceptance ellipse of the storage ring the ion will be lost. Coulomb scattering is described by the Rutherford formula. In the center of mass system the differential cross section is given:

$$\frac{d\sigma}{d\Omega} = \frac{1}{4} \left(\frac{Z_t q e^2}{4\pi\epsilon_0 2E_s} \right)^2 \frac{1}{\sin^4(\Theta/2)}, \tag{36}$$

where ϵ_0 is the permittivity, Z_t is the charge of the atomic nucleus of the target, e is the elementary charge, E_s is the energy in the center of mass system (CMS) and Θ is the scattering angle in the CMS system. The cross section σ_{sc} for the particle loss due to Rutherford scattering can be calculated from Eq. (36):

$$\sigma_{sc} = \int_{\varphi_{ac}}^{\pi} \frac{d\sigma}{d\Omega} 2\pi \sin(\Theta) d\Theta = \frac{e^4 Z_t^2 q^2}{64\pi\epsilon_0^2 E_s^2} \cot^2\left(\frac{\varphi_{ac}}{2}\right), \tag{37}$$

where φ_{ac} is the acceptance angle in the center of mass system. The relation between φ_{ac} and δ_{ac}, depending on the ion mass m and target atom mass m_t, is given by:

$$\tan(\delta_{ac}) = \frac{\sin(\varphi_{ac})}{\cos(\varphi_{ac}) + \frac{m}{m_t}}. \tag{38}$$

In order to obtain longer lifetimes, the acceptance angle δ_{ac} should be as large as possible. The acceptance angle is determined by the horizontal β_x and vertical β_y beta functions and by the horizontal A_x and vertical A_y acceptances of the storage ring. Since both β_i functions and acceptances A_i, with $i = x, y$ are not the same, there are two different acceptance angles $\delta_{ac,i}$:

$$\delta_{ac,i} = \sqrt{\frac{A_i}{\beta_i}}. \tag{39}$$

Thus, in order to obtain long single scattering lifetimes, a preferred target location shall be at a place where the β functions are small. The β functions of the storage ring in the standard mode are displayed in Fig. 34. Due to the requirement of a small horizontal and vertical β functions at the target location, the target should be located at $s = 0\,\text{m}$, compare Fig. 34. In the present TSR ring the straight section around $s \approx 0\,\text{m}$ is occupied by the rf-system and the diagnostics tools. But it is easily possible to replace the straight section for the diagnostics and rf-system with the experimental straight section, where the gas target would be built in. After this change the horizontal β_x function at the target location would be $\beta_x = 3.3\,\text{m}$ and the vertical $\beta_y = 1\,m$. With the horizontal acceptance of the storage ring $A_x \approx 100\,\text{mm mrad}$ and the vertical one of $A_y \approx 40\,\text{mm mrad}$, a horizontal acceptance angle of $\delta_{ac,x} \approx 5.5\,\text{mrad}$ and a vertical one of $\delta_{ac,y} \approx 6.3\,\text{mrad}$ can be estimated. Since both acceptance angles are similar, we can assume for our further calculations of the single scattering lifetimes an average acceptance angle of $\delta_{ac} = 5\,\text{mrad}$. In Table 16 the lifetimes due to single scattering τ_{sc} in different targets are summarized. For the target thickness a value of $5 \cdot 10^{13}$ atoms/cm^2 is assumed. Also shown in Table 16 are the particle lifetimes τ_{cap} due to electron capture processes in the target. These lifetimes are calculated with the well known Schlachter formulae (27). As shown in Table 16 the lifetimes for bare ions are determined by electron capture. Especially for bare light ion species and H_2 targets the lifetimes are affected by multiple scattering. As it is pointed out in Table 16, experiments up to a target thickness of $5 \cdot 10^{13}$ atoms/cm^2 should be possible at the TSR, if H_2 or He targets are used. In 1992 the TSR was equipped with a internal gas target with a target thickness of $5.6 \cdot 10^{13}$ atoms/cm^2. Details of this target are summarized in the next section.

4.8.3 The FILTEX experiment

An internal polarized hydrogen gas target was installed in the TSR to test a new method to polarize beams of strongly interacting particles. The stored particles, here

Table 16. Calculated ion lifetimes due to interaction with different internal targets. A target thickness of $5 \cdot 10^{13}$ atoms/cm^2 was assumed. τ_{sc} is the particle life time for single scattering and τ_{cap} is the lifetime for electron capture.

Ion	Energy [MeV]	target	τ_{sc} [s]	τ_{cap} [s]
$^{12}C^{6+}$	73	H_2	1847	4340
$^{12}C^{6+}$	73	He	461	236
$^{12}C^{6+}$	73	N_2	38	1.2
$^{12}C^{6+}$	73	Ar	6	0.055
$^{35}Cl^{17+}$	293	H_2	3200	302
$^{35}Cl^{17+}$	293	He	790	16
$^{35}Cl^{17+}$	293	N_2	64	0.086
$^{35}Cl^{17+}$	293	Ar	10	0.0095

protons, pass a polarized hydrogen gas target (thickness $6 \cdot 10^{13}$**H**/cm^2) in the ring some 10^{10} times and become partially polarized because one spin state is attenuated faster than the other [250]. The method is of particular interest for the production of polarized antiprotons, for which the construction of polarized ion sources is not feasible. We now discuss the internal polarized gas target which is required for the spin filter method. In principle, a hydrogen polarized gas target can be produced by use of a jet of polarized atoms from an atomic beam source. However, the target thickness provided by such a jet is only about $2 \cdot 10^{11}$ **H** atoms/cm^2. A test of the spin filter method required an increase in the target thickness of the polarized **H** target by a factor of several hundred. This was accomplished by injecting the polarized atoms into a windowless T-shape storage cell, through which the circulating beam passes. The polarized atoms make some hundred wall collisions before they exit from one of the ends of the tube. Depolarization of the atoms in wall collisions is suppressed by coating the cell walls with a suitable coating. The polarized target was located in the center of the experimental straight section. Electron cooling was applied continuously in order to compensate the energy loss and the emittance growth caused by the target. The polarized hydrogen target was provided by atoms from an atomic beam source, which were injected into a thin-walled 250 mm long aluminium tube of 11 mm inner diameter. The small diameter of this aluminium tube determined the acceptance of the storage ring. To minimize the losses of particles from Coulomb scattering in the target the TSR was operated in the low beta mode. The target cell was cooled to 100 K in order to increase the target thickness n = $(5.6 \pm 0.3 \cdot 10^{13})$ **H**/cm^2 for atoms in a single hyperfine state. The target thickness was deduced from the measured pp count rate using the known circulating beam current, pp cross section and the detector geometry. An alternative method to determine the target thickness was to measure the energy loss in the target after switching off the electron cooler. The energy loss was determined with the Schottky noise analysis by measuring the decrease of the revolution frequency of the stored ion beam. A powerful differential pumping system prevented the target gas from entering the other parts of the storage ring. The target polarization was determined in separate measurements at the beginning and at the end of the experiment, in which a 27 MeV beam of α particles was stored in the ring instead of protons. The target polarization was determined from the left-right asymmetry of recoil protons detected at $\Theta_{lab} = 21°$. The magnitude of the target polarization was found to be $P_T = 0.83 \pm 0.03$. The FILTEX experiment was carried out as follows. An (unpolarized) 23 MeV proton beam of up to 1 mA was stored in the ring by using the ECOOL stacking. Subsequently the beam was left to circulate for

periods between 30 und 90 min. After 90 min the beam intensity had decreased to 5% of the initial value, so that longer filter times could not explored. The polarization of the remaining beam was subsequently detected by making use of the large difference in the pp elastic scattering cross section between parallel and antiparallel spins. For this purpose the direction of the 5 G guide field, which determines the direction of the target polarization (up or down), was reversed periodically and the pp elastic count rates for the two target orientations were compared. Scattered protons were detected in scintillation counter telescopes, located at $\Theta_{lab} = 33.3°$ above and below the plane of the storage ring. The beam polarization is determined by the sum of the number of counts registered in the two detectors for target spin up and target spin down. This measurements results in a polarization buildup of $(1.24 \pm 0.06) \cdot 10^{-2}$ h^{-1}. At the used target density of n = $(5.6 \pm 0.3 \cdot 10^{13})$ **H**/cm^2 a lifetime of the 23 MeV proton beam of 30 min was measured and for the α beam a lifetime of about 15 min was determined. These lifetimes can be explained by single scattering in the target, where the scattering angle is larger than the acceptance angle of the storage ring. Because the small diameter $d = 11$ mm of the target cell determines the acceptance of the storage ring, the maximum acceptance angle in the target location is given by: $\delta_{ac} = d/2\beta$, where β is the β function at the target position. In the low beta mode the horizontal β_x and vertical β_y function were: $\beta \approx \beta_x \approx \beta_y \approx 1$ m [251], resulting in an acceptance angle of: $\delta_{ac} \approx 5.5$ mrad. The lifetimes due to single scattering can be calculated with the Eqs. (35,37–39). For the 23 MeV proton beam we obtain 60 min and for the 27 MeV α beam a lifetime of 38 min can be calculated. Both estimated lifetimes for the p and α beams are about a factor of two longer than the measured ones. A reason for the somewhat shorter measured lifetimes is the beam width of the electron cooled ion beam, which was neglected in the calculations, leading to a smaller effective acceptance angle (compare Fig. 53) and thus a shorter lifetime. Electron capture processes for both beams can be neglected, because the calculated electron capture lifetime for 23 MeV protons is $\tau_{cap} = 37$ years and for the 27 MeV α beam $\tau_{cap} = 4.8$ days.

4.9 The rf resonator of the TSR

The magnetic rigidity of the storage ring can cover the range between 0.2–1.5 Tm. In order to obtain heavy ions corresponding to this range of magnetic rigidities a new type of ferrite loaded resonator was developed [252] at MPIK which is able to accelerate or decelerate heavy ion beams covering a frequency range between 0.45 and 9 MHz with a fast tuning capability of about 9:1. The resonance frequency variation is realized by changing the ferrite permeability with a d.c. magnetization field. Most of the existing resonators have a simple coaxial quaterwave geometry. The magnetization field is produced by several bias windings mounted directly on the ferrite rings and connected to a regulated power supply able to deliver currents of several hundreds to 1000 A. The variation of the d.c. bias changes the incremental permeability $\mu_\triangle$ and in this way the resonator frequency is changed. The inside construction of these resonators is complicated by the necessary ferrite rings support and the bias windings which reduce the ferrite volume. Also, the rf voltage induced in the bias windings requires supplementary rf-filters which may lead to some parasitic resonances. In order to avoid this complications a new type of ferrite loaded resonator was developed at MPIK [253]. In contrast to the common resonators an external quadrupole field is used to magnetize the ferrite. Therefore the magnetization and rf field are completly decoupled at this kind of resonator. Figure 54 shows the resonator. Clearly to see is the green quadrupole with the four magnetization windings. The overall length of the resonator is about 1 m. Figure 55 shows the scheme of the resonator.

Fig. 54. The quadrupole ferrite loaded resonator.

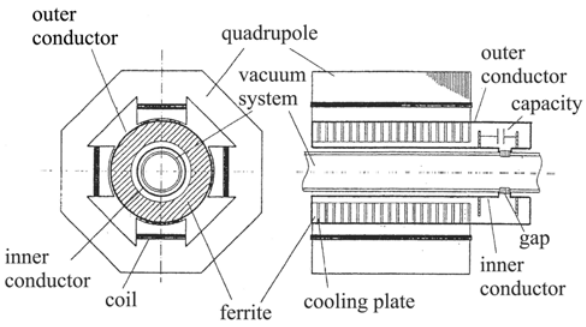

Fig. 55. Schematic drawing of the ferrite loaded resonator.

The space between the inner and the outer conductor of the resonator is filled with ferrite rings and copper cooling plates. From electrical strength considerations a clearance (radial dimension −10 mm) is needed between the inner conductor and the copper cooling plates. The magnetic bias field is created by an external quadrupole with 5 bias windings on each pole. In order to reduce the necessary d.c. power the space between the ferrite rings and the quadrupole poles must be as small as possible. The voltage necessary for acceleration or deceleration of a multi-turn injected ion beam is with 100–300 V relatively small and causes no problem. The design criteria of the maximum voltage of 5 kV was the demand of adiabatic capture of an rf-stacked ion beam having a momentum spread of about 1%. The properties of the rf-system are summarized in Table 17.

4.9.1 Rf acceleration

The widely tuneable range of the TSR resonator opens up the possibility to accelerate and decelerate ions. Experiments have shown the feasibility of acceleration and deceleration. For ramping the magnetic fields DAC cards developed at MPIK as well a DSP driven synthesizer card have been used. The generated functions to ramp the magnets can be directly calculated from the rigidity, taking into account the measured saturation effects of the TSR magnets. The user front end used for the ramp

Table 17. Properties of the ferrite loaded resonator with external quadrupole field.

frequency range	0.5–9 MHz
fast frequency shift	factor 5.5
max. rf voltage	5 kV
max. rf power	10 kW
rf power density (ferrite)	150 mW/cm^3
ferrite material	Philips FXC 8C12
ferrite dimensions	$498 \times 270 \times 25$ mm^3
number of ferrite rings	20
cooling	21 water cooled copper disks
bias current	up to 150 A

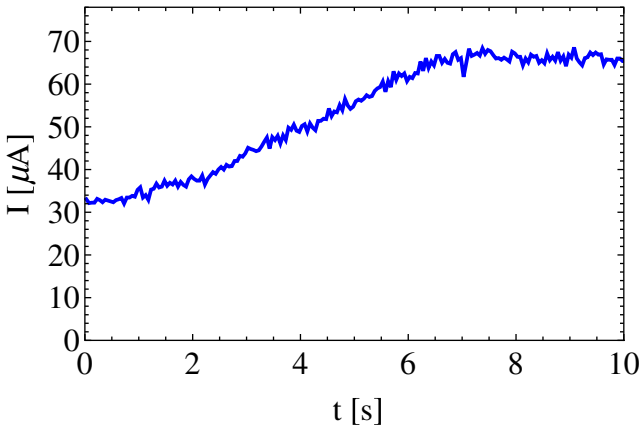

Fig. 56. Ion current during acceleration of $^{12}C^{6+}$ ions from 73.3 MeV to 362 MeV. After 7 s the maximum rigidity of 1.57 Tm was reached.

calculation is written in Mathematica. Only with the calculated functions for the power-supply currents and the calculated rf frequency it was possibly to accelerate a $^{12}C^{6+}$ beam from 73.3 MeV to 362 MeV. The measured ion current during this acceleration process is shown in Fig. 56. The ion current increases as the revolution frequency is increased during the ramp. From the final rf frequency and the stored ion current at the final energy an efficiency of 98% [254] for the acceleration process can be calculated. The efficiency is the ratio of the ion number reaching the final energy to the injected ion number. In these tests a record magnetic rigidity for an ion beam in the TSR of 1.57 Tm was achieved, significantly above the rigidity of 1.4 Tm realized in any previous beam time. The ramping time of 7 s in the present case was limited by the voltage induced in the correction windings on the iron cores of the TSR main magnets, which had to be kept below 6 V for proper operation of the power supplies that are presently in use. The high efficiency was achieved by pre-cooling the ion beam with the electron cooler before starting the ramp.

4.9.2 Mass selective acceleration

Acceleration of molecular ions has been applied in experiments bringing, among others, D_3O^+ beams from 2 MeV at injection to final energies of 4.2 MeV within 2.5 s. Singly charged molecules are produced in a Penning ion source located at the 2 MV terminal of the Pelletron. Besides heavy singly-charged molecules, like $DCND^+$, the

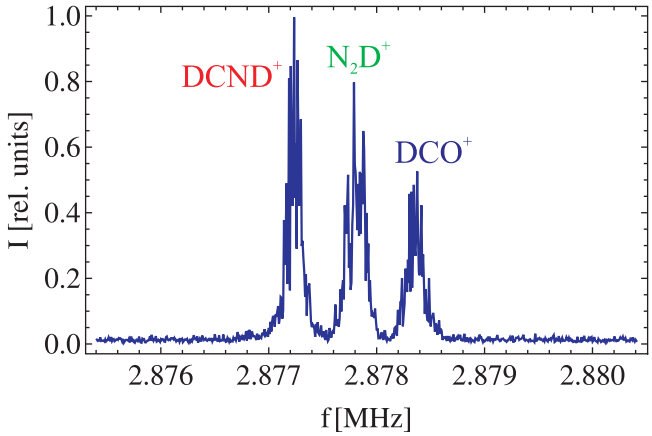

Fig. 57. Measured Schottky spectrum of a molecular ion beam, consisting of three ion species with the mass of 30 u.

ion source produces several other ion species such as N_2D^+, DCO^+, etc., with equal masses of 30 u. Due to the fact that the relative mass difference of two neighboring ion species, like $DCND^+$ and N_2D^+, is only $\Delta m/m = 3.7 \cdot 10^{-4}$, the desired molecule ions ($DCND^+$) can neither be separated with the separation dipole of the ion source nor with the magnets of the transfer line guiding the ion beam to the TSR ring. The Schottky spectrum of the injected molecular ion beams, taken at the 44^{th} harmonic of the revolution frequency, is shown in Fig. 57. The peaks in the spectrum correspond to the different ion species. Because the energy of each ion type is the same, given by Pelletron voltage and the ion charge, the frequency splitting $\Delta f/f$ can be calculated in the non-relativistic approach by the following formula: $\Delta f/f = -\frac{1}{2}(1+\alpha)\Delta m/m$, where α is the momentum compaction factor of the storage ring, describing the change of the closed C_0 orbit length by variation the momentum p of the ions:

$$\alpha = \frac{\Delta C_0/C_0}{\Delta p/p}.$$

In the standard mode of the TSR the momentum compaction factor $\alpha = 0.1$ which results in a frequency splitting of 581 Hz at $f = 2.878$ MHz, shown in Fig. 57. The width of each peak in the spectrum is determined by the momentum spread ($\sigma_p/p \approx 3 \cdot 10^{-5}$) of the injected beam, which is quite small, yielding in a clear separation of the mass peaks. With the mass selective acceleration [254] the desired ion species, for example $DCND^+$, can be separated from the other type of ions. The procedure is explained in Fig. 58. Mass selective acceleration can be described in the longitudinal phase space, defined by the frequency deviation $\Delta f_0 = f_0 - f_s$ and phase deviation $\Delta\phi = \phi - \phi_s$ of an ion, with a revolution frequency f_0 and rf phase ϕ. The revolution frequency of the synchronous particle is given by f_s and its rf phase is ϕ_s. After multiturn injection, which takes place at a resonator voltage of $U = 0$ V, three frequency bands are formed in the phase space (Fig. 58a). The width of each frequency band is given by the measured momentum spread of the injected beam. After injection the resonator voltage was increased linearly in 1.5 ms to $U = 10$ V, capturing the stored ion beam into the rf bucket, enclosed by the separatrix (compare Fig. 58b). To accelerate the ions, the synchronous phase was increased from 0° to 1°. In the calculation a time of 200 ms was used to simulate the shift of the synchronous phase. In the experiment the same shift was carried out in 0.5 s, by changing the derivative of the rf frequency df/dt from 0 to 0.45 MHz/s, following the magnetic rigidity $B\rho$ of the

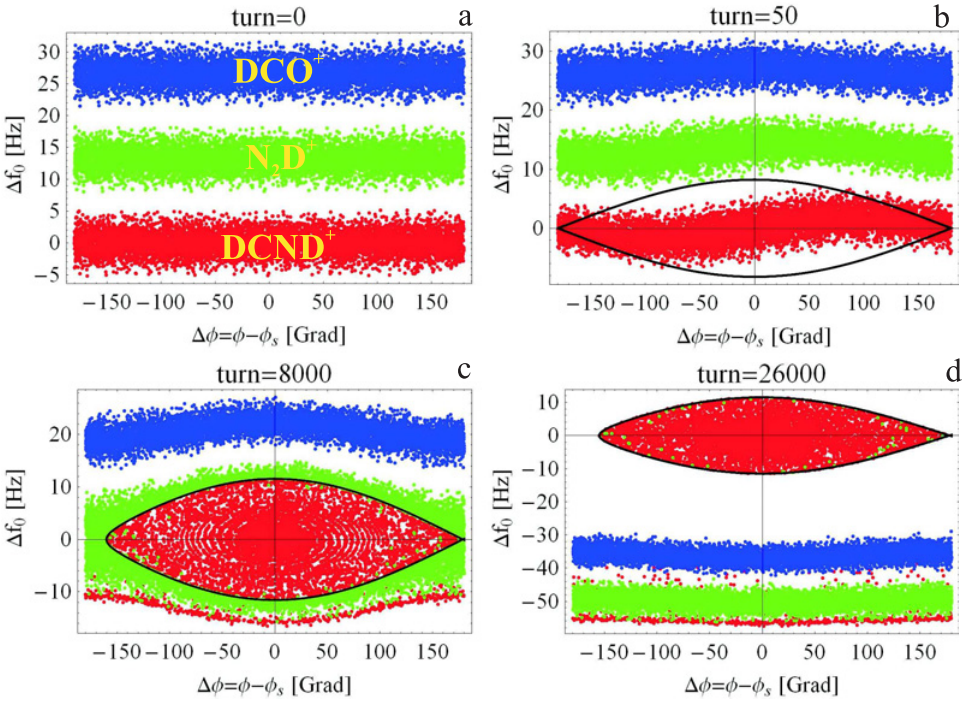

Fig. 58. Illustration of mass selective acceleration in the longitudinal phase space. The size of the separatrix given by the resonator voltage and synchronous phase is shown as a black curve.

$DCND^+$ ion beam. The longitudinal phase space during the synchronous phase shift is displayed in Fig. 58c. At turn = 26000 displayed in Fig. 58d the synchrotron phase is already 1°. The ions outside the bucket, created in the bunching process (Fig. 58b), taking place during the first 1.5 ms, are not accelerated and keep their energy. In Fig. 58c the rf bucket, filled with $DCND^+$ ions, moves through the N_2D^+ ion beam without capturing a N_2D^+ ion. There are only a few N_2D^+ ions inside the $DCND^+$ bucket, caused by the bunching process taking place in the first 1.5 ms. To avoid a trapping of any undesired ions, the resonator voltage has to be slightly decreased. Due to the small energy spread of the injected ion beam a reduction of the resonator voltage is possible. However, a small energy drift of the Pelletron will cause an energy error that cannot be balanced by the bucket size if the resonator voltage is decreased. In Fig. 58c, and d it can be seen that some $DCND^+$ ions are not captured in the bucket, because the resonator voltage was increased too fast. For that low ion beam velocity $\beta = 0.012$ a slower voltage increase ($\geq$5 ms instead of 1.5 ms) would be more adequate. During the acceleration process the energy difference of the ion bucket to the non accelerated undesired ions is increasing with time. Since the magnetic field of the storage ring is matched to the $DCND^+$ ions, the false ions will hit the vacuum chamber of the storage ring during the acceleration process, due to the limited momentum acceptance of the storage ring. After 2 s acceleration time a pure $DCND^+$ ion beam reaches the final energy of $E = 3$ MeV. At this energy the neutral reaction products from collisions of $DCND^+$ with residual gas (mostly H_2) were observed using a finely segmented, energy-sensitive surface barrier detector. These collisions lead to dissociation into neutral and charged or only neutral fragments. The corresponding pulse height spectrum is shown in Fig. 59. Changing the rf start frequency to an

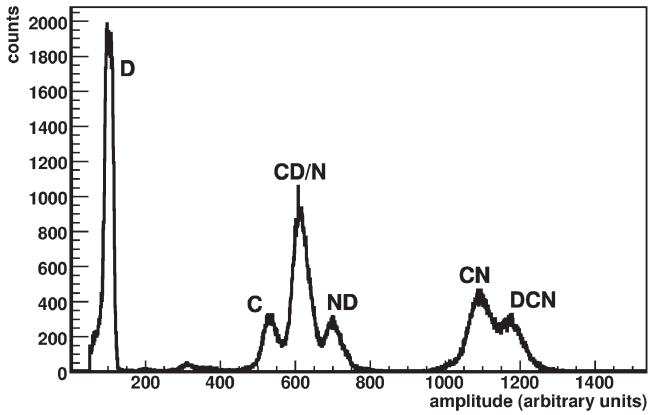

Fig. 59. Pulse height spectrum of a finely segmented surface barrier detector for neutral fragments from reactions of $DCND^+$ with residual gas. The spectrum shows peaks corresponding to mass 2, 12, 14, 16, 26 and 28 u. Coincident pulses yield a sum of up to mass 30 u (DCND).

integer multiple of the revolution frequency of the simultaneously stored N_2D^+ or DCO^+ beam allows to separate also N_2D^+ or DCO^+ ions.

4.9.3 Deceleration

In tests devoted to the deceleration of highly charged ions, a reduction of the beam energy by a factor of > 7, from 73.3 MeV to 9.7 MeV (1 MeV/u), corresponding to a rigidity decrease from 0.71 Tm to 0.26 Tm could be achieved for $^{12}C^{6+}$ ions. About 85% of the injected ions could be decelerated to the final energy [235]. Former deceleration tests using the rf-booster were much more difficult and resulted in beam losses of several orders of magnitude. This feature now considerably widens the operating range with highly-charged ions produced at the MPIK accelerators for stored ion beam experiments at the TSR.

4.9.4 Short ion bunches

For efficient ion beam deceleration small initial longitudinal bunch lengths, obtained by bunched beam electron cooling, are required. Even smaller longitudinal bunch lengths are necessary for experiments with a reaction microscope in a storage ring. Tests were therefore performed with 50 MeV $^{12}C^{6+}$ ion beams using the 6^{th} harmonic for bunching. A bunched ion beam profile obtained with simultaneous electron cooling measured with a capacitive pick-up is shown in Fig. 60. The intensity of the $^{12}C^{6+}$ ion beam with $E = 50$ MeV used for this measurements was $I = 45$ μA. The resonator voltage was set to 795 V. Also shown in Fig. 60 is a parabola fit function (red line), which represents the data very well. A bunch length, defined in Fig. 60, of $w = 20$ ns can be obtained from the fit. This bunch length is space charge limited. In the space charge limit the voltage of the resonator $U_i(\Delta\phi) = U\sin(\Delta\phi + \phi_s)$, each ion is passing through, is compensated by the longitudinal space charge voltage of the ion beam. For bunching in the TSR standard mode, where the slip factor $\eta = \frac{\Delta f_0/f_0}{\Delta p/p}$ is positive, the synchronous phase used for bunching is $\phi_s = 0$, where f_0 is the revolution frequency

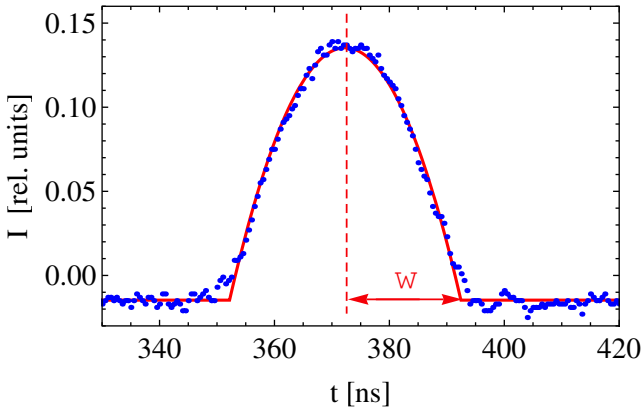

Fig. 60. Measured electron cooled longitudinal ion beam ($^{12}C^{6+}$, $E = 50\,\mathrm{MeV}$) profile. The width of the parabola profile is defined by w.

of an ion and p describes its momentum. Because the synchrotron oscillation is a very slow process compared to the revolution time, the longitudinal electrical field $E_{\parallel}(\Delta\phi)$, seen by one ion, can be assumed to be constant during one turn and the space charge voltage can be defined by $U_s(\Delta\phi) = E_{\parallel}(\Delta\phi) \cdot C_0$, where C_0 denotes the circumference of the storage ring. The ion phase $\Delta\phi$ is related to the longitudinal position s in the bunch: $\Delta\phi = -\omega s / v_s$, where ω is the angular frequency of the resonator and v_s the velocity of the synchronous particle, located in the center of the bunch at $s = 0$. Ions in front of the synchronous particle ($s > 0$) arrive at the resonator gap earlier than the synchronous one, therefore there is a negative sign in the formula. The longitudinal electrical field $E_{\parallel}(s)$ can be calculated from the charge line density $\lambda(s)$ of the bunch by the following formula [255]:

$$E_{\parallel}(s) = -\frac{1 + 2\ln(\frac{R}{r})}{4\pi\epsilon_0\gamma^2}\frac{\partial\lambda(s)}{\partial s}. \tag{40}$$

The constant ϵ_0 is the absolute permittivity and γ is the relativistic mass increase (for TSR energies $\gamma = 1$). R denotes the radius of the beam tube ($R = 0.1\,\mathrm{m}$) and r is the average beam radius, defined by twice the two σ_r value ($r = 2\sigma_r$) of the transverse beam width. A parabola density profile is the only longitudinal charge line distribution, for an electron cooled ion beam with $\Delta\phi \ll 2\pi$ ($\sin(\Delta\phi) = \Delta\phi$), which compensates the resonator voltage $U_i(\Delta\phi)$ for each ion, independent of its phase $\Delta\phi$. The parabola charge line density $\lambda(s)$ can be calculated from the number N_B of particle in the bunch:

$$\lambda(s) = \frac{3N_B q}{4w_s}\left(1 - \frac{s^2}{w_s^2}\right) \tag{41}$$

for $|s| \leq w_s$, with $\int_{-w_s}^{w_s}\lambda(s)ds = N_B \cdot q$. The charge of an ion is q and w_s describes the bunch length in meters, related to the bunch length w in seconds, $w_s = v_s \cdot w$, defined in Fig. 60. If $U_i(\Delta\phi)$ is completely compensated by the space charge voltage $U \cdot \sin(\Delta\phi + \phi_s) + E_{\parallel}(\Delta\phi) \cdot C_0 = 0$, the synchrotron oscillation of each particle in the bunch is freezed. This condition leads finally to the longitudinal space charge limit. For a beam, having a parabola longitudinal charge line density, the space charge limit is given by the following formula:

$$w = C_0\sqrt[3]{\frac{3(1 + 2\ln(\frac{R}{r}))I}{2^4\pi^2c^4\epsilon_0\gamma^2h^2\beta^4U}}\ . \tag{42}$$

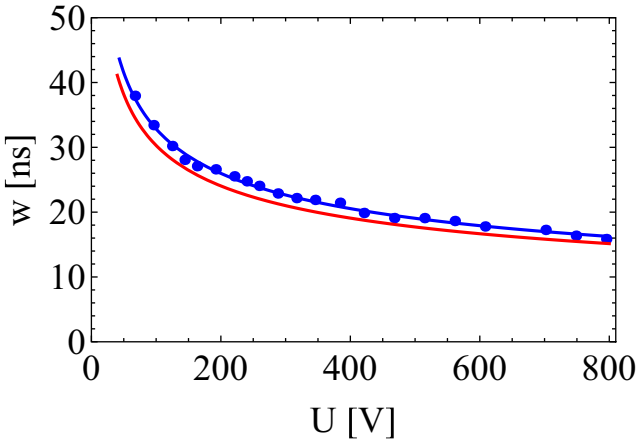

Fig. 61. Measured bunch length w for an electron cooled $^{12}C^{6+}$ ion beam ($E = 50\,\text{MeV}$, $I = 20\,\mu\text{A}$) as a function of the resonator voltage. The red curve is a calculation in which formula (42) was used.

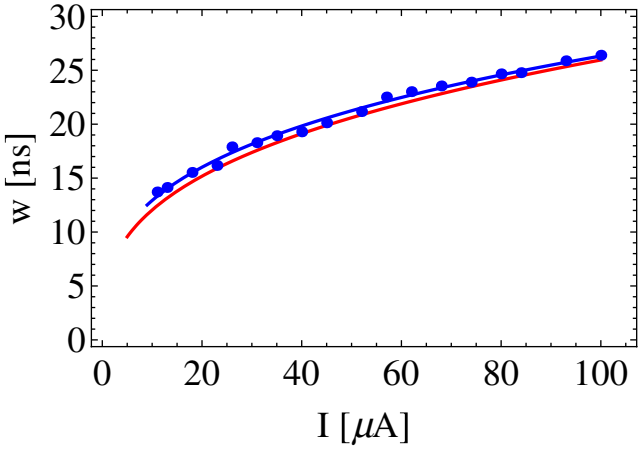

Fig. 62. Measured bunch length for an electron cooled $^{12}C^{6+}$ ion beam as a function of the ion intensity. The resonator voltage used in this measurement was $U = 795\,\text{V}$. The red curve is a calculation using formula (42).

The bunch length w in formula (42) is determined by the beam intensity I, the resonator voltage U, the number of bunches h in the ring and the beam velocity β in units of the speed of light c. If the space charge voltage $|U_s(\Delta\phi)|$ of the ion beam would be larger than $|U_i(\Delta\phi)|$, the magnitude $|\Delta\phi|$ of each ion would increase by the repelling space charge force, resulting in an increase of the bunch length. On the other hand a larger bunch has a smaller space charge voltage $|U_s(\Delta\phi)|$, thus the ion starts to oscillate. These oscillations $\Delta\phi$ will be damped by the electron cooler, bringing back the beam to the space charge limit. Therefore an electron cooled ion bunch in the space charge limit is stable. With an average transverse beam seam size σ_r=1 mm, the bunch length w can be calculated. Figure 61 shows the measured bunch length w as a function of resonator voltage U as well the theoretical prediction (red curve). As it is shown in Fig. 61 the calculated function with the fit to the data ($w \sim U^{-0.34}$), blue line, agrees very well. At the same number of bunches $h = 6$, the bunch length w was measured as a function of the beam intensity, shown in Fig. 62.

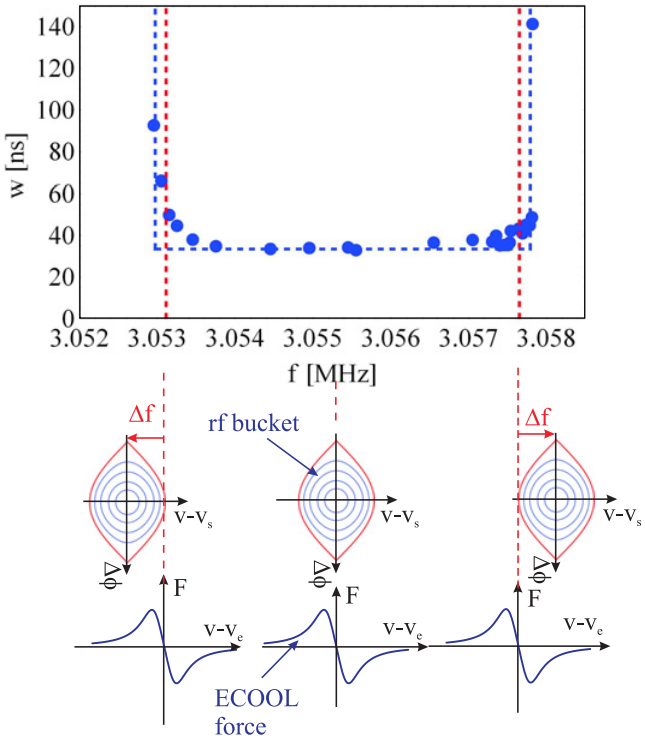

Fig. 63. Measured bunch lengths for an electron cooled $^{12}C^{6+}$ ion beam as a function of the rf frequency f. Also shown is the explanation of the bunch length increase at large frequency shifts.

The resonator voltage used in these measurements was $U = 795\,\mathrm{V}$. A fit through the data, blue curve, gives an exponent of 0.31, which is slightly less than the predicted value of 1/3. Furthermore the bunch length w was measured as a function of the rf frequency for a $^{12}C^{6+}$ ion beam with $E = 50$ MeV. The result of these measurements are displayed in Fig. 63. The voltage used in this measurement was $U = 96\,\mathrm{V}$ and the ion current was $I = 20\ \mu\mathrm{A}$. As it can be seen in Fig. 63 the bunch lengths are constant around $w = 33$ ns in a relatively wide frequency range. At the borders the bunch lengths are increasing rapidly. There is a deviation from the parabola bunch shape if the bunch length is larger than $w = 90$ ns. Outside the boundaries, blue marked vertical lines in Fig. 63, there are no observed ion bunches. This behavior can be explained also with Fig. 63. If the rf frequency f is changed, the velocity v_s and the revolution frequency f_s of the synchronous particle, which has to fulfill the equation $f = h \cdot f_s$, is modified. This means that the rf bucket, where the synchronous particle is sitting in the center ($v = v_s$), is shifted with respect to the velocity v_e of the electron beam. The cooling force of the electron cooler tries to shifts the ion velocity v to the electron velocity v_e. If the electron velocity v_e comes to the outside of the rf bucket no bunching is possible, due to the missing closed orbits in the longitudinal phase space around the synchronous particle. The experimental values found for the two limits are $\Delta f_l = \pm 2.37$ kHz, which is close to the bucket height $\Delta f_b = 2.27$ kHz calculated with: $\Delta f_b = 1/C_0\sqrt{2|\eta|hqU/\pi m}$, where m is the mass of an ion. In Fig. 63 the bucket size (red lines) are also shown. The small frequency difference between the vertical blue and red dashed lines can be explained by the momentum spread of the stored ion beam.

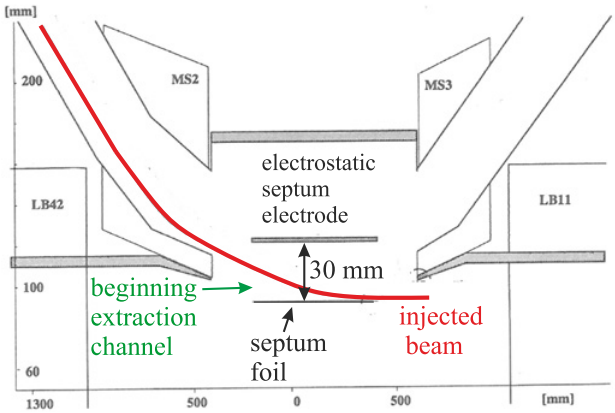

Fig. 64. Electrostatic septum for injection and extraction.

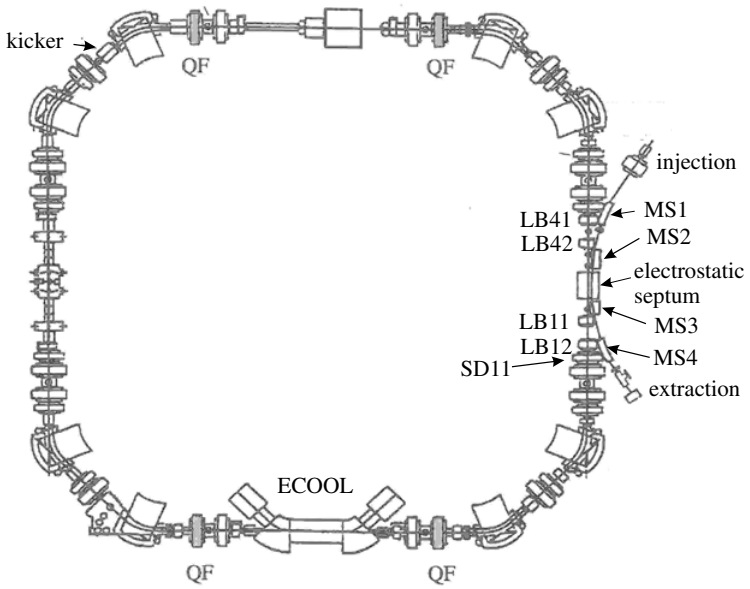

Fig. 65. Picture of the TSR with extraction elements. Quadrupole family QFX1 (gray) is used to setup the tune. Sextupole magnet SD11 is utilized to excite the third order resonance $Q_x = 8/3$.

4.10 Slow extraction

At the Heidelberg heavy ion cooler storage ring a slow beam extraction system using the third order resonance $Q_x = 8/3$ is installed. The same electrostatic septum is employed for the extraction and for the injection. Figure 64 shows the section used for injection and extraction. The vertical coordinates show the distance to the beam tube center, whereas the horizontal axis displays the distance to the center of the injection-extraction straight section. The distance between the septum foil and the septum electrode is 30 mm. In order to extract the stored ion beam, the ion beam has to be led into the electrostatic septum. At the slow extraction method the betatron motion of the ion beam particles are exited resonantly using a third order resonance. This leads within many revolution to an increase of the amplitude of the betatron

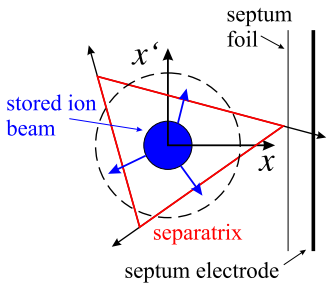

Fig. 66. The slow extraction process at the TSR.

motion. Generally this process yields to a particle loss due to collisions with the beam tube. In order to avoid the particle loss the acceptance of the storage ring should have its smallest value at the position at beginning of the extraction channel (electrostatic septum). To accomplish this condition the central orbit at the position at the electrostatic septum is shifted about 60 mm by using four dipole magnets (LB11, LB12, LB41, and LB42; compare Figs. 42 and 65). Therefore the distance between central orbit and septum foil is only 30 mm, while in the remaining part the central orbit has a distance of 100 mm to the beam tube wall.

The most important variables to characterize the slow extraction process are the separatrix and the emittance of the stored ion beam. The separatrix separates stable and unstable regions in the transversal phase space. Particles which are inside the separatrix are stored safely, whereas a particle outside the separatix increases its betatron amplitude and reaches the extraction channel of the electrostatic septum. In Fig. 66 a scheme of the slow extraction process at the TSR is shown. To extract the ion beam the horizontal betatron tune is shifted to the third order resonance generating a separatrix (red straight lines in Fig. 66) in the transversal phase space around the stored ion beam. To extract the ion beam:

(1) the third order resonance $Q_x = 8/3$ has to be excited by one or two sextupole magnets.
(2) the emittance of the stored ion beam has to be increased by applying rf noise with a frequency spread of typically about several kHz to the horizontal kicker, where the center frequency f_x of the noise has to fulfill the condition:

$$f_x = f_0(n \pm q). \tag{43}$$

The revolution frequency of the ion beam is given by f_0. The variable n in Eq. (43) is an integer number and q is the non integer part of the tune. With this method the extraction rate can be set up by the noise level. To extract the ion beam the third order resonance is excited by the sextupole magnet SD11, compare Fig. 65, the integral strength of the sextupole is typically $1.5\,\mathrm{m}^{-2}$. The time scheme used to extract the beam is displayed in Fig. 67. In the slow extraction experiment [256] the $^{12}C^{6+}$ ion beam ($E = 73.3$ MeV) is injected at the tune $Q_x = 2.64$. After injection the ion beam is cooled to reduce the transverse phase space. After cooling the horizontal tune is shifted from Q_x=2.64 to Q_x=2.662, by changing the setting of quadrupole family QFX1. At the time 1.3 s the transverse phase space is blow up by noise given to the horizontal kicker. After 9.5 s the noise is switched off and the quadrupole setting is changed to the injection value. To investigate the slow extraction process the development of the horizontal beam width, shown in Fig. 68 and the extraction rate, shown in Fig. 69, were measured during the extraction process. The interpretation

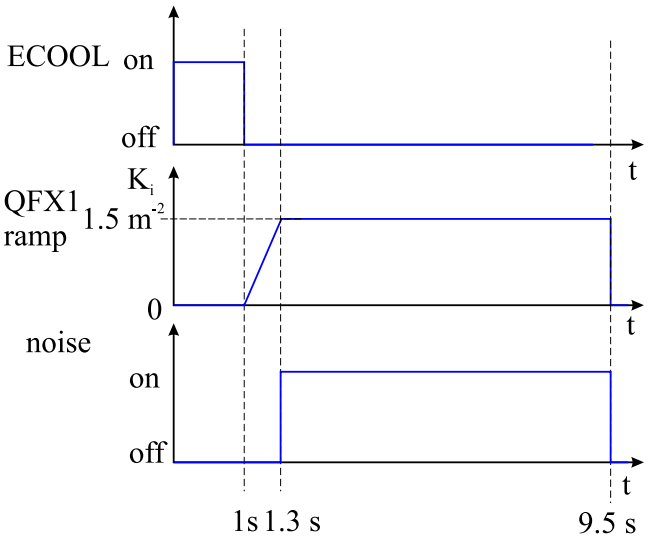

Fig. 67. Timing scheme of slow extraction.

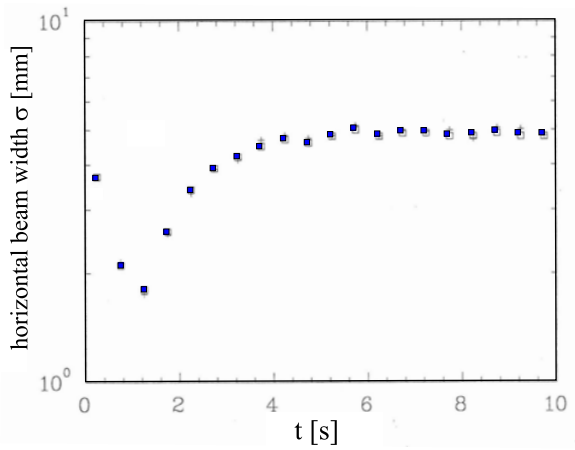

Fig. 68. Development of the beam width during the extraction process.

of the time development is the following:

- Up to 1 s after injection:
  Due to electron cooling a reduction of the horizontal beam profile can be recognized.
- Between 1 s and 1.3 s after injection:
  The value of quadrupole family QFX1 is changed, decreasing the distance to the third order resonance so that the separatrix size is reduced. Due to electron cooling the size in the transversal phase space is still inside the separatrix, therefore no ions are extracted.
- Between 1.3 s and 1.8 s after injection:
  After 1.3 s noise is transferred to the horizontal kicker blowing up the transverse phase of the stored ion beam, recognizable in the increase of the beam size. But still no ions reaches the separatrix, visible on the counting rate of the extracted ion beam.

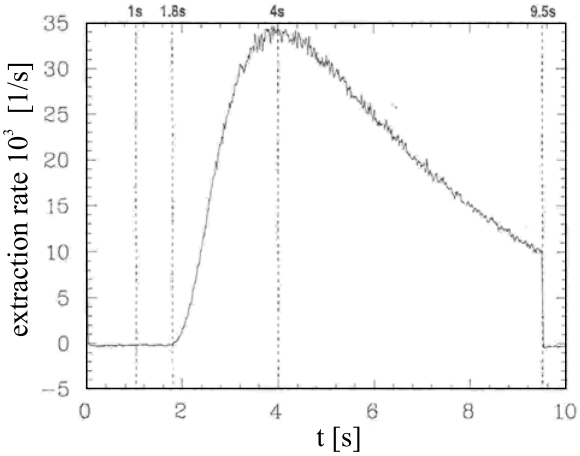

Fig. 69. Extraction rate during the slow extraction process.

- Approximately between 1.8 s and 4 s after injection:
  Approximately 1.8 s after injection the extraction rate increases, reaching its maximum value at 4 s. In that time range the width of the beam profiles increases further.
- approximately between 4 s and 9.5 s after injection:
  After 4 s the extraction rate reaches its maximum and the size of the beam width is kept constant as recognizable in Fig. 68. The size of the profile is now determined by the separatrix size.
- After 9.5 s:
  The noise is switched off and no particle is extracted.

The emittance, defined by the two σ value, of the extracted beam was measured to be horizontally $\epsilon_x = 1 \pm 0.2$ mm mrad and in the vertical degree of freedom an value of $\epsilon_y = 1.1 \pm 0.1$ mm mrad was determined in that experiment [256] for the extracted carbon beam. The extraction efficiency is the ratio between the number of extracted particle to the stored ion number reduction. An efficiency of $85 \pm 4\%$ was determined [256] if electron pre-cooling is used before extraction takes place. Without electron pre-cooling the extraction efficiency is reduced to $27 \pm 2\%$ [256], because without electron cooling the vertical width of the stored ion beam is much larger than the vertical acceptance of the extraction channel, resulting in ion collisions with the extraction vacuum chambers.

4.11 The diagnostic system of the TSR

4.11.1 Beam Position Measurement

In order to determine the horizontal and vertical positions of a bunched ion beam the TSR is equipped with 8 beam position monitors. All beam position monitors consist of a vertical and horizontal pick-up composed of two metallic electrodes. To determine the beam position the beam induced voltages on both electrodes are measured. The difference of these two voltages is proportional to the distance between the beam position and the pick-up center. The beam position monitor (BPM) is shown in Fig. 70. The plates of the horizontal and vertical BPM are clearly seen. The inner

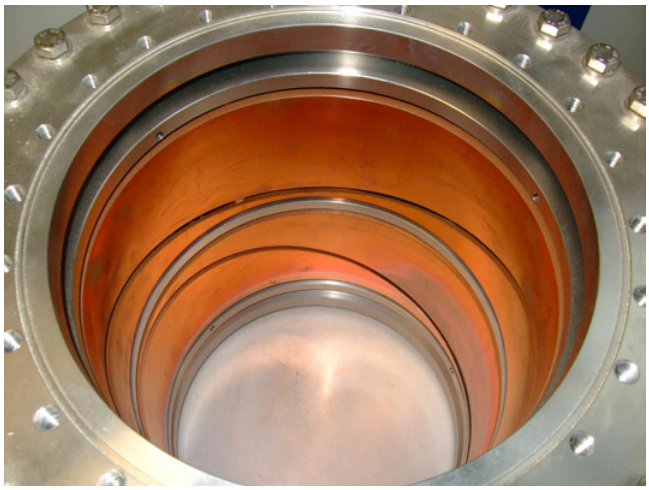

Fig. 70. Beam position monitor of the TSR.

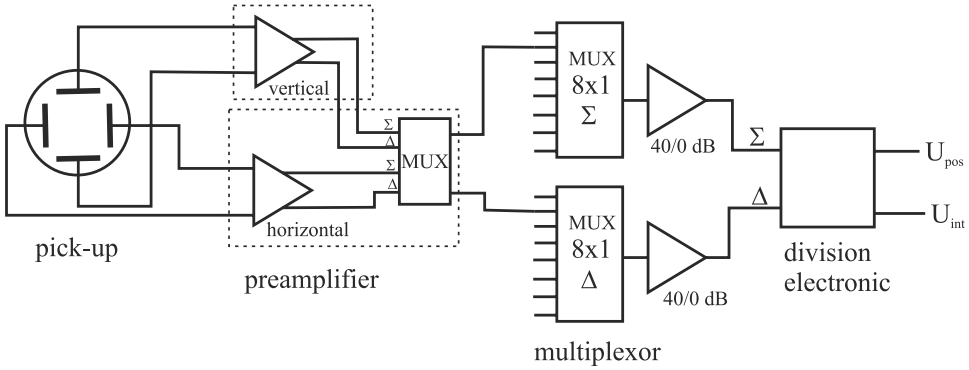

Fig. 71. General survey of the beam position system.

diameter of the BPM is 200 mm. The position x of the beam can be expressed by the two induced voltages U_1 and U_2:

$$x = a_{scal} \frac{U_2 - U_1}{U_2 + U_1}, \tag{44}$$

where the scaling factor a_{scal} was measured to be: $a_{scal} = 195.9 \pm 0.2$ mm [257].

Figure 71 shows a general overview of the total beam position system as realized at the TSR. Both preamplifier used for measuring the horizontal and vertical beam positions are mounted directly at the pick-up. Each pick-up is connected via several multiplexers with the division electronic. One multiplexer mounted in the horizontal preamplifier switches the output of the horizontal or vertical pre-amplifier. An additional multiplexer connects each pick-up with the division electronics. Both multiplexers are connected via control lines with a VME-Computer. The sum signal and the difference signal are generated in the pre-amplifier from the signals of two counterpart electrodes. In the division the ratio of the difference signal Δ and sum signal $\sum$ is provided. Due to the relation $x \sim \Delta U / \sum U$ one have a signal which is proportional to the beam position [257]. Beside the position signal U_{pos} the division electronics generates a signal U_{int} which is proportional to the beam intensity. Since there is only one division electronics, the multiplexers are used to select the pick-up

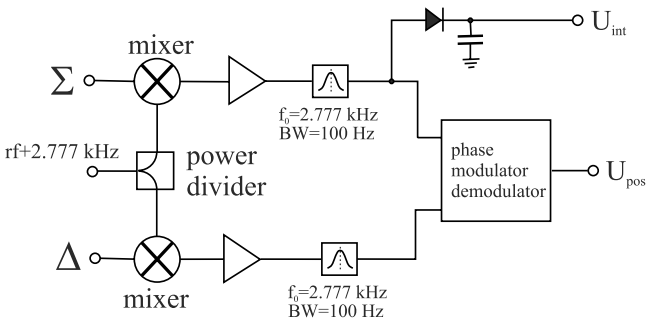

Fig. 72. Scheme of the division electronics.

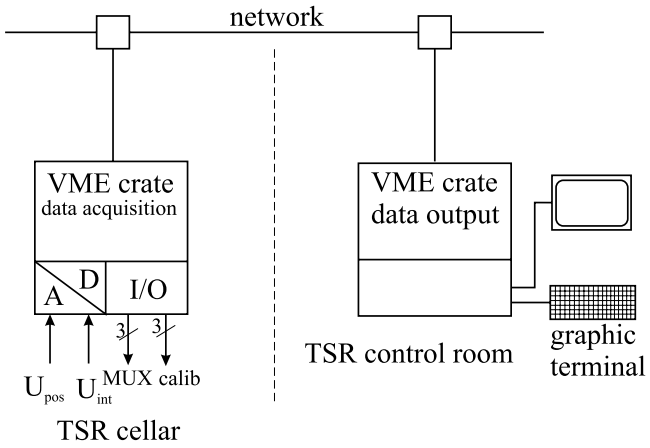

Fig. 73. Scheme of the pick-up computer control system.

as well the direction of measurement (horizontal or vertical). The measuring time at one electrode pair is about 20 ms. Because the TSR has totally 8 pick-ups equivalent to 16 electron pairs the total measuring time of all pick-up signals is about 320 ms. The division electronic, shown in Fig. 72, is substantially a frequency selective voltage measuring device measuring the amplitude ratio of the pick-up difference signal and the pick-up sum signal.

The first part of the division electronics is the mixer stage consisting of two mixer, amplifier and filters. The second stage is the phase-modulator-demodulator. The division electronics has two output signals, the position sensitive voltage U_{pos} and the voltage U_{int} proportional to the bunched stored ion current. The mixing stage is the frequency selective part of the division electronics. First of all the spectrum of the sum signal and difference signal is mixed down to 2.777 kHz. For this purpose both rf signals are multiplied with a frequency $f_m = f_{rf} + 2.777$ kHz, where f_{rf} is the frequency of the rf system. Signals with both frequencies f_{rf} and f_m are generated in a DDS card located in the main TSR computer. The mixed signals, containing the frequency component 2.777 kHz, are filtered by a narrow-band filter (band width 100 Hz) at $f_{filter} = 2.777$ KHz. The phase-modulator-demodulator circuit is an analog circuit to generate the ratio of the pick-up difference and sum signals [257]. The output signal of the division electronics U_{int} is fed to an ADC card located in a VME crate. The computer control system to control the position measurements is shown in Fig. 73. The computer control system can be divided in two blocks. The first part contains the data acquisition system with the ADC card and the I/O card to control

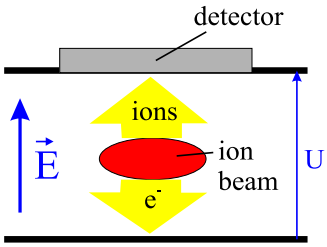

Fig. 74. Principle of the residual gas ionization monitor. Residual gas ions produced by the stored ion beam are accelerated into a position sensitive detector.

the multiplexers. The other part is the graphical display. Both blocks contain a VME computer connected via a network.

4.11.2 The residual-gas ionization beam profile monitor

A monitoring device for the transverse density distribution of stored heavy ion beams, based on the the detection of ionization products of the beam particles in the residual gas is installed in the TSR [258]. With two monitor units installed in the ring, non-destructive, sensitive measurements of the horizontal and vertical profiles of cooled stored ion beams can be performed with a spatial resolution of about 0.3 mm. The beam profile monitors are used to determine the transverse beam temperature, to study transversal cooling and heating mechanisms, to observe the ion beam behavior during experiments and to determine storage-ring parameters such as the dispersion function. The principle of a residual gas ionization profile monitor is illustrated in Fig. 74. The circulating beam crosses the free volume between two parallel plates. High voltage applied to the plates results in a homogenous electrical field $\vec{E}$ perpendicular to the beam direction. Residual gas ions produced in collisions of residual gas molecules with the stored ions accelerated by the electrical field into a position sensitive detector mounted on one plate. This leads to a projection of the beam profile onto the detector, because the number of ionized residual gas ions in a given volume is proportional to the density of the incident ion beam. The rate of ions on the detector surface is given by:

$$R = \eta\sigma n v N, \tag{45}$$

where N is the number of stored ions, v the ion velocity, n the residual gas density ($n \approx 10^6\,\mathrm{cm}^{-3}$ at $p = 5 \cdot 10^{-11}\,\mathrm{mbar}$), σ is the ionization cross section of the residual gas, and η is the ratio of the detector length and circumference of the storage ring. A typical counting rate for $^{12}C^{6+}$ ions with $E = 50\,\mathrm{MeV}$ at $I = 1\,\mu\mathrm{A}$ is $R \approx 200\,\mathrm{s}^{-1}$ ($\eta \approx 3 \cdot 10^{-4}$). A horizontal and vertical beam profile monitor is installed in the TSR. The material as well as the machining and assembling procedures were carefully chosen to fulfill the ultra high vacuum requirements of the TSR, aiming at residual-gas pressures in the low $10^{-11}\,\mathrm{mbar}$ region. The monitors are bakeable at 300 °C and the corresponding vacuum vessel is equipped with the sublimation and ion getter pumps. Being mounted on flanges connected to a bellow and a pneumatic drive, the image component can be moved in and out of the beam in the horizontal direction. In the horizontal beam profile monitor a rectangular MCP with a active area of $15 \times 100\,\mathrm{mm}$ is used. A horizontal size of 100 mm was chosen to detect the complete horizontal profile on an uncooled injected ion beam. The dimension of the end plates (compare Fig. 75) are $85 \times 160\,\mathrm{mm}$, the distance is 50 mm. In the vertical beam profile monitor a MCP with a full active area of a diameter of 40 mm used. This size also

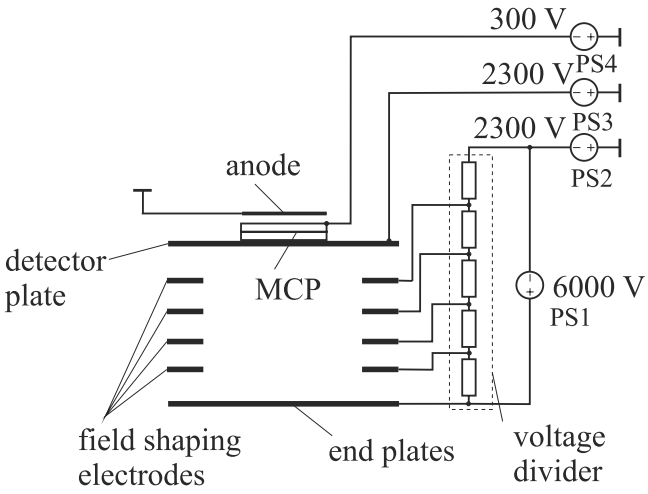

Fig. 75. High voltage system of the imaging component with typical operation voltages (PS: power supply, MCP: multi-channel plate).

covers the maximum extension of uncooled beams in the vertical degree of freedom. The extensions of the detector plate are 100×100 mm. The distance between them is 110 mm.

The high voltage system of the image component is shown in Fig. 75. A positive voltage of typically 6 kV is applied to the end electrode by the power supply PS1. In order to keep the resulting electric field homogenous over the active volume, the potential on the field-shaping electrodes is gradually reduced towards the detector plate by means of a voltage divider mounted across the vacuum feedthroughs on the atmospheric side. The bias voltage of the detector is generated by the separate power supply PS3 in order to avoid additional noise which might be caused by PS1 and to have the possibility of an independent control of the detector bias. Correspondingly, PS1 has a floating ground potential defined by PS2, which must be set at the same voltage as PS3 to maintain a constant electrical field. Finally, an additional power supply PS4 is needed to pull the electrons from the exit of the MCP to the detector anode which is operated close to ground.

A Chevron MCP assemblies consisting of two micro channel plates in series is used to detect the residual gas ions (Fig. 76). It has an amplification of $\approx 10^7$, which is necessary for the electronic detection of single residual gas ions impacting on the active surface. The detection efficiency for hydrogen ions of 5 keV is estimated to be 60–85% [259]. The bias voltage of the channel plates is determined by the difference of the voltages defined by PS3 and PS4 (see Fig. 75) and is adjusted to 1000 V per plate. The electron cloud resulting from an incident ion is accelerated onto the resistive anode (RA) mounted a few mm behind the MCP. The RA consists of a resistive sheet on a ceramic substrate. Electrical contact is made to two electrodes at the opposite ends of the sheet (total resistance $\approx$ 200 kΩ and to a rear metal plate providing a capacitive coupling of the resistive layer to the ground. Tests suggested a value of 300 V for the acceleration potential between MCP and RA to ensure an optimal spatial resolution. Among the various possibilities available for a position sensitive readout of channel plates, a resistive anode was chosen mainly for practical reasons. The resistive anode requires only two signal lines and therefore only two ultra-high vacuum feedthroughs, while the necessary shielding of the signal lines in the vacuum chamber can be realized without too much technical effort. The position signals from the resistive anode are red out by the rise-time method [259]. Figure 76 shows a

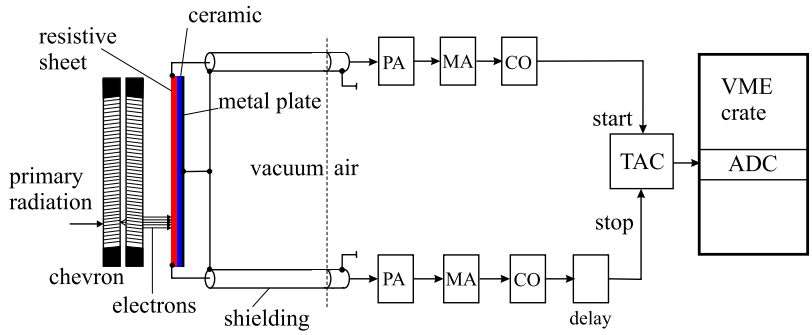

Fig. 76. Chevron micro-channel plate assembly and block diagram of the readout electronics for the pulse rise-time method (PA: charge-sensitive preamplifier, MA: main amplifier, CO: single-channel analyzer in cross-over mode, TAC: time-to-amplitude converter, ADC: analog-digital converter.)

Table 18. The DC current transformer.

resolution	1 μA
zero drift (1 hour)	$< \pm 4\mu$A
linearity error	$< \pm 0.005\%$
current range	-10 mA to 10 mA

block diagram of the readout electronics used to measure the difference of pulse rise time of the pulse occurring at each end of the resistive sheet, which are proportional to x and $L - x$ respectively, where L is the length of the resistive strip line and x is the event location. Charge pulses at each end are integrated in charge sensitive preamplifiers (PA), whose output pulses are shaped by spectroscopy main amplifiers (MA) with bipolar output. The zero crossing times of the amplifier output pulses represent the rise time of the input signals. The zero crossing are detected by single channel analyzers in cross over mode (CO), which generate fast logic pulses used to start and stop a time to amplitude converter (TAC). The analog output signal from the TAC is digitized in a analog to digital converter (ADC) located in the VME crate of the TSR control system. The pulse height spectrum of the ADC input signal represents the spatial distribution of the ions detected by the MCP. Horizontal beam profile measured with the beam profile monitor during electron cooling is shown in Fig. 46.

4.11.3 Current transformer

The current transformer is an instrument to measure the intensity of the stored bunched or a DC ion beam. This current transformer was developed by K. Unser. The working principle of the beam current transformer is described in Ref. [260]. The system consisting of a toroidal sensor, a front-end electronics box and back-end power supply was bought from the company Bergoz. The toroidal sensor is connected to the electronic box by two multicore cables equipped with 8-pin Burndy connectors. Because the toroidal magnetic sensor is very sensitive to magnetic fields a good shielding from external magnetic fields is required. The multilayer magnetic shield housing the magnetic sensor is shown on the right side in Fig. 77.

The properties of the DC current transformer are listed in Table 18.

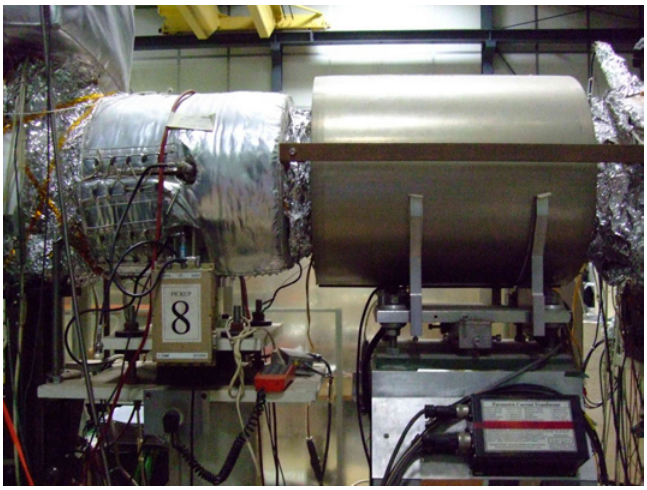

Fig. 77. Multilayer magnetic shielding of the current transformer housing the magnetic sensor (right). On the left side the thermic isolation of pick-up 8 is visible.

4.11.4 Intensity measurement of a bunched ion beam

The minimum current which can be detected by the DC transformer is $1\,\mu$A. The ion current can be measured much more sensitively with a pick-up if the ion beam is bunched and electron cooled [261]. At TSR a current pick-up consisting of a tube surrounding the stored ion beam is used to measure the total intensity of the electron cooled, bunched ion beam. If the pick-up electrode is loaded with a pre-amplifier with a very high input resistance the spectrum of the pick-up voltage $\hat{U}_n$ can be expressed by:

$$\hat{U}_n = \frac{L}{v \cdot C}\hat{I}_n, \tag{46}$$

where L describes the pick-up length and v the velocity of the ions. The total capacity of the pick-up, the cable connecting the pick-up with the preamplifier and the pre-amplifier is denoted by C. The bunch length w of the bunched electron cooled ion beam is space charge limited, having a parabolic longitudinal density profile [254]. The current spectrum $\hat{I}_n$, at the harmonic number n of the rf frequency f_0 ($f_0 = \frac{\omega_0}{2\pi}$), of a beam having a parabolic charge line distribution is determined by the bunch length w:

$$\hat{I}_n = \frac{6 \cdot \bar{I}(\sin(nw\omega_0) - nw\omega_0 \cos(nw\omega_0))}{n^3 w^3 \omega_0^3}. \tag{47}$$

The dependency of the bunch length w on the average beam current $\bar{I}$ can described by [254] (compare Sect. 4.9.4):

$$w = C_0 \sqrt[3]{\frac{3(1 + 2\ln(\frac{R}{r}))\bar{I}}{2^4\pi^2 c^4 \epsilon_0 \gamma^2 h^2 \beta^4 U}}\ . \tag{48}$$

The bunch length w in formula (48) is determined by the beam intensity $\bar{I}$, the resonator voltage U, the number of bunches h in the ring (circumference C_0) and the beam velocity β in units of the speed of light c. The constant ϵ_0 is the absolute permittivity and γ is the relativistic mass increase (for TSR energies $\gamma \approx 1$). R denotes the radius of the beam tube and r is the average beam radius, defined by

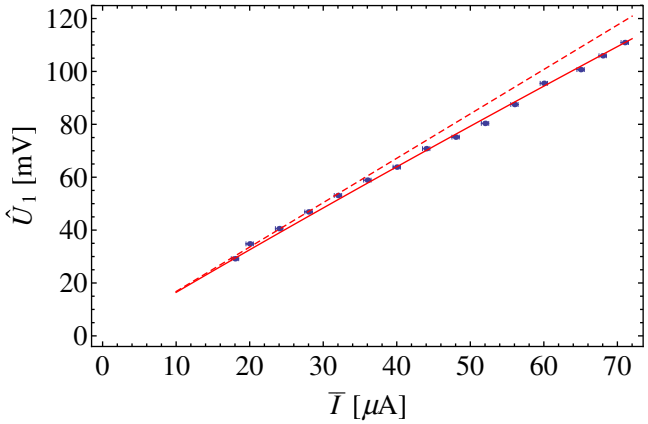

Fig. 78. Measured pick-up signal as a function of the current of a silicon beam having a velocity of $\beta = 0.0872$.

the $2\sigma_r$ value of the transverse beam width. From Eqs. (46), (47) and (48) a formula can be derived which can be used to calculate the average beam intensity $\bar{I}$ from the measured voltage spectrum $\hat{U}_n$ of the pick-up signal. Since $w \ll 1/f_0$, Eq. (47) can be Taylor expanded, resulting in an approximative formula to calculate the average beam intensity $\bar{I}$ from the measured voltage spectrum amplitude $\hat{U}_1$ at rf frequency f_0:

$$\bar{I} = \frac{vC}{L}\frac{\hat{U}_1}{2}. \tag{49}$$

At the TSR storage ring an experiment was carried out to determine the dependency of the component $\hat{U}_1$ of the pick-up voltage spectrum on the average beam current $\bar{I}$. This measurement was performed with $^{28}Si^{8+}$ ions ($E = 57\,\mathrm{MeV}$). The average beam current was measured with the DC transformer of the TSR storage ring. As shown in Fig. 78, $\hat{U}_1$ increases linearly at low ion intensities with the stored intensity as predicted by Eq. (49). The solid red line in Fig. 78 is a fit through the measurements using Eqs. (46), (47) and (48) where the capacity C was used as a free fit parameter. From the fit a value of 171 pF could be derived for C which is close to the capacity C= 176 pF measured using an LC meter. The red dashed line is the calculated spectrum $\hat{U}_1$ using Eq. (49) with $C = 171$ pF. The capacity from the fit can now be used to determine the beam current for any ion species having different ion velocities. Because the spectrum of the pick-up signal scales with the inverse of the ion velocity (compare Eq. (49)) this method to determine the absolute intensity of an electron cooled, bunched ion beam is very sensitive for low velocity ion beams.

4.11.5 The Schottky pick-up

To measure the revolution frequency and the momentum spread of a stored ion beam, Schottky noise diagnostics is used, meaning that the noise spectrum of the ion beam current is measured. The Schottky spectrum consists of many Schottky bands with a certain height and width. The distance between two neighboring bands corresponds to the revolution frequency. The width of one Schottky band is connected to the momentum spread $\Delta p/p$ of the ions. The width of the n^{th} band is given by

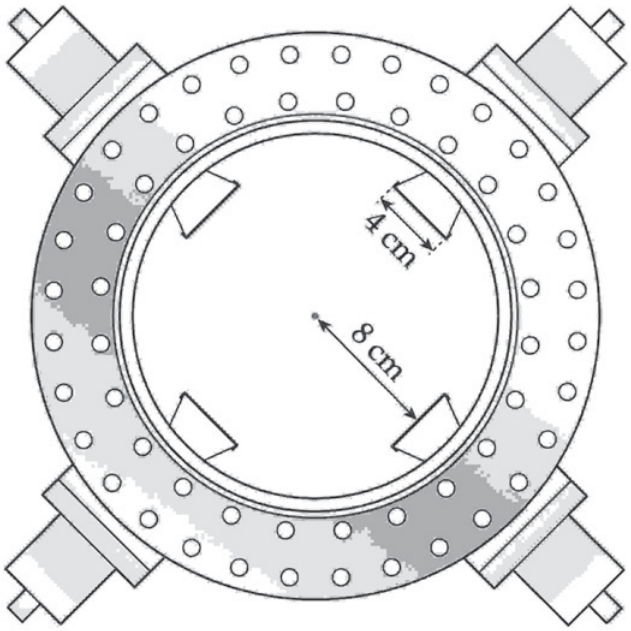

Fig. 79. Sketch of the Schottky pick up in the TSR.

$\Delta f_n = n\Delta f_0$, where Δf_0 depends on the momentum spread of the stored ion beam:

$$\frac{\Delta f_0}{f_0} = \eta \frac{\Delta p}{p}. \tag{50}$$

η is the slip factor defined in Sect. 4.3. The power of each Schottky band remains constant:

$$\int \frac{d\hat{I}_n^2}{df} df = (2qf_0)^2 N, \tag{51}$$

where N is the number of stored ions with charge state q. To detect the Schottky noise of the stored ion beam a Schottky pick-up is used. Figure 79 shows the Schottky pick-up of the TSR. The existing Schottky pick-up is made of four 4 cm wide conductor strip lines, each located about 8 cm from the center of the beam path in opposing corners. The Schottky power induced at one strip line is defined as:

$$P(f) = \int \frac{d\hat{U}^2}{df} df,$$

where $d\hat{U}^2/df$ is the spectral power density of the strip line voltage. The Schottky power at harmonic number n, measured at one strip line, is given by [262]:

$$P(\omega_n) = \kappa^2 4N(qf_0)^2 \frac{R^2}{1+\omega_n^2 C^2 R^2} \left(1 - \cos\left(\omega_n \frac{L}{v}\right)\right), \tag{52}$$

where N is number of ions with charge q and $\omega_n = n2\pi f_0$. C describes the total capacity of the pick-up, cables and preamplifier. The input resistance of the preamplifier

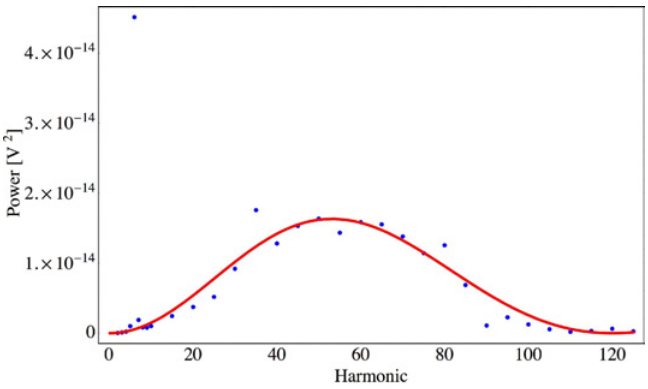

Fig. 80. Harmonic power spectrum of $^{12}C^{6+}$ ion beam ($E = 50\,\text{MeV}$), measured with one strip line of the Schottky pick-up and the NF 50 Ω amplifier including fit through the data points.

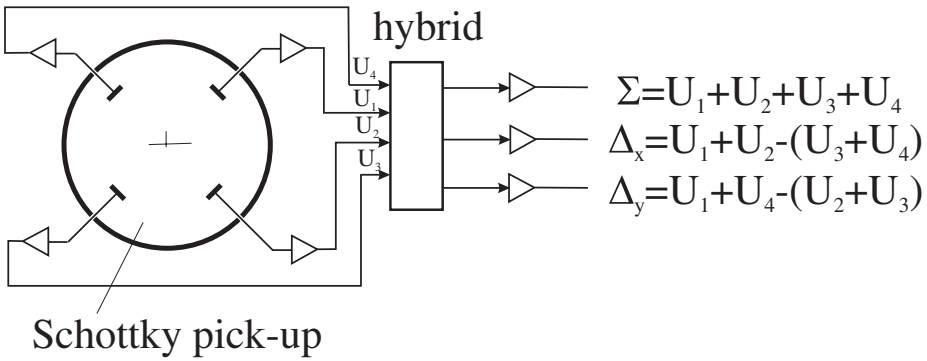

Fig. 81. Scheme of the Schottky signal processing.

is given by R. The factor κ is the ratio between the width of one strip line and the circumference of a tube with a radius which corresponds to the distance of one strip line to the beam center. The Schottky harmonic power spectrum measured at one strip line of the Schottky pick-up and an amplifier ($R = 50\ \Omega$) is shown in Fig. 80. It shows the power in each Schottky band as a function of the harmonic number of the revolution frequency $f_0 = 512\ kHz$ for a 50 MeV $^{12}C^{6+}$ with a beam current of $I = 20\,\mu\text{A}$. The power of the Schottky bands was corrected for the amplification and the damping of the cable and is plotted against the harmonic number. The values for the input resistance of the amplifier $R = 50\ \Omega$ and the capacity of the pick-up, amplifier $C = 85$ pF and length L of the pick up ($L = 462\,\text{mm}$) are well known. The data were fitted with the remaining fit parameter κ (red line in Fig. 80). The ratio of the κ obtained through the data fit and the theoretical value κ_{theo} is: $\kappa/\kappa_{theo} \approx 4.13$ [262]. As can be seen in Fig. 80, the theory accurately describes the characteristics of the harmonic spectrum. At the harmonic number $n = 6$ an increased Schottky power is visible, which can be described by the interaction of the stored ion beam with the rf-resonator, whose eigenfrequency was set to $6 \cdot f_0$. Each strip line of the Schottky pick-up is connected to a hybrid circuit via 50 Ω amplifiers (compare Fig. 81). The hybrid circuit adds and subtracts the four input signals to generate a horizontal, vertical and normal Schottky spectrum. The transverse Schottky signal can be used to

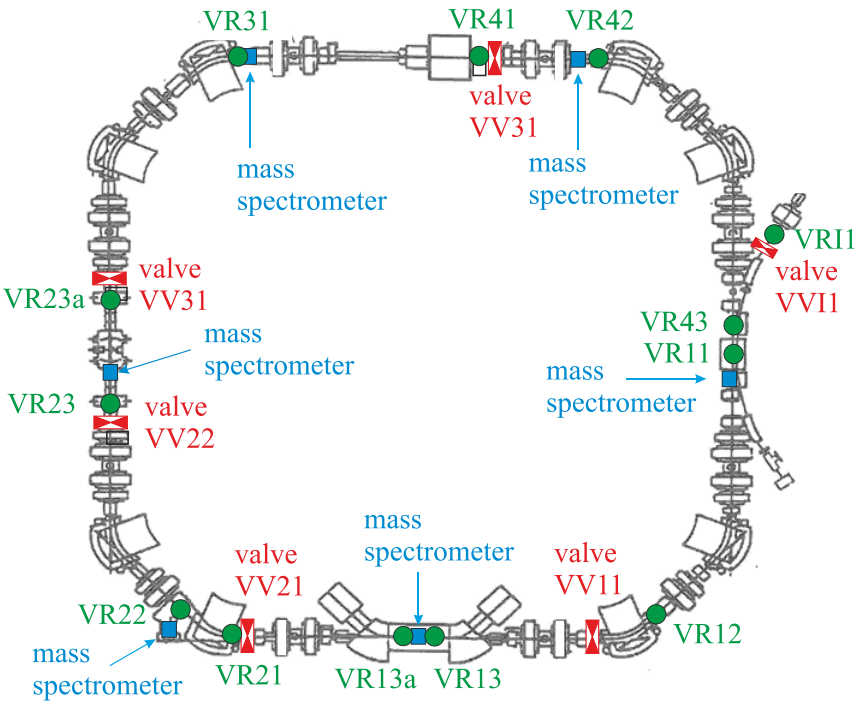

Fig. 82. Location of valves, vacuum measurements and mass spectrometers.

detect transversal coherent oscillations of the stored ion beam at high intensities, as well as the tune of the storage ring can be determined by analyzing the position of the two sidebands in the transversal Schottky spectrum.

4.12 The vacuum system

In order to achieve lifetimes for highly-charged ions in the minute range the whole vacuum system has to baked out up to 300 °C. For that purpose each vacuum component is provided with heating elements, thermo elements and heat isolation. To guarantee a constant temperature the temperature is regulated with an out-baking controller. In total the whole storage ring is equipped with 19 out-baking controllers. Each controller has 16 channels, where one channel is connected with a heater and one thermo element to measure the temperature. In total more than 300 thermo elements and heaters are used to bake-out the whole storage ring. The vacuum system is sub-divided with all-metal gate valves, compare Fig. 82 in 5 sections. In the storage ring itself 5 pneumatic controlled all-metal gate valves from VAT with nominal bore of 200 mm are used. Each vacuum section is equipped with one mass spectrometer and several "Bayard-Albert" high vacuum gauges from the company SVT able to measure vacua in the $10^{-7} - 10^{-12}$ mbar range. To pump down the storage ring from air pressure to the 10^{-5} mbar region all vacuum sections are connected via all-metal angle valves with pumping stations. The whole storage ring is pumped with approximately 30 ion getter pumps and approximately 40 titanium sublimation pumps. The

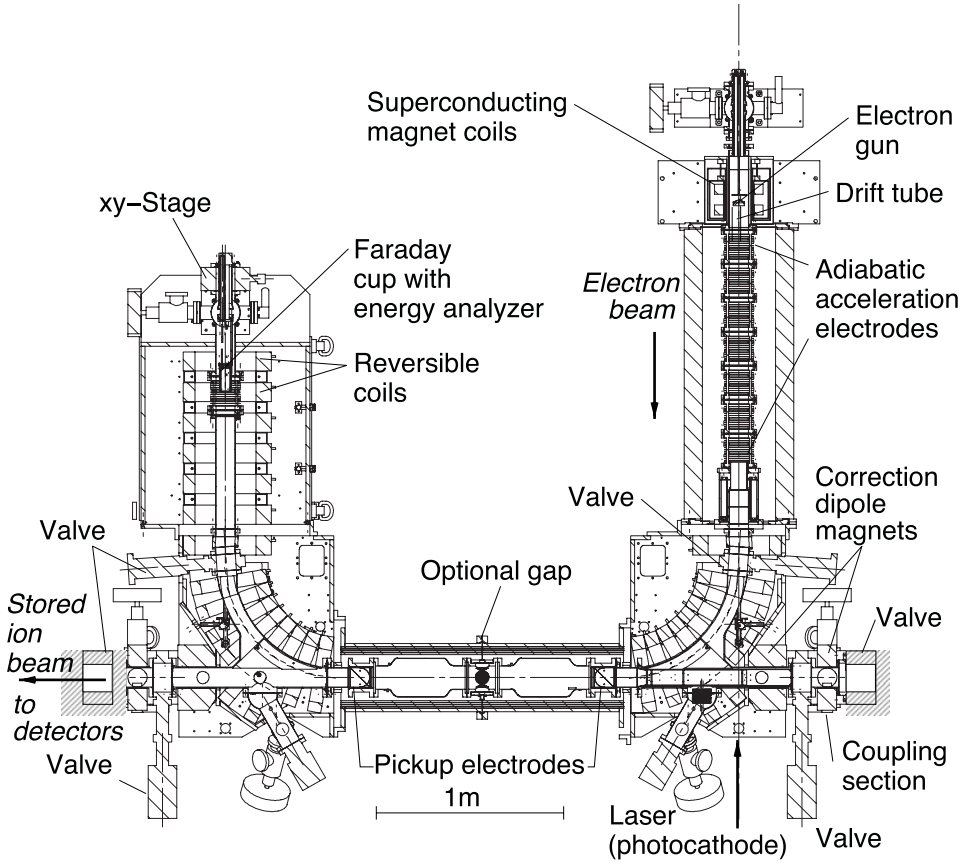

Fig. 83. ETS magnetic and vacuum system in the thermocathode configuration [170].

pumping speed of each ion getter is 60 l/s. In the electron cooler two ion getter pumps with pumping speed of 400 l/s are used. In the electron cooler additional NEG pumps ST 707 (SAES Getters) are utilized, compare Fig. 45.

4.13 The electron target

4.13.1 The Electron Target Section (ETS)

The electron target section (ETS) of the TSR, shown in Fig. 83, offers an independent merged electron beam dedicated for collision studies on atomic and molecular ion beams.

It produces a magnetically guided electron beam, using a similar arrangement as described in Sect. 4.6.1 for the electron cooler. The standard version [170] includes a thermionic cathode for which the transverse electron temperatures down to $\sim 4\,\mathrm{meV}$ were observed and which was operated at beam energies up to $\sim 7\,\mathrm{keV}$ and at currents of the order of 100 mA [263]. The ETS was complemented by a photocathode electron source [171,264], yielding transverse electron temperatures down $\sim 1\,\mathrm{meV}$ at a beam current up to $\sim 1\,\mathrm{mA}$. Here, typical operation energies are below 1 keV.

The ETS is a module installed on precision rails in the experimental section of the TSR. This arrangement offers the option of exchanging the ETS with another

station, such as a gas jet target or a laser interaction section. The stations on the rail system keep their alignment in the exchange procedure with the help of precision anchors at the in-ring and the parking positions.

The ETS vacuum system is separated from that of the TSR ring on either side by a lock system consisting of two bakeable gate valves. It can be moved on the rails under UHV and after its re-installation in the TSR only the short lock regions ($\sim$ 40 cm) must be baked. The ETS has its own self-consistent control system and a small high-voltage platform mounted above the gun magnet. Some power supplies (not all available for future use at ISOLDE) are installed at remote positions.

The photocathode system will not be available for use at ISOLDE and therefore has to be re-built if required. The thermo-cathode will be available for use at ISOLDE. The ETS includes two position pickup stations, suitable for both the ion and the electron beam, of which only one is presently operational.

4.13.2 Charge-changing detector

Behind the dipole magnet downstream of the ETS the MIDAS charge changing detector is installed. It uses [263,265] a Cerium YAG scintillation crystal (18×18 mm) read out by a photomultiplier installed $\sim$ 10 cm below the detector via a light guide. The detector is installed in a large-volume dipole chamber on a $\sim$ 1.6 m linear translation unit, by which it can be moved to both sides of the stored ion beam. The relative change of the charge(Q)-scaled momentum, p/Q, for off-beam ions at the detector position is near 50%.

4.13.3 Detector for molecular physics experiments

Around the dipole magnet downstream of the ETS additional vacuum ports exist [265] for connecting detectors for products with larger p/Q change and those for which the ion charge changes sign. Moreover, in the extension of the straight section a 100 mm diam. connection exists for neutral fragments from the experimental section. Rapid switching under UHV is possible between two output flanges, using a large bellow chamber. The straight output port is followed by the $\sim$ 8 m long time-of-flight detection beamline for molecular fragmentation products, BAMBI [266]. After an $\sim$ 2 m large-diameter vacuum transition region (100 mm diam.) an unbaked vacuum zone at $\sim 1 \times 10^{-9}$ mbar is operated, where experimental detectors for imaging neutral molecular fragments [266,267] can be installed.

4.14 An internal gas target

Dense internal gas-jet targets are presently not in operation in the TSR. Routinely employed here are the so-called reaction microscopes (for more details see Ref. [268]), with thicknesses of the jet target in the 10^{10} atoms/cm^2 region, which however are too low for the reaction experiments proposed here. The latter require targets with thicknesses of $\sim 10^{14}$ atoms/cm^2 for light gases as H_2, d, ^{4}He, and ^{3}He (see e.g. Sect. 2.7.2).

Suitable internal targets are presently being developed for the SPARC and EXL experiments in the ESR as well as for the future storage rings of FAIR facility [269]. The design of the future internal target station consists essentially of a high-power closed cycle cryostat that can be operated down to temperatures where condensation of He occurs ($\sim$ 4 K). The target beam is formed by expanding the desired target

Fig. 84. Layout of the new target inlet chamber design with the existing interaction chamber and target dump system for the ESR in Darmstadt.

gas at defined source conditions (temperature T_0 and pressure p_0) into vacuum. The use of micrometer-sized nozzles with two different geometries (pinhole orifice nozzle or trumpet-shaped nozzle) in addition to the large range of operating parameters ($T_0 = 4 - 300$ K and $p_0 \leq 100$ bars) offers the possibility to produce target beams using a large variety of gases (H_2, He, N_2, Ar, Kr, Xe) at target densities adjustable over several orders of magnitude from 10^{10} up to 10^{14} atoms/cm^2. A new inlet chamber design will significantly reduce the distance between the nozzle exit and the interaction point with the ion beam (to $\sim$ 400 mm) and moreover involve exchangeable skimmers with different aperture diameters in order to realize variable target beam interaction lengths down to $\sim$ 1 mm. A draft of a possible layout for the new target station based on the existing ESR interaction chamber and target dump system is shown in Fig. 84.

A design study for the integration of the internal target in a recoil detector setup for reaction studies is presently under investigation for the EXL project. The prototype of the new internal target source was implemented at the existing ESR target station in 2008. The maximum target densities were experimentally evaluated for different gas species during numerous experimental campaigns, i.e. the target densities for the low-Z gases were successfully improved by orders of magnitude by applying a pinhole orifice nozzle and producing a micro-droplet target beam at cryogenic temperatures [270].

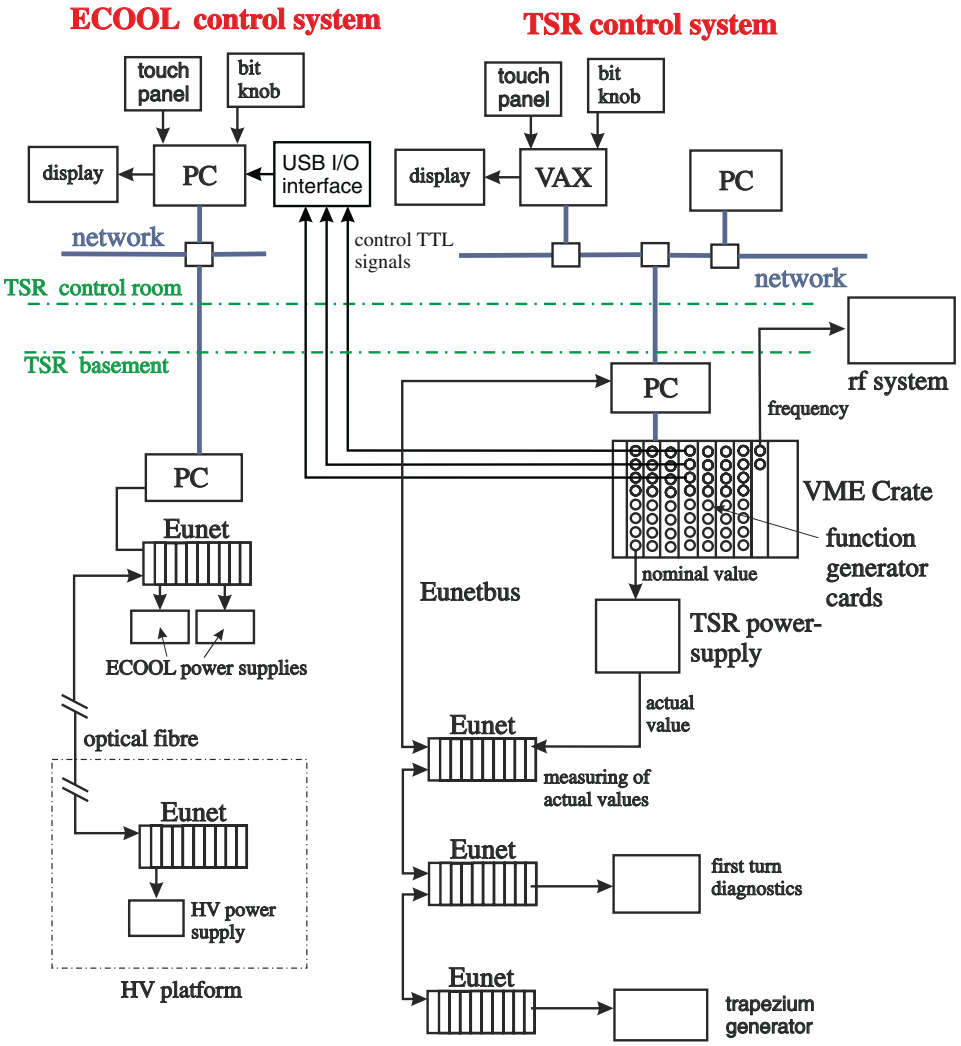

Fig. 85. The TSR control system.

Measurements with an internal target, consisting of near-liquid density hydrogen droplets, have been performed at the ESR at GSI in the recent years, where target densities of $\sim 10^{15}$ atoms/cm^2 have been achieved [91]. We note, that the size of these liquid droplets is of the order of 1 μm.

Since no internal target is presently available for the TSR, a dedicated gas-jet target will have to be constructed for the experiments at ISOLDE.

4.15 The control system

In this section the control system of the TSR is described. An overview of the control system is shown in Fig. 85. The most significant part of the control system is the VME Crate with the DAC and function generators cards. These cards, consisting of eight analog output channels with 16 bit resolution, are designed and constructed at MPIK. All output channels are optically isolated. Each function

generator card has a signal processor ADSP2181 on board used for programming the functions for acceleration and deceleration. The temperature drift of the cards are below 1 ppm/°C. Also located in the VME Crate of the TSR control system is a two-channel synthesizer VME-DDS card which generates the frequency f_{rf} of the rf system as well as a signal with a frequency of $f_{rf}+2.777$ kHz used in the beam position system. The frequency f_{rf} can be set up in the range between 0 and 10 MHz in 0.023 Hz steps. The data base of the TSR control system is located in a VAX computer. The VAX and the VME crates, with the function generator cards, are connected via a network. Touch panels as well as bit knob are used for the data input. For the data logging Eunet is used. Eunet is a bus system which was developed at MPIK and is used to control and readout the power supplies. For this purpose DAC and ADC modules with a resolution up to 16 bit are used. Digital output modules in the Eunet crates are utilized to control the drives for the quartz plates used for the first turn diagnostics. Specially designed opto-converter modules in the Eunet crates allows the control of power supplies located at the high voltage platform of the electron cooler. In the deceleration process several cooling steps are required, this means the electron cooler has to operate at different setting during the deceleration cycle. This requires an expansion of electron cooler control system. To enable a cooler operation at different settings a USB I/O card is added to the ECOOL user interface computer (compare Fig. 85), containing the database of the electron cooler settings. The USB I/O card is connected via three control cables with function generators of the TSR control system. This function generator creates TTL control signals. If one of the three control signals is changing its value the ECOOL computer is loading a new data base, where the number of the new data base is given by the TTL values of the three control signals.

5 General infrastructure and supplies

5.1 Assembly and installation procedure

The TSR storage ring has been operated for more than 20 years at MPIK-Heidelberg. The original lattice setup essentially was preserved, however several additions and modifications were implemented to accommodate new experimental setups:

- Fan-type dipole chambers;
- Extraction beamline;
- BAMBI time-of-flight beam-line;
- Laser interaction zone;
- e-target section;
- COLTRIMS with MOT arrangement.

A precision rail system allows to interchange the last three systems within one week.

The main components of the TSR cover a quadratic floor space of about $16\times16\,\mathrm{m}^2$. Two large 45° deflection magnets are positioned in each corner of the square. To allow a beam height of 177 cm the dipoles are supported by rectangular blocks of concrete with dimensions of $110\times150\,\mathrm{cm}^2$ and 75 cm height. Three adjustable feet of 20 cm height are used for lateral and height adjustment. All other components are supported by individual steel posts or pairs of massive steel rails parallel to the beam axis. Because of weight and size of the components the TSR has to be completely disassembled before transportation. Without vacuum chamber and copper coils the laminated iron yoke of one dipole has a weight of approximately 11 t. For assembly a loading zone fully accessible with a 40 t truck with a 15 t overhead crane would be

highly desirable in order to place the dipoles near their final position immediately on arrival. An overhead crane with 25 t capacity would be advisable if the electron cooler assembly including the main solenoids, gun, collector and toroids should be removed or inserted as one complete unit, as has been practiced at MPIK. The installation of the TSR at HIE-ISOLDE should be relatively straightforward if no changes to the lattice or experimental setups are required, as practically all parts are existing in a useable form. However, all copper gaskets and screws have to be renewed because of previous bake-outs.

It is highly advisable to carefully document and mark all hardware parts during disassembly for future use. The disassembly and reassembly shall be done by specialists from MPIK and ISOLDE in a joined effort to perform the work in the most efficient and qualified way.

The assembly and installation of the TSR could be done in the following steps:

- Grid definition for alignment;
- Placement of the concrete support blocks (original or new for different beam height);
- Placement of the dipoles (transportation could be made with mounted coils);
- Alignment of dipole yokes;
- Placement of support structures;
- Placement of quadrupoles and sextupoles (vacuum chambers removed);
- Alignment of all magnets;
- Installation of magnet coils and chambers;
- Installation of pumps;
- Installation of diagnostic sections;
- Leak tests;
- Electrical wiring of magnets and ancillary equipment;
- Installation of bakeout heating equipment and insulation;
- Bakeout of vacuum system;
- Leak testing;
- Injection tests.

Special attention should be paid to the location of the power supplies, the routing of the cable trays and the position and number of floor penetrations to minimize cabling costs and efforts. Several magnets are connected in series to reduce the number of power supplies. This is essentially true for all dipoles, some quadrupoles and correction dipoles of the electron cooler. At MPIK the main power supplies are installed at a floor level underneath the experimental area, which is at ground level. Cable trays are mounted near the ceiling of the basement running in parallel to the ring to minimize cable length and losses. The same is true for the pipes for the cooling water for magnets and power supplies.

5.2 Alignment

Great care has originally been exercised by professional surveyors to align the dipole magnets to the design axis better than 0.1 mm using optical theodolites. Provisions are made to be able to check the alignment after installation of the vacuum chambers without breaking the vacuum.

One precision template with pneumatic compression cylinders was mounted to the gap of each dipole using the mechanical edges of the poleshoes as references. Thus, two target points defining beam entrance and exit were defined at beam height level.

High-precision carrier plates with 6 target positions are permanently mounted on top of each dipole magnet yoke. A transfer measurement has been made from beam

level to the top level targets which later on have been used to align all dipoles to the required accuracy. All target points and adapters used are still available. However, with contemporary laser tracker technique it will be more convenient to fabricate a few adapters for laser tracker mirror balls which will be mounted to the existing target holders. Alignment of the dipoles then can be easily made using the top level target positions and in case of doubts the transfer from beam height to top level can be checked.

All other small dipole magnets, lenses, steerers were optically aligned with standard telescopes and glass targets on beam axis (Taylor Hobson, 2 1/4" diameter). These alignments have to be made without vacuum chambers, which means that quadrupoles and sextupoles have to be disassembled after the alignment procedure to install the chambers. The vacuum chambers of the quadrupoles are to be aligned separately.

The deflection magnets in the injection and extraction beam line can be aligned using optical targets which can be mounted to target holders on top of the iron yokes about 50 cm above beam height. Four permanent fixtures can be used to define entrance and exit beam position and direction. Some magnets are equipped with consoles to mount optical targets at beam level outside the vacuum chamber, which are preferred when available for practical reasons.

5.3 Media requirements

5.3.1 Electricity

The TSR-magnet system consists of a set of normally conducting C-type magnets. All magnet yokes are built from laminated steel cores and can be operated in DC or ramped mode. Ramping can be made to accelerate or decelerate the stored ion beams, however, with present power supplies only a relatively slow ramping speed is possible (a few seconds from Min to Max). Recuperation of electric power has not been tried.

The large apertures needed for high acceptance require high magnetic flux values. The electrical power needed to operate the TSR depends on the magnetic rigidity which is limited to 1.5 Tm. At the highest field level about 0.9 MW electrical power is needed (including beam transport).

The addition of input power ratings of all magnet power supplies ends at 2.2 MW, however, some power supplies are overrated for their present application or are built to allow a flexible use for different loads in case of a failure.

Essentially three types of power supplies from four different manufacturers are in use:

- Foeldi/Switzerland for dipoles and quadrupoles;
- Bruker/Germany for septa and deflectors;
- Danfysik/Denmark for solenoids and toroids;
- Kepco /USA small current supplies for correction coils and steerers.

In addition, some older types of Danfysik power-supplies are in use for the beam line dipoles and quadrupoles.

Figure 86 shows a list of the types of power supplies installed at present at the TSR, electron cooler and e-target. Nominal output parameters, their rated maximum connection power values and normal maximum settings are given, when much different from nominal values. In addition the water cooling specifications are listed. The 12 bipolar 10 A/20 V and 8 unipolar 50 A/8 V Kepco power supplies for correction coils and steerers do not need water cooling. They are not included in the table, as a future in house use is under consideration.

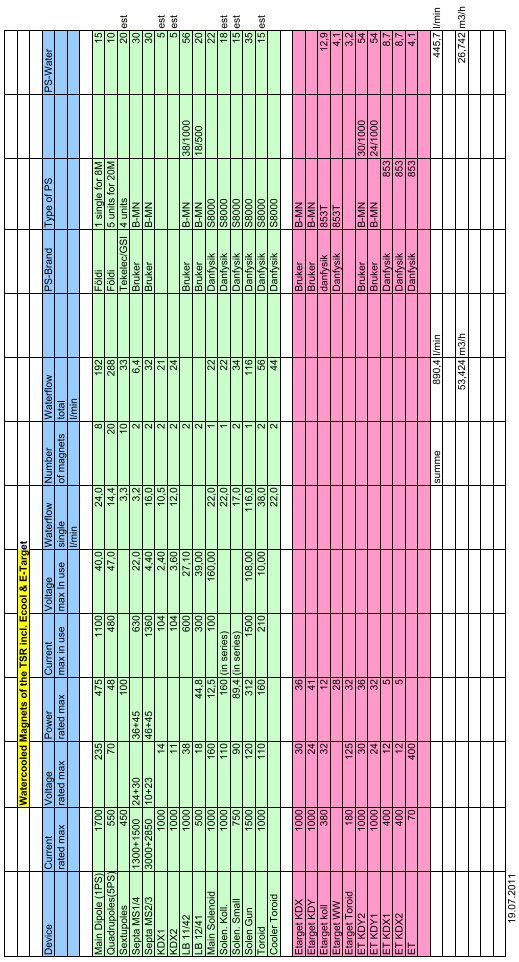

Watercooled Magnets of the TSR incl. Ecool & E-Target													
Device	Current rated max	Voltage rated max	Power rated max	Current max in use	Voltage max in use	Waterflow single l/min	Number of magnets	Waterflow total l/min	PS-Brand	Type of PS		PS-Water	
Main Dipole (1PS)	1700	235	475	1100	40,0	24,0	8	192	Fröhl	1 single for 8M		15	
Quadrupoles(5PS)	550	70	48	480	47,0	14,4	20	288	Fröhl	5 units for 20M		10	
Sextupoles	450		100			3,3	10	33	Tekelec/GSI	4 units		20	est
Septa MS1/4	1300+1500	24+30	36+45	630	22,0	3,2	2	6,4	Bruker	B-MN		30	
Septa MS2/3	3000+2850	10+23	46+45	1360	4,40	16,0	2	32	Bruker	B-MN		30	
KDX1	1000	14		104	2,40	10,5	2	21				5	est
KDX2	1000	11		104	3,66	12,0	2	24				5	est
LB 11/42	1000	38		600	27,10		2		Bruker	B-MN	38/1000	56	
LB 12/41	500	18	44,8	300	28,00		2		Bruker	B-MN	18/500	28	
Main Solenoid	1000	160	12,5	100	160,000	22,0	1	22	Danfysik	S8000		22	
Solen. Koll.	1000	110	160 (in series)			22,0	1	22	Danfysik	S8000		18	est
Solen. Small	750	90	89,4 (in series)			17,0	2	34	Danfysik	S8000		15	est
Solen. Gun	1500	120	312	1500	108,00	116,0	1	116	Danfysik	S8000		35	
Toroid	1000	110	160	210	10,00	38,0	2	56	Danfysik	S8000		15	est
Cooler Toroid						22,0	2	44	Danfysik	S8000			
Etarget KDX	1000	30	36						Bruker	B-MN			
Etarget KDY	1000	24	41						Bruker	B-MN			
Etarget coil	360	32	12						Danfysik	8537		12,9	
Etarget WW			288						Danfysik	8537		4,1	
Etarget Toroid	180	125	32									3,2	
ET KDY2	1000	30	36						Bruker	B-MN	30/1000	54	
ET KDY1	1000	24	32						Bruker	B-MN	24/1000	54	
ET KDX1	400	12	5						Danfysik		853	8,7	
ET KDX2	400	12	5						Danfysik		853	8,7	
ET	70	400							Danfysik		853	4,1	
							summe		890,4 l/min			445,7	l/min
									53,424 m3/h			26,742	m3/h
19.07.2011													

Fig. 86. Power and Cooling Specifications of TSR-Power Supplies in Heidelberg.

5.3.2 Space requirements

Due to different manufacturers the form factors of the power supplies vary greatly in width and in depth, however, when lined up, they would need a front length of 29 m floor space for TSR and additionally length of 7 m for the e-target in the basement. For ancillary electronics near the power supplies (controls, steerers etc) space for 10 standard 19" racks would be necessary, 3 additional racks are in use on a small insulated platform for the electron cooler inside a shielded HV-cage with dimension of about $4 \times 4\,\mathrm{m}^2$. At TSR ground-level additional floor space is needed for vacuum control (4 racks), rf-control (3 racks), fast bumper-switches (6 racks), diagnostics (1 rack) and bake out controls (5 racks). In total space for 13 racks are needed in the basement and 19 standard racks at ground floor level.

The additional needs for injection and extraction beam line have not been included, though magnets and power supplies would be available, too.

According to the space requirements for the installation of the TSR (see specifications in Sects. 5.1 and 5.3.2), a dedicated building would be needed to accommodate the TSR, the magnet power supplies, and the new experimental areas. The TSR ring itself requires a $20 \times 20\,\mathrm{m}$ hall. In addition, some space is needed for the installations

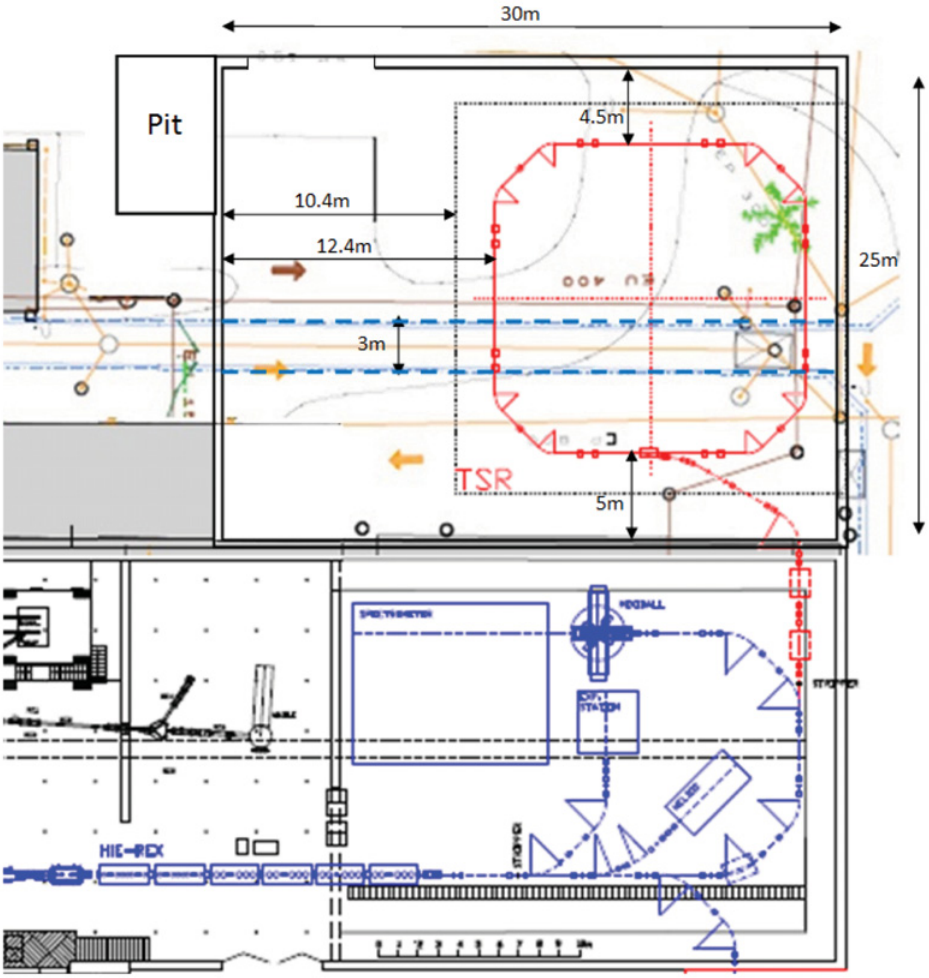

Fig. 87. A possible location of the TSR building at CERN. Shown is the Jura (West) side of the existing ISOLDE building Nr. 170. The TSR building would be built on top of a service tunnel (indicated with blue dashed lines). The injection beam-line from the HIE-ISOLDE (red color) is tilted to account for the level difference. The beam-line for slowly-extracted beams to the experimental setups is shown in Fig. 88. The final position of the ring and beam-lines inside the building as well as the exact dimensions of the building have still to be defined. The basement can be used to house the power supplies, racks with electronics, etc.

of internal targets, detectors, etc. A possible site for such a building is on the Jura (west) side of Building 170 (ISOLDE), which is illustrated in Fig. 87. The construction of the building at this place is feasible and offers several advantages, like, e.g., the space in the basement (service tunnel) can be partially used to install racks and various power supplies. Furthermore, there is a significant amount of space available for in-ring installations and experimental setups. The only disadvantage of this solution is the difference in levels of the HIE-ISOLDE beam-line and the TSR, which would require a tilted beam-line from the HIE-ISOLDE hall for the injection into the TSR (these beam line is taken into account in Fig. 87 and the tilted injection line is clearly seen in Fig. 89). Possible beam line for slowly-extracted beams from the TSR is illustrated in Fig. 88.

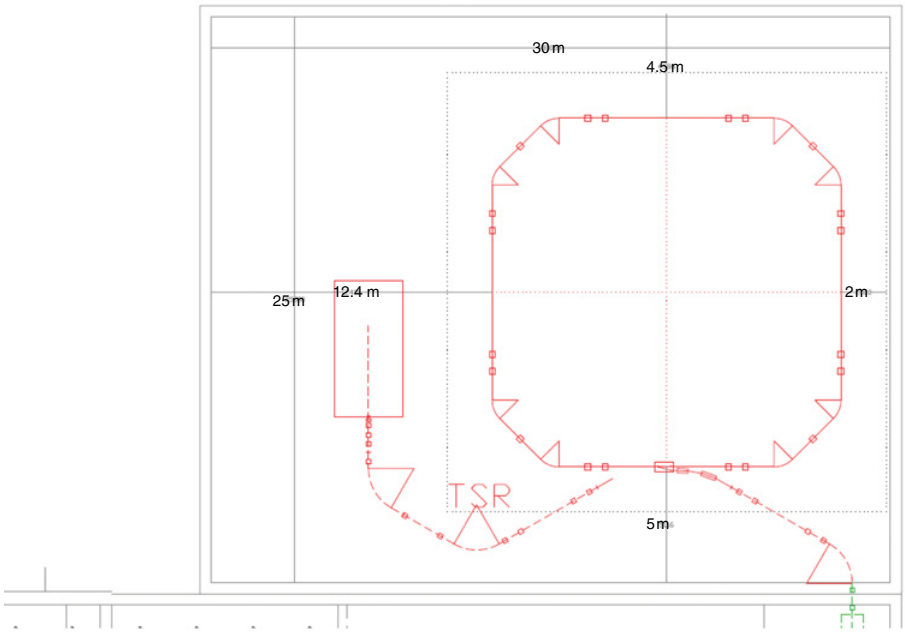

Fig. 88. Possible location on the TSR inside the building. The presently considered dimensions are indicated. The beam-line for slowly-extracted beams to external experimental setups is shown as well. We note, that although this arrangement allows for a convenient access to different components of the TSR, the final position of the ring and beam-lines inside the building still have to be defined.

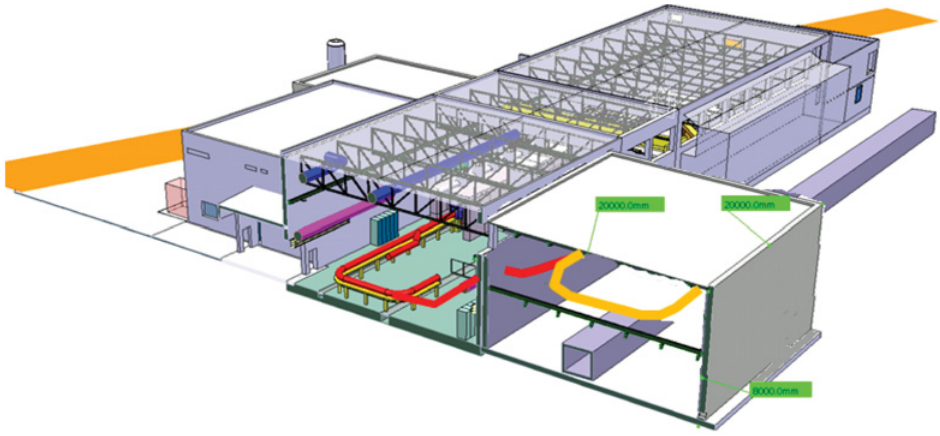

Fig. 89. The same as Fig. 87 in 3D representation. The service tunnel, the offset in the beam-line levels and the required tilted beam-line, connecting the HIE-ISOLDE (indicated in red color) and the TSR (indicated in orange color), are clearly seen. Furthermore, the French-Swiss border is shown by an orange line.

Another technically feasible location of the TSR building could be on the Saleve (east) side of the ISOLDE building, behind the new Buildings Nr. 198 and Nr. 199. However, this would require very long beam-lines from/to the HIE-ISOLDE hall. Furthermore, in this case the TSR building need to be built over the French-Swiss border (see Fig. 89).

5.3.3 Cooling water

Magnet coils and power supplies are water cooled using a system capable of supplying about 130 m^3/h of deionized water with a pressure of 8 bar and a temperature of less than 30 °C. The conductivity of the water supplied by a water softening stage and a reverse osmosis unit is basically better than 8 μS, however, as our system has an open return line and buffer tank the pH-value is kept near 8 by injecting NaOH leading to an effective conductivity of 60 μS. Thus, the CuO contents of the water can be kept below 0.2 mg/l using an ion exchange column in a bypass to the main loop. A weak passivation of the surfaces by Nalco 73199 (Sodium Benzotriazole) is made additionally. Corrosion of electrical or hydraulic connections due to leakage currents to ground or blocking of cooling channels by accumulated CuO is efficiently avoided since many years. This specially needed water treatment could be avoided with a closed water circuit with sufficiently low conductivity. Table 6-1 also shows the water flow rates of the individual magnets or power supplies as specified by the manufacturers.

A few devices presently installed at the TSR need lower temperature cooling water. Turbo-pumps at the injection and extraction line need a few l/min of 16–20 °C water, however occasionally air cooling with a fan is sufficient. Some closed cycle cryo-compressors demand for 20 °C-water (5 kW) and also one high power solenoid at the electron cooler cannot be operated at highest field if connected to the 30 °C water line.

5.3.4 Air conditioning

No temperature controlled environment is needed for the TSR-equipment. Sufficient air circulation is anticipated to keep the ambient temperature for the power supplies in the basement below or near 30 °C. A few locally cooled electronic racks would be desirable e.g. for the networking control PC and the 16-bit VME DACs for the magnet currents as well as the HV-power supplies of the electron cooler/e-target system which directly influences the resolution of experimental data.

5.3.5 Pressurized air, nitrogen, vacuum exhaust

Small amounts of dry, oil-free pressurized air of minimum 7 bar are continuously needed to control vacuum valves and pneumatic actuators of the TSR and injection line.

Occasionally somewhat larger amounts of pressurized air are needed to thermally protect the laminated, glued magnet yokes during bake out of the dipole vacuum chambers. A pressure of 2 bar and a continuous stream of about 20 m^3/h of air is considered to be sufficient to prevent the magnet poleshoes from overheating.

A supply line of dry nitrogen would be helpful for venting the vacuum chambers for access or servicing as the pumping speed during the consecutive pump down is considerably higher with less water on the surfaces.

A fan supported exhaust for all roughing and fore pumps should be installed. No dangerous or corrosive gases are to be expected from the TSR vacuum pumps.

5.4 Safety

The TSR at HIE-ISOLDE will not bring new risks to the ISOLDE Facility. The risk identified at the TSR are similar to those present in the existing ISOLDE experimental

area. Nevertheless, as a new installation, the TSR project will have to include all safety elements based on CERN Safety rules, Host States regulations, European Directives, international standards and best practices.

The following subsections describe the main safety issues that have already been identified. The TSR@ISOLDE project leader will have to provide a safety file [271] to the HSE unit in order to obtain final clearance to operate the TSR at CERN.

5.4.1 Radiation protection

The main function of the TSR is to accumulate low-energy heavy ions coming from HIE-ISOLDE (10 Mev/u). It may also be used to accelerate very low-intensity radioactive ion beams. Under these conditions the radiation levels during TSR operation may be considered as negligible.

At present, the facility is operated at MPIK, Heidelberg and is accessible when the TSR is running with the exception of restricted access to the machine when beams are injected.

The major concern from a radiological point of view will be the potential contamination of the machine due to long-lived isotope storage. The control and authorisation from the Radiation Protection Officer (RPO) will be needed prior to the intervention on any vacuum chamber or equipment of the TSR. It is already a common approach at ISOLDE due to the presence of potential contaminated transfer lines or equipment.

The TSR will require an extension of the radiation monitoring system RAMSES, a specific access system and extra RPO resources. It may also have an impact on radioactive waste production.

In any case, the TSR shall comply with the CERN Code F "Radiation Protection" [272].

5.4.2 Mechanical protection

As a storage ring, the TSR shall comply with the requirements of the Machinery Directive 2006/42/EC and the following CERN Safety rules: "Safety Regulation on mechanical equipment (SR-M)" [273].

The TSR shall be tested, inspected and proven to be conform with these rules prior to its first operation.

5.4.3 Electrical protection

All electrical installation and equipment used by the TSR shall comply with the Safety Code C1 [274]. All electrical equipment not compliant with these standards shall be replaced by a conform equipment during the installation phase.

Electrical emergency stops on electrical equipment or buildings shall be available when needed.

The TSR shall be tested, inspected and proven to be conform with these rules prior to its first operation.

5.4.4 Fire prevention

In order to reduce the fire hazard and its consequences, material used in electrical installations and equipment shall comply with CERN safety Instruction IS23 [275] and IS41 [276].

All material used in electrical installations and equipment not compliant with these standards shall be replaced by a conform equipment during the installation phase.

The ISOLDE facility will require an extension of the fire detection and alarm system already in place in the experimental area.

5.4.5 Cryogenics

The TSR is equipped with an electron target, where the gun solenoid is superconducting cooled with liquid helium. The liquid He consumption is around 10 l per 24 h. Due to the small quantity of liquid helium, there is no oxygen deficiency hazard linked to the presence of cryogenic liquid. Ideally, the liquid He line should be an extension of the future cryogenic installation foreseen for the HIE-ISOLDE SC Linac.

In any case the TSR shall comply with the CERN IS 47 [277].

5.5 Data acquisition systems and control room

Since the radiation level during the TSR operation can be neglected, the racks for the data acquisition electronics can be placed next to the detector setups at the TSR.

There are no special requirements for the control room and, as for other experiments at ISOLDE, the main ISOLDE control room can be used for tuning the TSR experiments.

6 TSR@HIE-ISOLDE Collaboration

The present proposal on a storage ring facility at HIE-ISOLDE brought together 131 scientists from 51 institutions located in 18 countries, who form the TSR@HIE-ISOLDE Collaboration.

The organization of the collaboration foresees the following administrative posts: a Spokesperson and two Deputy Spokespersons, the Physics Coordinator and a Deputy Physics Coordinator, a TSR Technical Coordinator and an ISOLDE Technical Coordinator, an ISOLDE Contact Person, and an HIE-ISOLDE Contact Person. At the time of submission of the present proposal, these positions are filled as follows:

Spokesperson	Klaus Blaum
Deputy Spokesperson	Riccardo Raabe
Deputy Spokesperson	Phil Woods
Physics Coordinator	Peter Butler
Deputy Physics Coordinator	Yuri A. Litvinov
TSR Technical Coordinator	Manfred Grieser
ISOLDE Technical Coordinator	Erwin Siesling
ISOLDE Contact Person	Yorick Blumenfeld/Maria Borge
HIE-ISOLDE Contact Person	Fredrik Wenander

Furthermore, the collaboration has a Board which consists of the persons serving at the above administrative posts and of two conveners from each of the physics cases

proposed in the present proposal. At the time of submission of the present proposal, the following were serving as conveners:

Reaction Experiments	Peter Egelhof & Dennis Mücher
Atomic Physics Experiments	Daniel Savin & Stefan Schippers
Astrophysics Experiments	Shawn Bishop & Rene Reifarth
Neutrino Experiments	Thierry Stora & Cristina Volpe
Atomic Effects on Nuclear Lifetimes	Fritz Bosch & Takayuki Yamaguchi
Isomeric Beam Experiments	George Dracoulis & Phil Walker
Dielectronic Recombination on Exotic Nuclei	Carsten Brandau & Andreas Wolf
Laser Spectroscopy	Kieran Flanagan & tba.

TSR@HIE-ISOLDE is an open collaboration and new conveners will join in the Board if new physics cases are proposed at a later time.

In order to pursue the physics goals presented in this TSR@HIE-ISOLDE Proposal, several R&D studies have to be done. Therefore, several dedicated working groups have been suggested which are listed below together with the main institutions which hold the necessary expertise and would participate in the corresponding R&D work.

Working Group	Participating Institutions
Electron Cooler / Electron Target	MPIK / Uni Giessen / CERN
Gas Target	MPIK / Uni Frankfurt / UK Universities
Diagnostics	MPIK / GSI
Setup & Commissioning	MPIK / CERN
Control System	CERN
Particle Detectors	TU Darmstadt / TU Munich / GSI / KU Leuven / UK Universities
EBIT/S & Injection / Extraction	MPIK / CERN

We would like to thank the Max-Planck-Society, the ISOLDE Collaboration and the ISOLDE Technical Team for their strong support in the preparation of the TDR and the realization of this project. This work has been supported by the UK STFC, AWE plc, BMBF grant in the framework of the Internationale Zusammenarbeit in Bildung und Forschung Projekt-Nr. CHN 11/012, and by the Helmholtz Alliance Program of the Helmholtz Association, contract HA216/EMMI "Extremes of Density and Temperature: Cosmic Matter in the Laboratory".

References

1. B. Franzke, H. Geissel, G. Münzenberg, Mass Spectr. Rev. **27**, 428 (2008)
2. Yu.A. Litvinov, F. Bosch, Rep. Prog. Phys. **74**, 016301 (2011)
3. Yu.A. Litvinov, et al., Acta Phys. Polonica **41**, 511 (2010)
4. Ion Storage Ring TSR, `http://www.mpi-hd.mpg.de/blaum/storage-rings/tsr/index.en.html`
5. D. Krämer, et al., Nucl. Instr. Meth. A **287**, 268 (1990)
6. V.S. Nikolaev, Sov. Phys. Usp. **8**, 269 (1965)
7. I.S. Dmitriev, V.S. Nikolaev, L.N. Fateeva, Y.A. Teplova. Sov. Phys. JETP **15**, 11 (1962)
8. National Nuclear Data Center, `http://www.nndc.bnl.gov`
9. T. Ohtsuki, et al., Phys. Rev. Lett. **98**, 252501 (2007)
10. V. Kumar, et al., Phys. Rev. C **77**, 051304R (2008)
11. J.N. Bahcall, R. Ulrich, Rev. Mod. Phys. **60**, 297 (1988)

12. I. Iben Jr., K. Kalata, J. Schwartz, Astroph. J. **150**, 1001 (1967)
13. A.V. Gruzinov, J.N. Bahcall, Astroph. J. **490**, 437 (1997)
14. C. Arpesella, et al., Phys. Rev. Lett. **101**, 091302 (2008)
15. W. Bambynek, et al., Rev. Mod. Phys. **49**, 77 (1977)
16. L.M. Folan, V.I. Tsifrinovich, Phys. Rev. Lett. **74**, 499 (1995)
17. Yu.A. Litvinov, et al., Phys. Rev. Lett. **99**, 262501 (2007)
18. H. Geissel, et al., Eur. Phys. J. Special Topics **150**, 109 (2007)
19. N. Winckler, et al., Phys. Lett. B **679**, 36 (2009)
20. Z. Patyk, et al., Phys. Rev. C **77**, 014306 (2008)
21. K. Siegień-Iwaniuk, et al., Phys. Rev. C **84**, 014301 (2011)
22. S. Kappertz, et al., AIP Conf. Proc. **455**, 110 (1998)
23. C.W. Johnson, E. Kolbe, S.E. Koonin, K. Langanke, Astroph. J. **392**, 320 (1992)
24. C.E. Rolfs, W.S. Rodney, Cauldrons in the Cosmos (Uni. Chicago Press, 1988), p. 351
25. C.E. Rolfs (private communications)
26. W. von Oertzen, M. Freer, Y. Kanada-Enyo, Phys. Rep. **432**, 43 (2006)
27. B. Jonson, Phys. Rep. **389**, 1 (2004)
28. S. Hyldegaard, et al., Phys. Lett. B **678**, 459 (2009)
29. R. Raabe, et al., Phys. Rev. Lett. **101**, 212501 (2008)
30. X.D. Tang, et al., Phys. Rev. C **81**, 045809 (2010)
31. M.J.G. Borge, et al., Zeit. Phys. A **340**, 255 (1991)
32. K. Riisager, et al., Phys. Lett. B **235**, 30 (1990)
33. R. Raabe, et al., Phys. Rev. C **80**, 054307 (2009)
34. A. Saastamoinen, et al., Phys. Rev. C **83**, 045808 (2011)
35. D. Baye, P. Descouvemont, E.M. Tursunov, Phys. Rev. C **82**, 054318 (2010)
36. D. Baye, E.M. Tursunov, Phys. Lett. B **696**, 464 (2011)
37. H.-J. Kluge, W. Nörtershäuser, Spectrochim. Acta B **58**, 1031 (2003)
38. B. Cheal, K.T. Flanagan, J. Phys. G **37**, 113101 (2010)
39. G. Neyens, Rep. Prog. Phys. **66**, 633 (2003)
40. C. Thibault, et al., Phys. Rev. C, **12**, 644 (1975)
41. G. Neyens, et al., Phys. Rev. Lett. **94**, 022501 (2005)
42. D.T. Yordanov, et al., Phys. Rev. Lett. **99**, 212501 (2007)
43. D.T. Yordanov, et al., Phys. Rev. Lett. **108**, 042504 (2012)
44. R. Grzywacz, et al., Phys. Rev. Lett. **81**, 766 (1998)
45. S. Franchoo, et al., Phys. Rev. Lett. **81**, 3100 (1998)
46. S. Franchoo, et al., Phys. Rev. C **64**, 054308 (2001)
47. K.T. Flanagan, et al., Phys. Rev. Lett. **103**, 142501 (2009)
48. B. Cheal, et al., Phys. Rev. Lett. **104**, 252502 (2010)
49. U. Köster, et al., Phys. Rev. C **84**, 034320 (2011)
50. K. Sieja, F. Nowacki, Phys. Rev. C **81**, 061303 (2010)
51. T. Kühl, et al., Nucl. Instr. Meth. B **56/57**, 1129 (1991)
52. R. Grieser, et al., Appl. Phys. B **59**, 127 (1994)
53. R. Kirchner, Nucl. Instr. Meth. B **204**, 179 (2003)
54. F. Wenander, J. Instr. **5**, C10004 (2010)
55. P. Campbell, et al., Eur. Phys. J. A **15**, 45 (2002)
56. E. Mané, et al., Eur. Phys. J. A **42**, 503 (2009)
57. D. Rodriguez, et al., Eur. Phys. J. Special Topics **183**, 1 (2010)
58. A. Ozawa, T. Kobayashi, T. Suzuki, K. Yoshida, I. Tanihata, Phys. Rev. Lett. **84**, 5493 (2000)
59. R. Kanungo, et al., Phys. Rev. Lett. **102**, 152501 (2009)
60. C.R. Hoffman, et al., Phys Lett. B **672**, 17 (2009)
61. D. Lambert, Astron. Astroph. Rev. **3**, 201 (1992)
62. M. Arnould, S. Goriely, Phys. Rep. **384**, 1 (2003)
63. T. Rauscher, F.-K. Thielemann, At. Data Nucl. Data Tab. **75**, 1 (2000)
64. T. Rauscher, F.-K. Thielemann, At. Data Nucl. Data Tab. **88**, 1 (2004)
65. H. Schatz, et al., Phys. Rep. **294**, 167 (1998)

66. W.M. Howard, et al., Astroph. J. **373**, 5 (1991)
67. M. Kusakabe, et al., Astroph. J. **726**, 25 (2011)
68. C. Travaglio, et al., Astroph. J. (in press) http://arxiv.org/abs/1106.0582v1
69. Q. Zhong, et al., J. Phys. Conf. Ser. **202**, 012011 (2010)
70. R. Reifarth, et al., GSI Proposal (2010)
71. G. Lotay, et al., Phys. Rev. Lett. **102**, 1625202 (2009)
72. R. Diehl, et al., Nature (London) **298**, 445 (2006)
73. G. Lotay, et al., Phys. Rev. C **84**, 035802 (2011)
74. W. Tan, et al., Phys. Rev. Lett. **98**, 242503 (2007)
75. R. Sánchez, et al., Phys. Rev. Lett. **96**, 033002 (2006)
76. V.L. Ryjkov, et al., Phys. Rev. Lett. **101**, 012501 (2008)
77. B. Fornal, et al., Phys. Rev. C **70**, 064304 (2004)
78. L. Gaudefroy, et al., Phys. Rev. Lett. **97**, 092501 (2006)
79. A.N. Andreyev, et al., Nature (London) **405**, 430 (2000)
80. E. Caurier, et al., Rev. Mod. Phys. **77**, 427 (2005)
81. O. Sorlin, M.G. Porquet, Prog. Part. Nucl. Phys. **61**, 602 (2008)
82. S.M. Lenzi, F. Nowacki, A. Poves, K. Sieja, Phys. Rev. C **82**, 054301 (2010)
83. T. Otsuka, et al., Phys. Rev. Lett. **95**, 232502 (2005)
84. T. Otsuka, et al., Phys. Rev. Lett. **105**, 032501 (2010)
85. A.M. Bernstein, R.A. Miskimen, B. Quinn, S.A. Wood, Phys. Rev. Lett. **49**, 451 (1982)
86. E. Khan, et al., Phys. Lett. B **490**, 45 (2000)
87. J.P. Schiffer, W. True, Rev. Mod. Phys. **48**, 191 (1976)
88. B.P. Kay, et al., Phys. Lett. B **658**, 216 (2008)
89. B.P. Kay, et al., Phys. Rev. C **84**, 024325 (2011)
90. P. Egelhof, et al., Phys. Scripta T **104**, 151 (2003)
91. N. Petridis, et al., Nucl. Instr. Meth. A **656**, 1 (2011)
92. N. Kalantar-Nayestanaki, et al., Int. J. Mod. Phys E **18**, 524 (2009)
93. FAIR Baseline Technical Report, GSI Darmstadt, 2006
94. H. Moeini, et al., Nucl. Instr. Meth. A **634**, 77 (2011)
95. B. Streicher, et al., Nucl. Instr. Meth. A **654**, 604 (2011)
96. J. Diriken, et al., contribution to the ARIS 2011 Conference, 2011
97. Agenda of the 37$^{\text{th}}$ Meeting of the INTC on the CERN INDICO website
98. The HIE-ISOLDE spectrometer LoI to the INTC, CERN, 2010
99. W. Catford, et al., GASPARD LoI to the INTC, CERN, 2010
100. S.J. Freeman, et al., Helios LoI to the INTC, CERN, 2010
101. R. Raabe, et al., ACTAR-TPC LoI to the INTC, CERN, 2010
102. P.M. Walker, G.D. Dracoulis, Nature (London) **399**, 35 (1999)
103. G. Audi, et al., Nucl. Phys. A **729**, 3 (2003)
104. M.W. Reed, et al., Phys. Rev. Lett. **105**, 172501 (2010)
105. B. Sun, et al., Eur. Phys. J. A **31**, 393 (2007)
106. B. Sun, et al., Nucl. Phys. A **834**, 476c (2010)
107. D. Rudolph, et al., Phys. Rev. C **78**, 021301 (2008)
108. I. Stefanescu, et al., Phys. Rev. Lett. **98**, 122701 (2007)
109. P.M. Walker, J.J. Carroll, Phys. Today **58**, 39 (2005)
110. G. Gosselin, et al., Phys. Rev. C **76**, 044611 (2007)
111. A. Palffy, J. Evers, C. Keitel, Phys. Rev. Lett. **99**, 172502 (2007)
112. A. Palffy, et al., Phys. Lett. B **661**, 330 (2008)
113. J.N. Bahcall, Phys. Rev. **126**, 1143 (1962)
114. K. Takahashi, K. Yokoi, At. Data Nucl. Data Tables **36**, 375 (1987)
115. G.T. Emery, Annu. Rev. Nucl. Sci. **22**, 165 (1972)
116. Yu.A. Litvinov, et al., Phys. Lett. B **573**, 80 (2003)
117. B. Sun, et al., Phys. Lett. B **688**, 294 (2010)
118. M. Jung, et al., Phys. Rev. Lett. **69**, 2164 (1992)
119. F. Bosch, et al., Phys. Rev. Lett. **77**, 5190 (1996)
120. W. Henning, et al., AIP Conf. Proc. **126**, 203 (1985)

121. J.B. Blake, T. Lee, D.N. Schramm, Nat. Phys. Sci. **242**, 98 (1973)
122. F. Bosch, et al., GSI Proposal (2010)
123. T. Ohtsubo, et al., Phys. Rev. Lett. **95**, 052501 (2005)
124. J. Kurcewicz, et al., Acta. Phys. Polonica B **41**, 525 (2010)
125. Yu.A. Litvinov, et al., Phys. Lett. B **664**, 162 (2008)
126. J.R. Letaw, et al., Astroph. and Space Sci. **114**, 365 (1985)
127. N.E. Yanasak, et al., Adv. Space Res. **27**, 727 (2001)
128. P. Seelig, et al., Phys. Rev. Lett. **81**, 4824 (1998)
129. Yu.A. Litvinov, Int. J. Mod. Phys. E **18**, 323 (2009)
130. D.R. Atanasov, et al., Eur. Phys. J. A **48**, 22 (2012)
131. L.D. Huff, W.V. Houston, Phys. Rev. **36**, 842 (1930)
132. T. Brage, et al., Astroph. J. **500**, 507 (1998)
133. R.H. Rubin, G.J. Ferland, E.E. Chollet, R. Horstmeyer, Astroph. J. **605**, 784 (2004)
134. W. Johnson, Can. J. Phys. **89**, 429 (2011)
135. K.T. Cheng, M.H. Chen, W.R. Johnson, Phys. Rev. A **77**, 052504 (2008)
136. C. Laughlin, Phys. Lett. A **75**, 199 (1980)
137. A.D. Ludlow, et al., Science **319**, 1805 (2008)
138. T. Rosenband, et al., Science **319**, 1808 (2008)
139. T. Becker, et al., Phys. Rev. A **63**, 051802 (2001)
140. T. Rosenband, et al., Phys. Rev. Lett. **98**, 220801 (2007)
141. T. Brage, P.G. Judge, C.R. Proffitt, Phys. Rev. Lett. **89**, 281101 (2002)
142. E. Träbert, J. Phys. B **43**, 074034 (2010)
143. S. Schippers, et al., Phys. Rev. Lett. **98**, 033001 (2007)
144. E. Träbert, et al., New J. Phys. **13**, 023017 (2011)
145. M. Andersson, Y. Zou, R. Hutton, T. Brage, Phys. Rev. A **79**, 032501 (2009)
146. J. Li, C. Dong, Plas. Sci. Technol. **12**, 364 (2010)
147. P. Jönsson, M. Andersson, J. Phys. B **40**, 2417 (2007)
148. H. Kang, et al., J. Phys. B **42**, 195002 (2009)
149. M. Andersson, Y. Zou, R. Hutton, T. Brage, J. Phys. B **43**, 095001 (2010)
150. N.J. Stone, At. Data Nucl. Data Tables **90**, 75 (2005)
151. R. Schuch, S. Böhm, J. Phys. Conf. Ser. **88**, 012002 (2007)
152. A. Müller, Adv. At. Mol. Opt. Phys. **55**, 93 (2008)
153. A. Wolf, et al., J. Phys. Conf. Ser. **194**, 012024 (2009)
154. C. Brandau, et al., Phys. Rev. Lett. **91**, 073202 (2003)
155. C. Brandau, et al., Phys. Rev. Lett. **100**, 073201 (2008)
156. Y.S. Kozhedub, et al., Phys. Rev. A **77**, 032501 (2008)
157. M. Lestinsky, et al., Phys. Rev. Lett. **100**, 033001 (2008)
158. R. Schuch, et al., Phys. Rev. Lett. **95**, 183003 (2005)
159. S. Schippers, et al., Nucl. Instr. Meth. B **235**, 265 (2005)
160. C. Brandau, et al., J. Phys. Conf. Ser. **194**, 012023 (2009)
161. C. Brandau, et al., Hyperfine Interact. **196**, 115 (2010)
162. C. Brandau, et al. (unpublished)
163. H.T. Schmidt, et al., Phys. Rev. Lett. **72**, 1616 (1994)
164. A.A. Saghiri, et al., Phys. Rev. A **60**, R3350 (1999)
165. T. Radon, et al., Nucl. Phys. A **677**, 75 (2000)
166. Yu.A. Litvinov, et al., Nucl. Phys. A **756**, 3 (2005)
167. F. Nolden, et al., Nucl. Instr. Meth. **659**, 69 (2011)
168. I. Klaft, et al., Phys. Rev. Lett. **73**, 2425 (1994)
169. B.R. Beck, et al., Phys. Rev. Lett. **98**, 142501 (2007)
170. F. Sprenger, M. Lestinsky, D.A. Orlov, D. Schwalm, A. Wolf, Nucl. Instr. Meth. A **532**, 298 (2004)
171. D.A. Orlov, U. Weigel, D. Schwalm, A.S. Terekhov, A. Wolf, Nucl. Instr. Meth. A **532**, 418 (2004)
172. R.D. Hoffman, S.E. Woosley, T.A. Weaver, Astroph. J. **549**, 1085 (2001)
173. F.-K. Thielemann, et al., Astroph. J. Suppl. Ser. **281**, 25 (2002)

174. J. Vink, J.S. Kaastra, J.A.M. Bleeker, Astron. Astroph. **307**, L41 (1996)
175. C.L. Fryer, M.S. Warren, Astrophys. J. Lett. **574**, L65 (2002)
176. S. Akiyama, J.C. Wheeler, D.L. Meier, I. Lichtenstadt, Astroph. J. **584**, 954 (2003)
177. W.D. Arnett, C. Meakin, Astrophys. J. **733**, 78 (2011)
178. M. Herant, W. Benz, S. Colgate, Astroph. J. **395**, 642 (1992)
179. M. Herant, Phys. Rep. **256**, 117 (1995)
180. J.M. Blondin, A. Mezzacappa, C. DeMarino, Astroph. J. **584**, 971 (2003)
181. T. Foglizzo, P. Galletti, L. Scheck, H.-T. Janka, Astroph. J. **654**, 1006 (2007)
182. C.D. Ott, A. Burrows, L. Dessart, E. Livne, Astroph. J. **685**, 1069 (2008)
183. T.D. Brandt, A. Burrows, C.D. Ott, E. Livne, Astroph. J. **728**, 8 (2011)
184. U. Hwang, J.M. Laming, Astroph. J. **597**, 362 (2003)
185. J.M. Laming, U. Hwang, Astroph. J. **597**, 347 (2003)
186. U. Hwang, et al., Astroph. J. Lett. **615**, L117 (2004)
187. U. Hwang, J.M. Laming [arXiv:1111.7316] (2011)
188. J. Vink, et al., Astroph. J. Lett. **560**, L79 (2001)
189. M. Renaud, et al., Astroph. J. Lett. **647**, L41 (2006)
190. S. Nagataki, et al., Astroph. J. Lett. **492**, L45 (1998)
191. S. Schippers, J. Phys. Conf. Ser. **163**, 012001 (2009)
192. S. Schippers, et al., Int. Rev. At. Mol. Phys. **1**, 109 (2010)
193. M. Hahn, et al., Astroph. J. **729**, 76 (2011)
194. M. Hahn, et al., Astroph. J. **735**, 105 (2011)
195. U. Samm, Cont. Phys. **44**, 203 (2003)
196. G.F. Matthews, et al., Phys. Scr. T **138**, 014030 (2009)
197. T. Pütterich, et al., Nucl. Fusion **50**, 025012 (2010)
198. J. Reader, Phys. Scr. T **134**, 014023 (2009)
199. C.P. Ballance, S.D. Loch, D.C. Griffin, M.S. Pindzola, J. Phys. B **43**, 205201 (2010)
200. N.R. Badnell, et al., Astron. Astroph. **406**, 1151 (2003)
201. http://www.adas.ac.uk/
202. S. Schippers, et al., Phys. Rev. A **83**, 012711 (2011)
203. C. Volpe, J. Phys. G **30**, L1 (2004)
204. C. Espinoza, R. Lazauskas, C. Volpe [arXiv:1203.0790v1] [hep-ph]
205. C. Volpe, J. Phys. G **34**, R1 (2007)
206. F. Ames, J. Cederkall, T. Sieber, F. Wenander (eds.), *The REX-ISOLDE Facility: Design and Commissioning Report*, CERN-2005-009
207. M. Lindroos, T. Nilsson (eds.), *HIE-ISOLDE: the technical options*, CERN-2006-013
208. M. Pasini, et al., *A SC upgrade for the REX-ISOLDE accelerator at CERN*, Proceedings of Linac'08, Victoria, Canada, Sep. 2008
209. P. Delahaye, et al., Nucl. Phys. A **746**, 604 (2004)
210. R. Rao, O. Kester, T. Sieber, D. Habs, K. Rudolph, Nucl. Instr. Meth. A **427**, 170 (1999)
211. J. Van der Walle, et al., *The Miniball setup at REX-ISOLDE*, Eur. Phys. J (submitted)
212. T.A. Carlson, C.W. Nestor, N. Wasserman, J.D. McDowell, Atomic Data **2**, 63 (1970)
213. Y.S. Kim, R.H. Pratt, Phys. Rev. A **27**, 2913 (1983)
214. R. Becker, O. Kester, Th. Stöhlker, J. Phys. Conf. Ser. **58**, 443 (2007)
215. G. Schiwietz, P.L. Grande, Nucl. Instr. Meth. B **175**, 125 (2001)
216. D. Voulot, et al., Nucl. Instr. Meth. B **266**, 4103 (2008)
217. A. Müller, E. Salzborn, Phys. Lett. A **6**, 391 (1977)
218. A.S. Schlachter, et al., Phys. Rev. A **27**, 3372 (1983)
219. A. Pikin, et al., J. Instr. **5**, C09003 (2010)
220. A. Lapierre, et al., J. Instr. **5**, C07001 (2010)
221. D.A. Knapp, R.E. Marrs, S.R. Elliott, E.W. Magee, R. Zasadzinski, Nucl. Instr. Meth. A **334**, 305 (1993)
222. N. Nakamura, et al., Phys. Scr. T **73**, 362 (1997)
223. J.R. Crespo López-Urrutia, A. Dorn, R. Moshammer, J. Ullrich, Phys. Scr. T **80**, 502 (1999)

224. Y. Fu, K. Yao, B. Wei, D. Lu, R. Hutton, Y. Zou, J. Instr. **5**, C08011 (2010)
225. T. Sieber, *Entwicklung von 4-Rod- und IH-Radio Frequenz Quadrupol (RFQ)-Beschleunigern für radioaktive Ionenstrahlen bei REX-ISOLDE und MAFF*, Ph.D. thesis, LMU München, 2001
226. S. Emhofer, *Aufbau und Vermessung der HF-Eigenschaften des REX-ISOLDE-IH Beschleunigers*, Diploma thesis, LMU München, 1999
227. H. Podlech, et al., Nucl. Phys. A **701**, 651c (2002)
228. T. Sieber, *Tests and First Experiments with the new REX-ISOLDE 200 MHz IH structure*, Proc. LINAC2004, Lübeck, Germany, 2004
229. M.A. Fraser, et al., Nucl. Instr. Meth. A **663**, 1 (2012)
230. F.T. Cole, F.E. Mills, Ann. Rev. Nucl. Sci. **31**, 293 (1981)
231. G. Plass, CERN/PS/DL 80-7, Genf (May 1980)
232. H. Grote, F.C. Iselin, *The MAD Program*, CERN/SL/90-13 (1990)
233. P. Schmüser, *Second general CERN accelerator School*, Cern yellow report, CERN 87-10 (1987)
234. M. Grieser, et al., Workshop on Beam Cooling and Related Topics, Montreux 1993, (Cern-94-03, Geneva, 1994), p. 257
235. S. Artikova, University Heidelberg, Ph.D. thesis (in preparation)
236. C.M. Kleffner, Diploma thesis, University Heidelberg, 1990
237. G. Bisoffi, M. Grieser, E. Jaeschke, D. Krämer, A. Noda, Nucl. Instr. Meth. A **287**, 320 (1990)
238. M. Steck, et al., Nucl. Instr. Meth. A **287**, 324 (1990)
239. S. Pastuszka, Nucl. Inst. Meth. A **369**, 11 (1996)
240. G. Barking, Diploma thesis, University Heidelberg, 1996
241. M. Beutelspacher, Diploma thesis, University Heidelberg, 1997
242. M. Beutelspacher, University Heidelberg, Ph.D. thesis, 2000
243. M. Grieser, et al., Proc. 1991 IEEE Part. Acc. Conf. (1991), p. 2817
244. B. Hochadel, University Heidelberg, Ph.D. thesis, 1994
245. O. Uwira, Hyperfine Interact. **108**, 149 (1997)
246. W. Hardt, CERN ISR-300-gs-68-11 (1968)
247. J.D. Jackson, *Classical Electrodynamis* (Wiley, New York, 1975)
248. M. Bell, I.S. Bell, Part, Accel. **12**, 49 (1982)
249. N. Bohr, K. Dan. Vidensk. Selsk. Mat. Fys. Medd. **18**, 8 (1948)
250. F. Rathmann, et al., Phys. Rev. Lett. **71**, 1379 (1993)
251. C. Montag, Univeristy Heidelberg, Diploma thesis, 1993
252. M. Blum, M. Grieser, E. Jaeschke, D. Krämer, S. Papureanu, Proc 2nd Europ. Part. Acc. Conf., Nice (1990), p. 955
253. M. Blum, Ph.D. thesis, University Heidelberg, 1989
254. M. Grieser, et al., HIAT 09 Proceedings, Venice, June 2009
255. A. Hofmann, CERN yellow report, CERN 77-13 (1977), p. 143
256. G. Wissler, Diploma thesis, University Heidelberg, 1998
257. F. Albrecht, Diploma thesis, University Heidelberg, 1993
258. B. Hochadel, et al., Nucl. Inst. Meth. A **343**, 401 (1994)
259. J. Wiza, Nucl. Instr. Meth. **162**, 587 (1979)
260. K. Unser, CERN-ISR-OP/81-14 (1981)
261. F. Laux, Ph.D. thesis, University Heidelberg, 2011
262. F. Schmitz, Bachelor thesis, University Heidelberg, 2010
263. M. Lestinsky, Ph.D. thesis, University of Heidelberg, 2007 (Online via `http://www.ub.uni-heidelberg.de/archiv/7334/`)
264. D.A. Orlov, et al., J. Appl. Phys. **106**, 054907 (2009)
265. G. Wissler, Ph.D. thesis, University of Heidelberg, 2002 (Online via `http://www.ub.uni-heidelberg.de/archiv/3101/`)
266. H. Buhr, Ph.D. thesis, University of Heidelberg, 2006 (Online via `http://www.ub.uni-heidelberg.de/archiv/6744`)
267. H. Buhr, et al., Phys. Rev. A **81**, 062702 (2010)

268. *Reaction Microscopes: The Cloud Chambers of Atomic, Molecular and Optical Physics*, http://www.mpi-hd.mpg.de/ullrich/page.php?id=126
269. Th. Stöhlker, et al., AIP Conf. Proc. **1336**, 132 (2010)
270. M. Kühnel, et al., Nucl. Instr. Meth. A **602**, 311 (2009)
271. Joao Carlos Batista Lopes, *Guideline Safety file and safety requirements for experimental apparatus and equipment*, EDMS 1108525
272. *Code F Rev. Radiation Protection - Radiation Protection Manual*, Safety code, EDMS 335729
273. *Safety Regulation SR-M Mechanical Equipment*, Safety regulation, EDMS 875606
274. *Code C1 Electrical safety code*, Safety Codes, EDMS 335725
275. *IS 23 Rev. 3 Criteria and Standard Test Methods for the Selection of Electric Cables and Wires with Respect to Fire Safety and Radiation Resistance*, Safety Instructions, EDMS 335745
276. *IS 41 Rev. The use of plastic and other non-metallic materials at CERN with respect to fire safety and radiation resistance*, Safety Instructions, EDMS 335806
277. *IS 47 The use of cryogenics fluids*, Safety Instructions, EDMS 335812